Structural elucidation of novel allosteric regulatory mechanisms in nuclear receptors

Structural Elucidation of Novel Allosteric Regulatory Mechanisms in Nuclear Receptors

PROEFSCHRIFT

ter verkrijging van de graad van doctor aan de Technische Universiteit Eindhoven,
op gezag van de rector magnificus prof.dr.ir. F.P.T. Baaijens,
voor een commissie aangewezen door het College voor Promoties,
in het openbaar te verdedigen op woensdag 16 december 2020 om 16:00 uur

door

Rens Michaël Johannes Maria de Vries

geboren te Hoorn

Dit proefschrift is goedgekeurd door de promotoren en de samenstelling van de promotiecommissie is als volgt:

voorzitter:	prof.dr.ir. M. Merkx
1e promotor:	prof.dr.ir. L. Brunsveld
co-promotor:	dr. R.G. Doveston (University of Leicester)
leden:	prof.dr. K. De Bosscher (Universiteit Gent)
	prof.dr. W.T. Zwart
	dr.rer.nat. C. Ottmann
	dr. A. Oubrie (Lead Pharma)
	dr. A.J. Markvoort

Het onderzoek of ontwerp dat in dit proefschrift wordt beschreven is uitgevoerd in overeenstemming met de TU/e Gedragscode Wetenschapsbeoefening.

"Nothing in life is to be feared, it is only to be understood. Now is the time to understand more, so that we may fear less."

– Marie Curie

"Any fool can know. The point is to understand."

– Albert Einstein

Cover: Rens de Vries

Printed by: ADC Dereumaux– The Netherlands

A catalogue record is available from the Eindhoven University of Technology Library
ISBN: 978-90-386-5172-9

This work has been financially supported the Netherlands Organization for Scientific Research (NWO) via the VICI grant 016.150.366.

Table of Contents

CHAPTER 1

Allosteric Modulation of Nuclear Receptors

Abstract

Nuclear receptors (NRs) are multi-domain proteins, whose natural regulation occurs via hormones or other small molecules binding to a classical, orthosteric, binding pocket and via intra- and inter-domain allosteric mechanisms. Allosteric modulation of NRs using synthetic small molecules has recently emerged as an interesting entry to address the need for small molecules targeting NRs in pathology, via novel modes of action and with beneficial profiles. This chapter deals with NR function and the general concept of allosteric modulation in drug discovery. Moreover, some examples will be shown of small molecules that interact with allosteric pockets and thereby effectively modulate the NR using distinct mechanisms. Overall, this chapter aims to highlight the significant benefits of allosterically modulating NRs over the classical orthosteric approach. Finally, the research subject from this thesis will be introduced, including a brief overview of the contents of the chapters.

Part of this work is published as: de Vries, R. M. J. M., Meijer, F. A., Leijten-van de Gevel, I. A. & Brunsveld, L. Allosteric small molecule modulators of nuclear receptors. Mol. Cell. Endocrinol. 485, 20–34 (2019).

Structural organization of nuclear receptors

Nuclear receptors (NRs) are a family of ligand-activated transcription factors consisting of 48 members that share high degree of structural similarity. Despite the similarity, each NR operates in different physiological processes, including cell proliferation, metabolism and development. Their key role in these processes makes them attractive drug targets. NRs have a conserved domain organization (Figure 1) starting at the N-terminus with the highly variable N-terminal domain (NTD). For most NRs, this domain contains a ligand-independent activation function (AF1). The NTD is intrinsically disordered, but the interaction with binding partners can induce folding, which can enhance transcriptional activity.[1,2] The NTD is followed by a conserved DNA binding domain (DBD) that includes two zinc fingers that recognize specific hormone response elements (HREs). The affinity for these particular HREs is determined by the NR subtype but is also dependent on NR homo- or heterodimerization.[3] The DBD is connected to the ligand-binding domain (LBD) via a hinge region that typically contains a nuclear localization signal (NLS) and undergoes posttranslational modifications (PTMs).[4] The LBD is a highly conserved domain, usually consisting of 12 helices and is commonly referred to as a "three-layer antiparallel α-helical sandwich".[5] As the full name suggests, small molecules can bind to this domain, thereby regulating the receptor's activity. This domain also plays an important role in NR dimerization. Finally, certain NRs contain a C-terminal F-domain that is highly variable across the NR family. This domain is highly variable in length, composition and function ranging from interacting with other proteins to stabilizing the ligand-bound conformations of the LBD.[6]

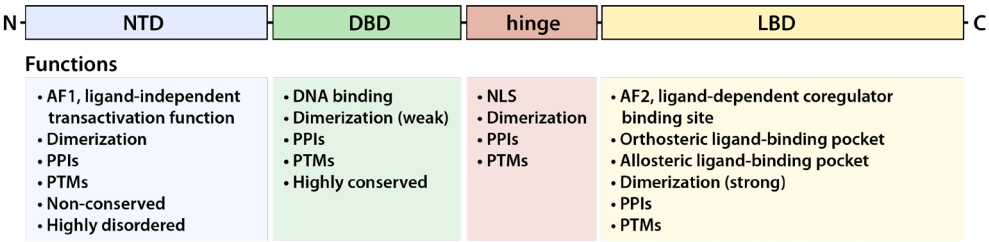

Figure 1 | Domain organization of nuclear receptors, including the regulatory function per domain. From the N-terminus (N) to C-terminus (C): N-terminal domain (NTD), DNA-binding domain (DBD), a hinge region and the ligand-binding domain (LBD). Per domain, the most important regulatory and structural characteristics are specified. Abbreviations: activation function 1/2 (AF1/AF2), protein-protein interactions (PPIs), post-translational modifications (PTMs) and nuclear localization signal (NLS). Figure adapted from De Bosscher et al. 2020.[7]

Hormones and other small molecules control the recruitment of coactivators and corepressors to the nuclear receptors. The classical "mouse-trap" model states that agonistic ligands bind in the ligand-binding pocket (LBP) of the LBD and induce a shift of helix 12 that closes the pocket, "trapping" the ligand and creating a surface suitable for coactivator binding.[8] Some years later, the alternative "dynamic stabilization" model was proposed that states that the LBD, in its apo form, can be present in a wide range of conformations.[9] Binding of an agonist stabilizes the conformations that induce cofactor binding.[10] In contrast, inverse agonists reduce the basal activity of the receptor and are primarily relevant for the modulation of constitutively active NRs.[11] Lastly, antagonists block the binding of other ligands but do not induce a conformation that leads to coactivator recruitment, thereby neutralizing gene transcription (Figure 2).[11]

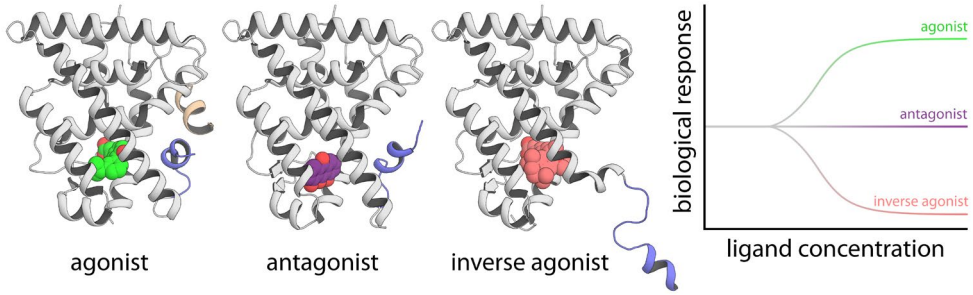

Figure 2 | Tertiary structure of a nuclear receptor LBD in complex with an agonist, antagonist and an inverse agonist as well as the associated biological response. The nuclear receptor protein is shown as a white cartoon with helix 12 colored blue. The ligands, represented as spheres, modulate the conformation of helix 12. Agonist induces coactivator binding (wheat colored cartoon), while an inverse agonist disrupts coactivator binding, lowering the biological response. An antagonist does inhibit the binding of other ligands but does not influence the basal activity of the receptor.

Intracellular mechanism of action of nuclear receptors

NRs can be categorized into four mechanistic subtypes (Figure 3). Type I receptors like the androgen receptor (AR), glucocorticoid receptor (GR) and the estrogen receptor (ER), are generally situated in the cytoplasm and are in complex with chaperone proteins. Upon binding steroid hormones like androgens, estrogens and corticoids, the chaperones dissociate, and the NR is translocated to the cell nucleus. Type I receptors primarily bind to the DNA as a homodimer by interacting with two inverted repeats.[12,13] Type II receptors like the peroxisome proliferator-activated receptors (PPAR), retinoic acid receptor (RAR)

and the orphan NRs RAR-related orphan receptor (ROR) and nuclear receptor related-1 (Nurr1), are present in the cell nucleus in complex with a corepressor protein.[14] Ligand binding leads to the dissociation of the corepressor and recruitment of coactivators and members of the transcriptional machinery. Most type II receptors can heterodimerize with the retinoid X receptor (RXR). Type III receptors behave similarly to type II but bind as homodimers to direct repeats instead of inverted. Lastly, type IV receptors bind the DNA as a monomer and interact with half-site response elements.[15]

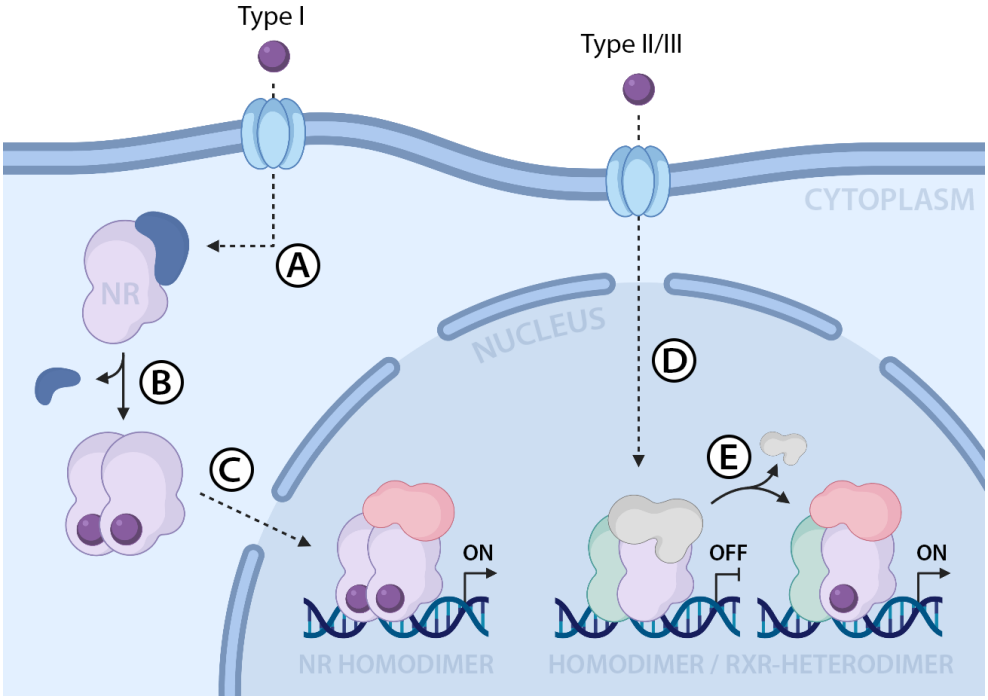

Figure 3 | Overview of the mechanism of action of nuclear receptor signaling. A. Type I nuclear receptors are bound to chaperones in the cytoplasm. **B.** Upon binding of a ligand, the chaperone protein dissociates and allows the protein to homodimerize. **C.** The homodimer complex translocates to the cell nucleus, where it interacts with DNA and recruits coactivators (red) to initiate gene transcription. **D.** Type II/III nuclear receptors are present in the cell nucleus and are in complex with corepressors (grey). **E.** Upon binding of an agonist, the corepressors dissociate, and coactivators are recruited to start gene transcription.

Inter-domain allosteric regulation of nuclear receptor activity

Until recently, structural information of NRs was only available for the separate domains. This provided valuable information on ligand and DNA binding as well as on dimerization of separate LBDs or DBDs, but left a demand for information on the implications of inter-

domain communication.[10] From 2008 onward, the multi-domain structures of various NRs were solved.[16–18] It became clear that the different domains within an NR act and communicate via modulatory, allosteric mechanisms. Allostery, in general, occurs when binding of an interaction partner, e.g. ligand or protein, at one site of a protein results in a functional change at another, topographically distinct site.[19,20] Therefore, there is an interplay between the binding site and the site of the biological response, which is established by a conformational change of the protein.[21] Figure 4 conceptually summarizes the different types of intramolecular allosteric regulatory mechanisms that have been described for NRs.

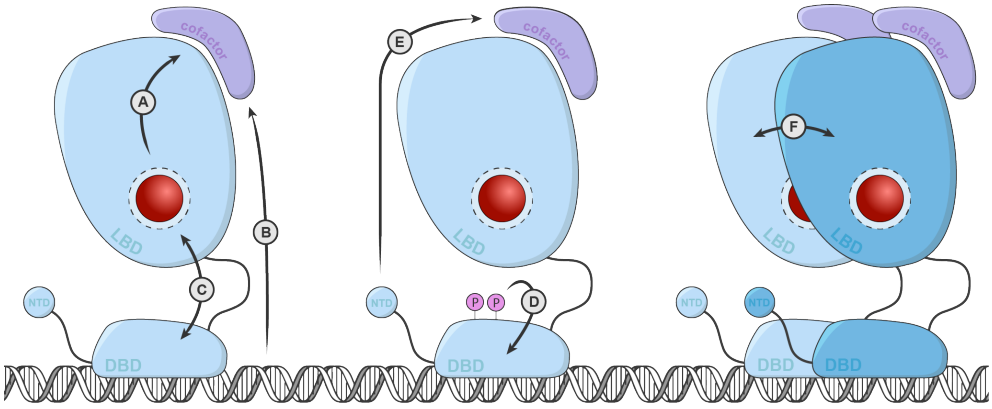

Figure 4 | Conceptual modes of intramolecular NR allosteric regulation. A. From the ligand-binding pocket to the cofactor binding site **B.** From the DNA to the cofactor binding site **C.** Between the DNA binding domain and the ligand-binding domain **D.** Via post-translational modifications within and over NR domains **E.** From the N-terminal domain to the cofactor binding site **F.** Between NR dimerization partners.

First, most endogenous and synthetic NR ligands bind to the LBP. This causes a conformational change in the LBD, resulting in cofactor recruitment at another place on the LBD (Figure 4A).[22] Clustering correlations showed that the binding mode of the ligand and peptide recruitment can be delineated and can be used to identify compounds that selectively recruit a specific cofactor.[23] Besides this primary example of NR allosteric mechanism, other more subtle allosteric mechanisms can be found in endogenous NR regulation.

The interplay between HREs and the cofactor binding site of an NR is also allosterically modulated via inter-domain communication (Figure 4B). Using a phage ELISA assay,

cofactor recruitment in response to various estrogen response elements (EREs) showed that the structure of the coactivator pocket is influenced by the type of ERE.[24] A similar behavior was observed for GR. No clear correlation was found between the affinity of GR with the binding sequence (GBS) and the transcriptional activity. The sole structural difference was found in a small loop region connecting recognition helix 1 and the dimerization loop called the "lever arm". This minor conformational difference is believed to translate through the complete protein.[25] Molecular dynamics (MD) was used to analyze the behavior of this loop region in the presence and absence of DNA. DBD dimerization or the presence of DNA significantly reduced the conformational flexibility of the lever arm, which influenced the conformational landscape of the rest of the protein.[26]

Several additional studies determined the allosteric communication between DBD and cofactor binding site using isothermal titration calorimetry (ITC) and hydrogen/deuterium exchange (HDX).[27–29] In these studies, an apparent enhancement of cofactor recruitment was observed upon binding of the receptor complex to its HRE.

The LBD and DBD can also allosterically influence each-other's ligand affinity, which was exemplified by Helsen et al. (Figure 4C).[25] Superimposition of the AR LBD and DBD crystal structures with the full-length heterodimeric RXRα-PPARγ crystal structure lead to the identification of key residues at the LBD-DBD interaction interface.[16,25] Established disease-related mutations were introduced at the interaction interface and the effect on both ligand and DNA binding was determined. Four mutations in the LBD resulted in reduced DNA binding and transactivation but did not impact ligand binding. Conversely, three DBD mutations lead to decreased ligand binding and transactivation but did not influence DNA binding.[25]

PTMs commonly occur in NRs and play an essential role in allosteric regulation. PTMs at one site of the protein can influence cofactor interactions, cellular localization, protein stability and DNA binding at a different location (Figure 4D).[30] Phosphorylation, ubiquitinylation, acetylation and SUMOylation are PTMs commonly found in NRs and are essential for their biological function. There are excellent reviews that highlight the relevance of the PTMs and their potential for drug discovery.[30–33]

The NR NTD is also involved in allosteric communication (Figure 4E). Using circular dichroism, Khan and coworkers showed that upon binding of the TATA-box-binding protein to the GR NTD, the helical content of the NTD was enhanced. This improved both coactivator recruitment and transcriptional activity.[34] Despite the significant sequence

homology differences between the NTDs, similar behavior was found for the mineralocorticoid receptor (MR) and progesterone receptor (PR).[35,36]

Homodimerization or heterodimerization with the retinoid X receptor (RXR) is a common phenomenon for NRs and already briefly discussed. These processes, similar to the binding of other protein partners, change the structural plasticity, and thereby the behavior of an NR.[37] This, in turn, can allosterically affect the recruitment and binding of ligands (Figure 4F). As an example, RARβ is known to be a monomer in solution, but upon binding of cofactors, it forms a homodimeric assembly.[38] A similar behavior was found for VDR and TR when bound to coactivators.[39,40] To dimerize, the receptor must undergo a conformational change, which can lead to asymmetry in the dimer complex. For both RARβ and ERα, it was observed that in the homodimer complex, this asymmetry was altering the ligand's binding mode, as revealed via two different poses of the same ligand in each of the monomers.[41,42] Furthermore, it has been reported that also in the absence of a ligand, the NR homodimer can be asymmetric. The crystal structure of the apo-PPARγ LBD contains two monomers in the asymmetric unit forming a homodimer, with only one of the monomers present in its active conformation.[43]

The preceding examples highlight the importance of allosteric modulation within the NR to finetune its biological function. Therefore, the design of small molecules that bind to allosteric pockets, thereby modulating the NR's activity, is a promising additional approach for NR drug discovery.

Allosteric modulation of nuclear receptors using small molecules

Modulation of NRs via the orthosteric LBP has been a very successful approach and led to the development of several FDA approved drugs and many ongoing clinical trials.[44] However, effectively modulating the NR even via the orthosteric LBP can be challenging.[45] As previously mentioned, the orthosteric LBP is highly homologous across the NRs. Small molecules designed to bind a specific NR also regularly show affinity for other NRs, resulting in side-effects. Moreover, drug resistance mutations are commonly observed when drug treatment is used for a more extended period, which could lead to agonist/antagonist switching.[45–47] Small molecules that bind and modulate NRs at regulatory sites distinct from the orthosteric LBP could potentially overcome these drawbacks. Because binding of these types of modulators is not limited to a single evolutionary conserved pocket, there is no competition with the endogenous ligand and a high degree of receptor selectivity can be obtained.[20,46] Therefore, these allosteric

modulators can also be a compelling alternative when drug-associated mutations occur in the orthosteric LBP. Unfortunately, the number of small molecules that modulate NRs via allosteric pockets is very limited, especially compared to the extensive library of compounds binding to orthosteric LBP.[48] The design and optimization of allosteric ligands have proven to be challenging, and a flat structure-activity relationship is often observed.[49] The next part of this chapter will briefly summarize some of the allosteric ligands that have been identified for NRs and what type of mechanism they use to modulate the receptor (Figure 5).

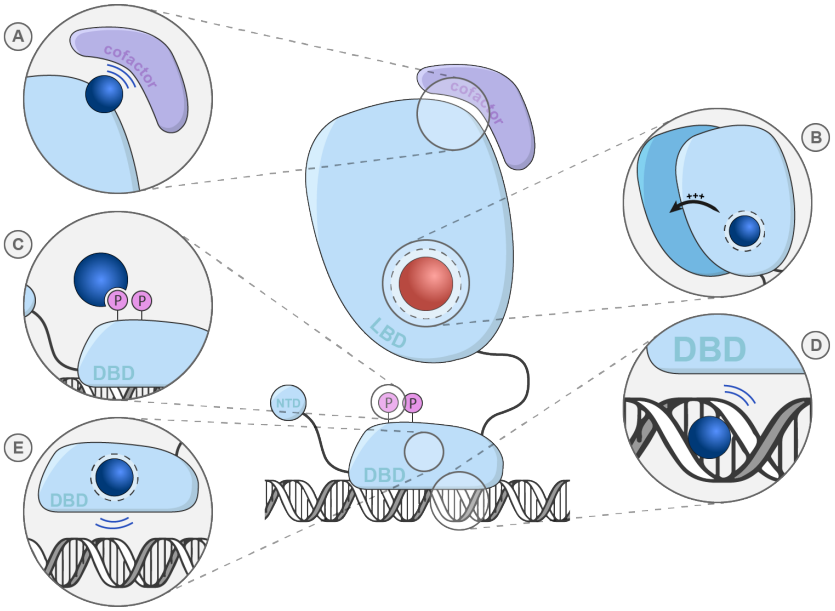

Figure 5 | Different modes of actions for small molecule-based allosteric NR modulation outside of the ligand-binding domain. A. Via binding to the cofactor binding site. **B.** Via compounds modulating the NR dimerization. **C.** Via the recognition of post-translational modifications. **D.** Via modulation of the DNA response element. **E.** Via binding to the DNA binding domain.

Several molecules were designed to block the AF-2 site, thereby inhibiting cofactor recruitment (Figure 5A).[50] One method is to create constrained peptides or peptide mimetics that mimic the LXXLL motif of the coactivator.[45,48,51] The synthetic peptides were designed to have high affinity for the protein. Therefore, if an agonist activates the NR, it favors the binding of the synthetic peptide over the endogenous cofactor, effectively blocking transcriptional activity. Additionally, synthetic ligands have been reported that selectively bind in or close to the AF-2 site, abolishing the interaction surface of the

coactivator. The interaction of these allosteric modulators is often independent of the presence of the orthosteric endogenous ligands.[52,53] There are examples of allosteric ligands that have nanomolar affinity for the target NR and, upon binding, effectively inhibit cofactor binding.[52–54]

NR homo- and heterodimerization also provide entries for allosteric modulation via small molecules (Figure 5B). Through its ability to form heterodimeric assemblies, RXR can modulate and activate multiple NR partners such as PPAR, LXR and Nurr1. In general, RXR dimerization partners can be arranged into two classes, being permissive and non-permissive heterodimer partners. For permissive heterodimers, the sole presence of the RXR ligand is enough to make the heterodimer transcriptionally active. If the partner's ligand is also present, this results in a stronger activation. In contrast, for non-permissive heterodimers, the partner's ligand is required for activation, since they are not responsive to RXR-ligands (rexinoids) on their own. However, like permissive heterodimers, the presence of an RXR ligand does enhance the biological response.[55,56] In 2015, the structural mechanism by which RXR transduces its signal to its dimer partner has been further elucidated.[57] As an example of the fine interplay of RXR heterodimer regulation, in a Parkinson's disease mouse model, treatment with the rexinoid bexarotene enhanced the clearance of β-amyloids, improving the neural function. This is believed to be caused by the activation of the permissive RXR-PPAR and RXR-LXR heterodimers.[58] Furthermore, it has been shown that the type of RXR ligand can have a substantial effect on the dimerization behavior of RXR and, therefore, on the transactivation capacity of its dimer partner.[59–61] The RXR ligand LG101506 was shown to selectively activate RXR-PPAR heterodimers over other heterodimers, e.g. RXR-RAR, RXR-LXR and RXR-FXR. Selective activation of RXR-PPAR is beneficial in the treatment of type 2 diabetes by improving insulin sensitivity while simultaneously keeping the triglyceride levels constant.[62,63] Lastly, in a 2017 study, the effect of minor modifications on RXR ligand scaffolds on the heterodimerization behavior of RXR with the orphan NR Nurr1 was analyzed. Interestingly, ligands that introduced steric bulk towards either helix 7 or 11 of RXR significantly inhibited the heterodimer formation.[61]

Several ligands have been identified that allosterically modulate NRs by interacting with specific PTMs (Figure 5C). Phosphorylation of Ser273 in PPARγ upregulates target genes, thereby decreasing the insulin sensitivity.[64] Ser273 phosphorylation could be inhibited using PPARγ ligands that bind to the orthosteric LBP and display a minimal agonistic activity. Due to the low agonistic affinity, side-effects caused by PPARγ

activation were minimal.[65] For the farnesoid X receptor (FXR), SUMOylation of Lys277 is essential for the repression of pro-inflammatory genes. SUMOylation of this residue can be inhibited by acetylation of Lys217, a PTM that commonly occurs in obese patients. For this reason, targeting this acetylation site has been of significant interest in improving hepatic inflammation and glucose intolerance.[66] The F-domain of ERα encompasses a phosphorylation site that can interact with a regulatory protein family called 14-3-3. The protein-protein complex can be stabilized with fusicoccin, a small-molecule isolated from a fungus.[67] This causes a significant reduction of ERα homodimerization and, as a result, inhibition of the downstream gene regulation. ERα is overexpressed in 70% of breast cancer patients making inhibition of ERα dimerization a promising approach to treat breast cancer.

Lastly, the interaction between the DBD of the NR and the DNA is essential to initiate the expression of target genes. Allosteric ligands can effectively modulate this interaction by binding to either the DBD or the DNA.[45,48] Hairpin polyamides interact non-covalently to the minor groove of the DNA and effectively inhibit the interaction with AR and ERα (Figure 5D).[45,68,69] Another approach is to target the zinc fingers of the DBD using small molecules (Figure 5E). The zinc fingers are essential for the overall fold of the DBD, and a disturbed conformation can lead to inhibition of DNA binding.[45,70] This can be accomplished by compounds that oxidize the zinc finger thiolates to disulfides, which releases Zn^{2+}. Because of the high sequence similarity of the DBD within the NR family, it is challenging to design molecules that selectively target a specific NR DBD.[45]

Aim and Scope

This chapter has outlined how small molecule allosteric modulation can be a promising approach for NR modulation. In this thesis, the focus will be on two types of allosteric modulation. First, the effect of small molecule binding on receptor homo- and heterodimerization will be evaluated, with particular emphasis on the ability of small molecules to direct the formation of specific heterodimers. Second, the other type of allosteric modulation deals with a class of molecules that bind to an allosteric site on the LBD, blocking cofactor recruitment. In particular, we focus on those modulators that binds the NR independently of an orthosteric modulator. Despite the binding being independent, still, binding of an orthosteric ligand can influence the binding behavior of the allosteric ligand and vice versa, a concept known as cooperative binding. The exact

molecular mechanisms behind cooperative dual ligand binding and ligand-mediated receptor dimerization are poorly understood. Therefore, for both types of NR allostery, the primary aim is to decipher the structural mechanism by which these ligands exert their effect. A comprehensive understanding of these mechanisms could aid in the design of more selective and effective allosteric drugs.

In **Chapter 2**, we will explore how small molecules influence RXRα homo- and heterodimerization. One of the RXRα heterodimer partners analyzed in this chapter is the orphan NR Nurr1, an NR difficult to modulate via the orthosteric LBP. First, a structural model of the RXRα-Nurr1 complex is created to identify regions of the receptor that are affected by rexinoid binding and that could impact the ability to dimerize with other receptors. Next, a modular and highly sensitive *in vitro* luciferase complementation assay is designed based on the NanoBiT technology. This assay revealed that the dimerization behavior of the RXRα homodimer, as well as the RXRα-Nurr1 and RXRα-PPAR heterodimer, can be significantly changed in the presence of specific rexinoids. Interestingly, the ligands were shown to regulate each dimer in a distinct manner. In other words, some rexinoids stabilize a specific dimer while abolishing others. The results indicate that the dimerization behavior of nuclear receptors can be controlled with small molecules.

Chapter 3 describes elements for the identification of a unique non-RXR heterodimer. Together with Ghent University, the direct interaction between the orphan nuclear receptor ERRα and PPARα is determined. In a cellular context, the interaction between both NRs was established recently. A NanoBiT assay combined with other biochemical techniques was used to show that the LBDs of both proteins are not able to dimerize *in vitro*. Instead, the full-length ERRα was required to dimerize with the PPARα LBD. An *in vitro* His-tag pulldown assay was developed to confirm that both proteins interact in a direct manner.

Chapter 4 presents the structural identification of two modulators (FM26 and compound 13) of RORγt that prevent cofactor recruitment by binding to an allosteric pocket in the LBD. First, biochemical assays show that FM26 and compound 13 both interact with an allosteric pocket on the RORγt LBD with submicromolar affinity. The protein construct and purification method were optimized to enable the crystallization of RORγt in complex with these novel allosteric modulators. The crystal structures reveal subtle differences in the ligand's binding mode compared to the previously published co-crystal structure of the allosteric ligand MRL-871 in complex with RORγt.

Chapter 5 shows that the allosteric ligands described in Chapter 4 can interact with RORγt in the presence of orthosteric agonists. Binding of both ligands was demonstrated to be cooperative, as the binding of a ligand at one site of RORγt enhanced the binding affinity of the ligand at the other site. To determine the mechanism behind this cooperative behavior, we solved the first ternary complexes of RORγt in complex with both an orthosteric and allosteric ligand. In total, twelve novel crystal structures were solved, including all combinations of four orthosteric and three allosteric ligands. The structural data revealed a clamping mechanism that alters the conformation of the allosteric ligand that occurs upon binding of the orthosteric modulator. With molecular dynamics, the subtle mechanism behind this clamping motion was further elucidated, presenting the critical role of helix 4-5 to establish cooperative binding. The structural characteristics of helix 4-5 are greatly conserved across the NR family, suggesting that this mechanism might be an important feature, possibly overlooked in other NRs.

Chapter 6, the epilogue, puts the work described in this thesis into perspective and provides some future directions and potential experimental strategies to further advance this field of research. Additional factors that could play a role in the allosteric regulation of NR dimerization are discussed and we deliberate how some of the identified molecular mechanisms can influence other NR-associated functions.

References

1. Kumar, R. & Litwack, G. Structural and functional relationships of the steroid hormone receptors' N-terminal transactivation domain. *Steroids* **74**, 877–883 (2009).
2. Helsen, C. & Claessens, F. Looking at nuclear receptors from a new angle. *Mol. Cell. Endocrinol.* **382**, 97–106 (2014).
3. Helsen, C. *et al.* Structural basis for nuclear hormone receptor DNA binding. *Mol. Cell. Endocrinol.* **348**, 411–417 (2012).
4. Haelens, A., Tanner, T., Denayer, S., Callewaert, L. & Claessens, F. The hinge region regulates DNA binding, nuclear translocation, and transactivation of the androgen receptor. *Cancer Res.* **67**, 4514–23 (2007).
5. Bourguet, W., Ruff, M., Chambon, P., Gronemeyer, H. & Moras, D. Crystal structure of the ligand-binding domain of the human nuclear receptor RXR-α. *Nature* **375**, 377–382 (1995).
6. Patel, S. R. & Skafar, D. F. Modulation of nuclear receptor activity by the F domain. *Mol. Cell. Endocrinol.* **418**, 298–305 (2015).
7. De Bosscher, K., Desmet, S. J., Clarisse, D., Estébanez-Perpiña, E. & Brunsveld, L. Nuclear receptor crosstalk — defining the mechanisms for therapeutic innovation. *Nature Reviews Endocrinology* vol. 16 363–377 (2020).
8. Renaud, J.-P. *et al.* Crystal structure of the RAR-γ ligand-binding domain bound to all-trans retinoic acid. *Nature* **378**, 681–689 (1995).

9. Pissios, P., Tzameli, I., Kushner, P. J. & Moore, D. D. Dynamic Stabilization of Nuclear Receptor Ligand Binding Domains by Hormone or Corepressor Binding. *Mol. Cell* **6**, 245–253 (2000).
10. Rastinejad, F., Huang, P., Chandra, V. & Khorasanizadeh, S. Understanding nuclear receptor form and function using structural biology. *J. Mol. Endocrinol.* **51**, T1–T21 (2013).
11. Kojetin, D. J. & Burris, T. P. Small molecule modulation of nuclear receptor conformational dynamics: implications for function and drug discovery. *Mol. Pharmacol.* **83**, 1–8 (2013).
12. Pratt, W. B., Galigniana, M. D., Morishima, Y. & Murphy, P. J. M. Role of molecular chaperones in steroid receptor action. *Essays in Biochemistry* vol. 40 41–58 (2004).
13. Bulynko, Y. A. & O'Malley, B. W. Nuclear receptor coactivators: Structural and functional biochemistry. *Biochemistry* **50**, 313–328 (2011).
14. Tata, J. R. Signalling through nuclear receptors. *Nature Reviews Molecular Cell Biology* vol. 3 702–710 (2002).
15. Mangelsdorf, D. J. *et al.* The nuclear receptor superfamily: The second decade. *Cell* **83**, 835–839 (1995).
16. Chandra, V. *et al.* Structure of the intact PPAR-γ–RXR-α nuclear receptor complex on DNA. *Nature* **456**, 350–356 (2008).
17. Rochel, N. *et al.* Common architecture of nuclear receptor heterodimers on DNA direct repeat elements with different spacings. *Nat. Struct. Mol. Biol.* **18**, 564–570 (2011).
18. Orlov, I., Rochel, N., Moras, D. & Klaholz, B. P. Structure of the full human RXR/VDR nuclear receptor heterodimer complex with its DR3 target DNA. *EMBO J.* **31**, 291–300 (2012).
19. Motlagh, H. N., Wrabl, J. O., Li, J. & Hilser, V. J. The ensemble nature of allostery. *Nature* **508**, 331–339 (2014).
20. Nussinov, R. & Tsai, C.-J. Allostery in Disease and in Drug Discovery. *Cell* **153**, 293–305 (2013).
21. Changeux, J. P. & Christopoulos, A. Allosteric Modulation as a Unifying Mechanism for Receptor Function and Regulation. *Cell* vol. 166 1084–1102 (2016).
22. Hilser, V. J. & Thompson, E. B. Structural dynamics, intrinsic disorder, and allostery in nuclear receptors as transcription factors. *J. Biol. Chem.* **286**, 39675–82 (2011).
23. Folkertsma, S. *et al.* The Use of *in Vitro* Peptide Binding Profiles and *in Silico* Ligand-Receptor Interaction Profiles to Describe Ligand-Induced Conformations of the Retinoid X Receptor α Ligand-Binding Domain. *Mol. Endocrinol.* **21**, 30–48 (2007).
24. Hall, J. M., McDonnell, D. P. & Korach, K. S. Allosteric Regulation of Estrogen Receptor Structure, Function, and Coactivator Recruitment by Different Estrogen Response Elements. *Mol. Endocrinol.* **16**, 469–486 (2002).
25. Helsen, C. *et al.* Evidence for DNA-binding domain--ligand-binding domain communications in the androgen receptor. *Mol. Cell. Biol.* **32**, 3033–43 (2012).
26. Frank, F., Okafor, C. D. & Ortlund, E. A. The first crystal structure of a DNA-free nuclear receptor DNA binding domain sheds light on DNA-driven allostery in the glucocorticoid receptor. *Sci. Rep.* **8**, 13497 (2018).
27. Putcha, B. D. K. & Fernandez, E. J. Direct interdomain interactions can mediate allosterism in the thyroid receptor. *J. Biol. Chem.* **284**, 22517–22524 (2009).
28. Zhang, J. *et al.* DNA binding alters coactivator interaction surfaces of the intact VDR-RXR complex. *Nat. Struct. Mol. Biol.* **18**, 556–563 (2011).
29. de Vera, I. M. S. *et al.* Synergistic Regulation of Coregulator/Nuclear Receptor Interaction by Ligand and DNA. *Structure* **25**, 1506-1518.e4 (2017).
30. Becares Salles, N., Gage, M. C. & Pineda-Torra, I. Post-translational modifications of lipid-activated nuclear receptors: Focus on metabolism. *Endocrinology* **158**, en.2016-1577 (2016).
31. Faus, H. & Haendler, B. Post-translational modifications of steroid receptors. *Biomed. Pharmacother.* **60**, 520–528 (2006).

32. Anbalagan, M., Huderson, B., Murphy, L. & Rowan, B. G. Post-translational modifications of nuclear receptors and human disease. *Nucl. Recept. Signal.* **10**, e001 (2012).
33. Brunmeir, R., Xu, F., Brunmeir, R. & Xu, F. Functional Regulation of PPARs through Post-Translational Modifications. *Int. J. Mol. Sci.* **19**, 1738 (2018).
34. Khan, S. H., Ling, J. & Kumar, R. TBP Binding-Induced Folding of the Glucocorticoid Receptor AF1 Domain Facilitates Its Interaction with Steroid Receptor Coactivator-1. *PLoS One* **6**, e21939 (2011).
35. Fischer, K., Kelly, S. M., Watt, K., Price, N. C. & McEwan, I. J. Conformation of the Mineralocorticoid Receptor N-terminal Domain: Evidence for Induced and Stable Structure. *Mol. Endocrinol.* **24**, 1935–1948 (2010).
36. Kumar, R. *et al.* Regulation of the structurally dynamic N-terminal domain of progesterone receptor by protein-induced folding. *J. Biol. Chem.* **288**, 30285–99 (2013).
37. Jin, L. & Li, Y. Structural and functional insights into nuclear receptor signaling. *Adv. Drug Deliv. Rev.* **62**, 1218–26 (2010).
38. Venepally, P., Reddy, L. G. & Sani, B. P. Analysis of Homo- and Heterodimerization of Retinoid Receptors in Solution. *Arch. Biochem. Biophys.* **343**, 234–242 (1997).
39. Takeshita, A., Ozawa, Y. & Chin, W. W. Nuclear Receptor Coactivators Facilitate Vitamin D Receptor Homodimer Action on Direct Repeat Hormone Response Elements. *Endocrinology* **141**, 1281–1281 (2000).
40. Velasco, L. F. R. *et al.* Thyroid hormone response element organization dictates the composition of active receptor. *J. Biol. Chem.* **282**, 12458–12466 (2007).
41. Delfosse, V. *et al.* Structural and mechanistic insights into bisphenols action provide guidelines for risk assessment and discovery of bisphenol A substitutes. *Proc. Natl. Acad. Sci. U. S. A.* **109**, 14930–5 (2012).
42. Billas, I. & Moras, D. Allosteric Controls of Nuclear Receptor Function in the Regulation of Transcription. *J. Mol. Biol.* **425**, 2317–2329 (2013).
43. Nolte, R. T. *et al.* Ligand binding and co-activator assembly of the peroxisome proliferator-activated receptor-gamma. *Nature* **395**, 137–43 (1998).
44. Zhao, L., Zhou, S. & Gustafsson, J.-Å. Nuclear receptors: recent drug discovery for cancer therapies. *Endocr. Rev.* **40**, 1207–1249 (2019).
45. Caboni, L. & Lloyd, D. G. Beyond the ligand-binding pocket: targeting alternate sites in nuclear receptors. *Med. Res. Rev.* **33**, 1081–1118 (2013).
46. Lu, S., Li, S. & Zhang, J. Harnessing allostery: a novel approach to drug discovery. *Med. Res. Rev.* **34**, 1242–1285 (2014).
47. Liu, H., Han, R., Li, J., Liu, H. & Zheng, L. Molecular mechanism of R-bicalutamide switching from androgen receptor antagonist to agonist induced by amino acid mutations using molecular dynamics simulations and free energy calculation. *J. Comput. Aided. Mol. Des.* **30**, 1189–1200 (2016).
48. Moore, T. W., Mayne, C. G. & Katzenellenbogen, J. A. Minireview: Not picking pockets: Nuclear receptor alternate-site modulators (NRAMs). *Molecular Endocrinology* vol. 24 683–695 (2010).
49. Conn, P. J., Kuduk, S. D. & Doller, D. Drug Design Strategies for GPCR Allosteric Modulators. *Annu. Rep. Med. Chem.* **47**, 441–457 (2012).
50. Wang, Y. *et al.* A second binding site for hydroxytamoxifen within the coactivator-binding groove of estrogen receptor beta. *Proc. Natl. Acad. Sci.* **103**, 9908–9911 (2006).
51. Tice, C. M. & Zheng, Y. J. Non-canonical modulators of nuclear receptors. *Bioorganic Med. Chem. Lett.* **26**, 4157–4164 (2016).
52. Scheepstra, M. *et al.* Identification of an allosteric binding site for RORγt inhibition. *Nat. Commun.* **6**, 1–10 (2015).
53. Meijer, F. A. *et al.* Ligand-Based Design of Allosteric Retinoic Acid Receptor-Related Orphan Receptor γt (RORγt) Inverse Agonists. *J. Med. Chem.* **63**, 241–259 (2020).

54. de Vries, R. M. J. M., Meijer, F. A., Doveston, R. G. & Brunsveld, L. Elucidation of an allosteric mode-of-action for a thienopyrazole RORγt inverse agonist. *ChemMedChem* **n/a**, (2020).
55. Forman, B. M., Umesono, K., Chen, J. & Evans, R. M. Unique response pathways are established by allosteric interactions among nuclear hormone receptors. *Cell* **81**, 541–550 (1995).
56. Kurokawa, R. *et al.* Regulation of retinoid signalling by receptor polarity and allosteric control of ligand binding. *Nature* **371**, 528–531 (1994).
57. Kojetin, D. J. *et al.* Structural mechanism for signal transduction in RXR nuclear receptor heterodimers. *Nat. Commun.* **6**, 8013 (2015).
58. Cramer, P. E. *et al.* ApoE-Directed Therapeutics Rapidly Clear -Amyloid and Reverse Deficits in AD Mouse Models. *Science (80-.).* **335**, 1503–1506 (2012).
59. McFarland, K. *et al.* Low Dose Bexarotene Treatment Rescues Dopamine Neurons and Restores Behavioral Function in Models of Parkinson's Disease. *ACS Chem. Neurosci.* **4**, 1430–1438 (2013).
60. Giner, X. C., Cotnoir-White, D., Mader, S. & Lévesque, D. Selective ligand activity at Nur/retinoid X receptor complexes revealed by dimer-specific bioluminescence resonance energy transfer-based sensors. *FASEB J.* **29**, 4256–4267 (2015).
61. Scheepstra, M. *et al.* Ligand Dependent Switch from RXR Homo- to RXR-NURR1 Heterodimerization. *ACS Chem. Neurosci.* **8**, (2017).
62. Leibowitz, M. D. *et al.* Biological Characterization of a Heterodimer-Selective Retinoid X Receptor Modulator: Potential Benefits for the Treatment of Type 2 Diabetes. *Endocrinology* **147**, 1044–1053 (2006).
63. Michellys, P. Y. *et al.* Design, synthesis, and structure - Activity relationship studies of novel 6,7-locked-[7-(2-alkoxy-3,5-dialkylbenzene)-3-methylocta]-2,4,6-trienoic acids. *J. Med. Chem.* **46**, 4087–4103 (2003).
64. Choi, J. H. *et al.* Anti-diabetic drugs inhibit obesity-linked phosphorylation of PPARγ by Cdk5. *Nature* **466**, 451–456 (2010).
65. Choi, J. H. *et al.* Antidiabetic actions of a non-agonist PPARγ ligand blocking Cdk5-mediated phosphorylation. *Nature* **477**, 477–481 (2011).
66. Kim, D.-H. *et al.* A dysregulated acetyl/SUMO switch of FXR promotes hepatic inflammation in obesity. *EMBO J.* **34**, 184–199 (2015).
67. De Vries-van Leeuwen, I. J. *et al.* Interaction of 14-3-3 proteins with the Estrogen Receptor Alpha F domain provides a drug target interface. *Proc. Natl. Acad. Sci.* **110**, 8894–8899 (2013).
68. Gearhart, M. D. *et al.* Inhibition of DNA Binding by Human Estrogen-Related Receptor 2 and Estrogen Receptor α with Minor Groove Binding Polyamides. *Biochemistry* **44**, 4196–4203 (2005).
69. Nickols, N. G. & Dervan, P. B. Suppression of androgen receptor-mediated gene expression by a sequence-specific DNA-binding polyamide. *Proc. Natl. Acad. Sci. U. S. A.* **104**, 10418–10423 (2007).
70. Whittal, R. M. *et al.* Preferential Oxidation of Zinc Finger 2 in Estrogen Receptor DNA-binding Domain Prevents Dimerization and, Hence, DNA Binding. *Biochemistry* **39**, 8406–8417 (2000).

CHAPTER 2

Modulation of RXR Dimerization with Small Molecules

Abstract

The retinoid X receptor (RXR) is a nuclear receptor (NR), which is classified as a master regulator of gene transcription through its capacity to form heterodimers with other NRs, thereby controlling many physiological processes. Modulation of specific RXR heterodimers has shown to be beneficial in neurodegenerative diseases, but also diabetes and cancer. It has been demonstrated that rexinoids can selectively influence the dimerization and transcriptional activity of specific RXR heterodimers. Recently, also the RXR-Nurr1 complex has been shown to be amenable to small molecule heterodimerization regulation. However, the underlying structural mechanism behind this ligand-induced heterodimer selectivity is poorly understood. In this chapter, we will explore what structural characteristics of the RXR-ligand determine the dimerization behavior of RXRα. A novel NanoBiT assay is developed to analyze the effect of rexinoid binding on RXRα-RXRα, RXRα-Nurr1 and RXRα-PPARα dimerization. Combining the biochemical data with structural information reveals that the conformational flexibility of two helices on the RXRα dimerization interface plays a crucial role in RXR dimerization and can be effectively modulated by rexinoids.

Part of this work is published as: Scheepstra, M., Andrei, S. A., de Vries, R. M. J. M., et al. Ligand Dependent Switch from RXR Homo- to RXR-NURR1 Heterodimerization. ACS Chem. Neurosci. 8, 2065–2077 (2017).

Introduction

The retinoid X receptor (RXR) is a nuclear receptor (NR) that plays a critical role in the regulation of transcription through heterodimerization with other NRs, including PPAR, LXR, FXR and the orphan nuclear receptor Nurr1.[1,2] The ability to modulate multiple signaling pathways makes RXR an attractive drug target for the treatment of a wide variety of diseases. Activation of these heterodimeric complexes has indeed demonstrated to be beneficial for neurodegenerative diseases, diabetes and cancer.[3–5]

The unique ability of RXR to heterodimerize is believed to be caused by the insertion of a single residue in the I-box of RXR. On helix 7, a glutamine is inserted in the alpha helix, forming a π-helix (Figure 1A). This type of helix is rare, energetically unfavorable, and is only present if it has a functional benefit for the protein. Therefore, these π-helices are primarily found in active sites of the protein. In RXR, Glu352 forms a salt bridge with Arg348, thereby bringing it near Lys431 on helix 10. In the crystal structure of full-length RXRα-PPARα, this lysine residue interacts with the carboxy-terminus of PPARα (Figure 1A). This salt bridge stabilizes a conformation of helix 12 of PPARα that allows for coactivator binding.[6] In 2015, Kojetin and coworkers further elucidated the intramolecular mechanism by which signal transduction occurs upon heterodimerization and what allosteric effects dimerization have on helix 12 and the conformation of both the AF-2 site and the ligand-binding pocket.[7] In short, this study revealed that ligand-binding leads to a conformational change of helix 11, located on the dimerization interface. This shift leads to a rotation of helices at the dimer interface and the central core of the dimer partner. This structural rearrangement demonstrated to change the conformation of helix 12 and the ligand-binding pocket (LBP) of the partner NR.

Recently, it has been demonstrated that rexinoids significantly influence the formation of specific RXR heterodimers.[4,5,8–12] The group of Pierre Germain showed that RXR and RAR ligands could be used to finetune the RXR-RAR heterodimer activity by directing the specificity and activity of the complex.[10] Cesario and coworkers showed that rexinoid LG100754 activates RXR-PPAR heterodimers to improve insulin resistance but was unable to activate RXR-RXR, RXR-LXR, RXR-FXR and RXR-NGFI-B.[5] BRF110, an RXRα agonist derived from XCT0135908 but with better drug-like properties, showed to activate RXRα-Nurr1 heterodimers selectively but did not activate RXRα-RXRα, RXRα-RXRγ, RXRα-PPARγ and RXRα-VDR. Only the RXRα-Nur77 heterodimer, like Nurr1 a member of the NR4A1 subfamily, showed partial activation upon binding of BRF110. In Parkinson's disease (PD) mouse models, BRF110 was shown to be neuroprotective by activating Nurr1-associated

genes.[11] Moreover, McFarland and coworkers showed that the dimerization behavior of the RXR homodimer and RXR-Nurr1 heterodimer could be effectively regulated with commercially available rexinoids using a BRET-2 assay format.[4] The rexinoids 9-cis-retinoic acid (9-cis-RA) and bexarotene effectively stabilized the RXR-Nurr1 heterodimer, while HX630 and XCT0135908 showed a strong bias towards the RXR homodimer. Scheepstra *et al.* continued this research by performing the same BRET-2 assay with a more focused and less chemically diverse set of ligands built around a biaryl scaffold.[8] Most ligands behaved as full agonists in biochemical assays but showed a significantly differentiating effect on the RXR dimerization properties. Within this small library, the compact compound 4 showed a 25-fold bias towards the RXR-Nurr1 heterodimer, where the bulkier derivative 9 showed a 10-fold selectivity towards the RXR homodimer (Figure S1). Crystal structures of RXR in complex with these cinnamic acid derivatives revealed no conclusive explanation for the altered dimerization behaviors.[8]

At present, rexinoids are often selected based on their affinity and their effect on the receptor's activity. The preceding examples exemplify the importance of rexinoid selection to obtain a reliable readout for cellular or animal studies. Two chemically diverse full agonists could lead to a completely different biological response caused by the dimerization profile as well as cofactor recruitment. However, the molecular mechanism of how ligands induce RXR dimer selectivity remains unclear but is essential to prevent side-effects caused by the activation of other heterodimers.

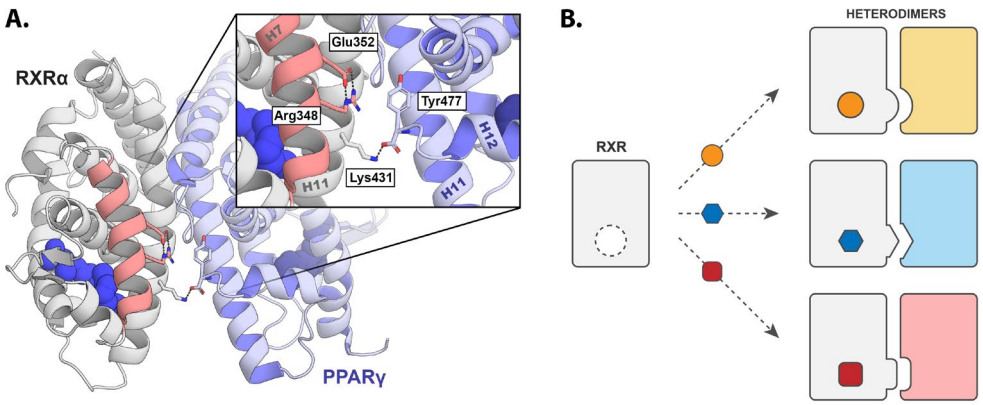

Figure 1 | Heterodimerization mechanism of RXR A. The LBDs of RXRα (white) and PPARγ (blue) from the full-length RXRα-PPARγ heterodimer (PDB: 3DZY). Helix 7 of RXRα is highlighted in red, presenting the Glu352 insertion forming a π-helix. The inset shows the stabilization of helix 12 from PPARγ by Lys431 of RXRα. **B.** The concept of selective small-molecule-induced heterodimerization of RXR. Small molecules change the structural plasticity of RXR, which "shapes" RXR to interact with specific heterodimer partners.

This chapter will address the molecular mechanism by which rexinoids can influence RXR dimerization and how selectivity can be obtained. We believe that the shape of the rexinoid plays an important allosteric role in the molding and the conformational dynamics of the dimerization interface of RXR. Therefore, differently shaped ligands can lead to the same activation state of the receptor but recruit different dimerization partners (Figure 1B). The RXR-Nurr1 heterodimer will be used to explore the effect of rexinoids on dimerization. Nurr1 is an orphan NR that binds to DNA as a monomer and controls the development and maintenance of dopamine neurons, and an impaired function is, therefore, associated with PD.[4,11,13–15] The crystal structure of the Nurr1 LBD revealed that the orthosteric LBP is completely occupied with bulky hydrophobic sidechains, making it challenging to modulate this receptor via the classical, orthosteric approach.[16,17] Since Nurr1 is a permissive heterodimer partner of RXR[18]; this makes modulation of Nurr1 via RXR a viable and relevant approach to modulate Nurr1-associated genes.

Results and discussion

RXR-Nurr1 heterodimer model

To date, the crystal structure of the RXR-Nurr1 complex is not available. However, the crystal structures of RXR with both permissive and non-permissive NR partners generally show a comparable dimerization interface for the receptors, primarily composed of helices 9 and 10 of both receptors.[7,19–23] Therefore, a model was constructed based on the full-length crystal structure of RXRα-PPARγ in complex with 9-cis-RA and rosiglitazone (PDB 3DZY).[19] PPARγ is a permissive heterodimer partner of RXR and it is, therefore, expected that the binding mode of Nurr1 would be comparable.[7,19–23] The LBDs of RXRα in complex with ligand 4 (PDB: 5MKU) and Nurr1 (PDB: 1OVL) were aligned to the LBDs of RXRα and PPARγ, respectively (Figure 2B).[8,16] For this model, single residue mutations for both RXRα (A416K/D and R421P) and Nurr1 (P560A and L560A) that are known to abolish RXR-Nurr1 heterodimerization are indeed located at the dimerization interface (Figure 2C).[24]

Like the RXRα-PPARγ crystal structure, the RXRα-Nurr1 model shows that in addition to helix 9 and 10 also helix 12 of Nurr1 is present at the dimer interface in close contact with helix 7 and 11 of RXRα (Figure 2C-D). Compared to other RXR heterodimer partners, helix 12 of Nurr1 is composed of more residues that form a relatively long alpha-helical section, restricting the conformational freedom of this helix. Therefore, for RXRα to

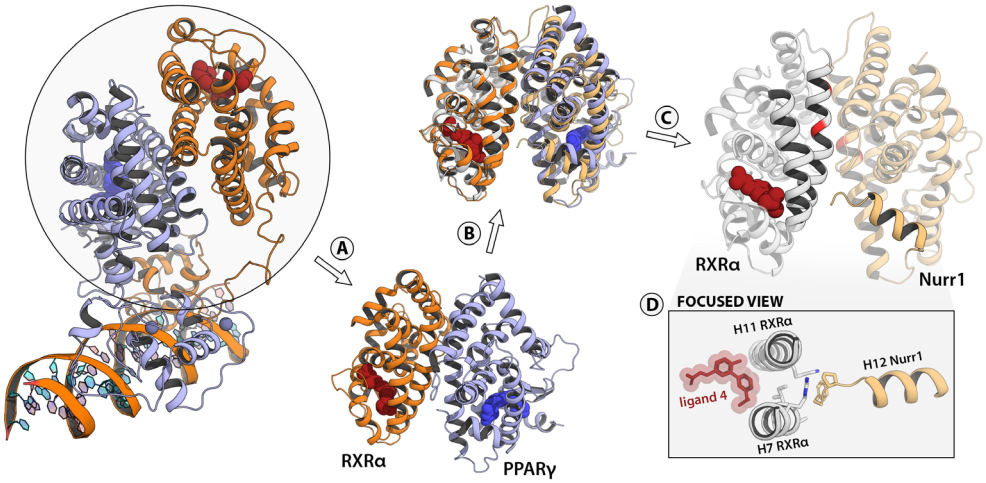

Figure 2 | Construction of the RXR-Nurr1 LBD heterodimer model. A. The LBDs of RXRα and PPARγ were extracted from the full-length RXRα-PPARγ heterodimer complex on DNA. **B.** The LBDs of Nurr1 (PDB: 1OVL) and RXRα in complex with ligand 4 (PDB: 5MKU) were superimposed on the RXRα-PPARγ LBDs. **C.** The final model of the RXRα-Nurr1 heterodimer with ligand 4 shown as red spheres. Mutations that are reported to abolish RXRα-Nurr1 heterodimerization are shown in red. Helix 12 of Nurr1 and helix 7 and 11 of RXRα are highlighted. **D.** Top view on the highlighted helices showing helix 12 of Nurr1 to be present at the dimerization interface and close to helix 7 and 11 of RXRα. Directly behind these RXRα helices, the RXRα-ligand is present.

accommodate helix 12 of Nurr1, a degree of flexibility of RXRα helix 7 and 11 is expected to be important. The heterodimer model shows that the flexibility of these helices is, in part, dependent on the presence and composition of the rexinoid (Figure 2D). The small molecule libraries used in the BRET-2 assay from both Scheepstra *et al.* and McFarland *et al.* showed reduced heterodimerization of RXRα-Nurr1 whenever steric bulk was introduced towards either helix 7 or 11 of RXRα.[4,8] In contrast, compact ligands like compound 4 (from now referred to as ligand 4) show a 25-fold preference for the heterodimeric complex over the homodimer (Figure S1).[4,8]

Tandem purification of the RXR-Nurr1 complex for crystallography

The purification procedures of the LBDs of RXRα and Nurr1 were optimized to obtain high yields and pure proteins. This resulted in a yield of 48 mg and 55 mg per liter of bacterial cell culture for RXRα and Nurr1, respectively, with a purity of >95% (Figure 3A). For the Nurr1 LBD, a pH-value of 8.5 (pH=~9.0 at 4 °C) of the purification buffer was essential to

obtain acceptable yield as a more acidic buffer (pH-values between 6.0-8.2) generally resulted in a yield of 1-2 mg per liter of cell culture.

The purified RXRα and Nurr1 LBDs and ligand 4 were combined in the presence or absence of an RXRα cofactor peptide and screened using multiple commercial crystallization suites (PACT Premium, JCSG+, NR-LBD and CRYOS). This resulted in octahedron-shaped crystals in a wide variety of conditions. The crystal structures were solved using crystals from multiple buffer conditions. However, the solved structures exclusively showed the RXRα monomer in complex with ligand 4 and a coactivator peptide.

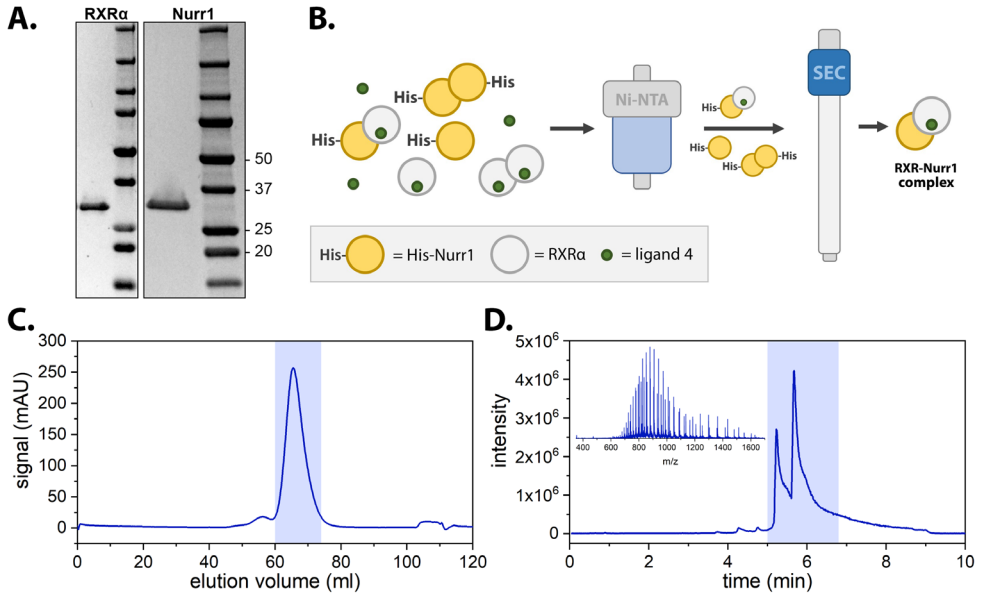

Figure 3 | Tandem purification of the RXR-Nurr1 complex. A. SDS-PAGE gel with the purified RXRα and Nurr1 in the left lane and a protein ladder in the right lane. **B.** His-Nurr1, RXRα and ligand 4 (stoichiometry 1:2:6 respectively) were purified using Ni-affinity chromatography to remove non-dimerized RXRα and excess ligand. Using size-exclusion chromatography (SEC), the heterodimeric complexes were separated from their monomeric subunits. Finally, thrombin cleavage was used to remove the purification tag, resulting in the purified RXRα-Nurr1 heterodimer complex. **C.** SEC chromatogram of the RXRα-Nurr1 complex after Ni-NTA purification. The blue highlighted area indicates the collected fractions **D.** LC/MS chromatogram of the RXRα-Nurr1 complex after SEC purification. The inserted graph shows the charge state distribution (m/z) of the primary peaks (highlighted blue area). Deconvoluted mass of the primary two peaks: 27235 Da and 32573 Da (theoretical masses 27235.50 Da and 32752.44 Da for RXRα and His-Nurr1, respectively).

The sample composition was improved by co-purifying the protein complex using a tandem purification technique (Figure 3B).[25] Purified His-Nurr1 was combined with a 2-fold excess of RXRα and a 6-fold excess of ligand 4. The solution was sequentially purified using Ni-affinity chromatography and SEC to obtain the purified heterodimer complex (Figure 3C). The Q-ToF LC/MS chromatogram of the purified product shows two distinct peaks, with the deconvoluted molecular masses of 27235 Da and 32573 Da corresponding to RXRα and His-Nurr1, respectively (Figure 3D). The presence of both proteins indicates that His-Nurr1 can heterodimerize with RXRα and the complex can be retained on the column under chromatography conditions.

The crystallization screen was repeated for the purified complex. Similar to the previous experiment, multiple conditions produced crystals with an octahedron morphology. However, some conditions produced small crystals with a cubic morphology. The solved crystal structure of these cubic crystals only showed RXRα in complex with ligand 4 and the coactivator peptide. The tandem purification was repeated in the absence of either ligand or coactivator peptide. In addition, other crystallization suites were added (AmSO4 and JCSG CORE I-IV) to improve the crystal growth of the heterodimeric complex. Unfortunately, these approaches were unsuccessful and exclusively resulted in crystals containing the RXRα-ligand 4 complex.

Design of a modular assay to quantify the impact of small molecules on RXR dimerization behavior

Previously, a BRET-2 assay format was used to determine the effect of rexinoid binding on the homo- and hetero-dimerization behavior of RXRα. This assay is performed in a cellular environment, which enhances the level of complexity due to the presence of compounds, cofactors and other proteins that can potentially influence the dimerization behavior of RXRα or its partner. To overcome this, an *in vitro* assay was designed that quantifies the direct interaction between the NR LBDs, removing all the other components. This assay makes use of a split-luciferase reporter system referred to as NanoBiT.[26] This technology uses a split version of the small and bright luciferase NanoLuc (19 kDa) that can be fused to proteins of interest (Figure 4A-B). The luciferase is split into a small peptide (SmBiT; 11 residues) and the rest of the enzyme (LgBiT; 157 residues) that separately do not produce a luminescent signal. Upon complementation of the fragments, the functionality is restored, producing a bright luminescent signal at a wavelength of 460 nm. A SmBiT

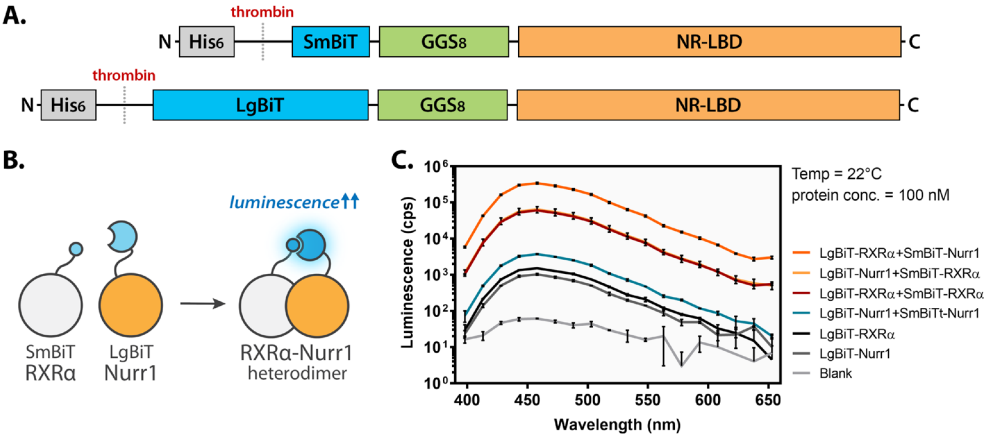

Figure 4 | Construction of the RXR-Nurr1 LBD heterodimer model. A. Design of the NanoBiT-NR protein constructs. **B.** Illustration of the NanoBiT assay format to quantify nuclear receptor dimerization. **C.** Wavelength scan of different combinations of NanoBiT fusion constructs LBD proteins. Monomers and the Nurr1 homodimer show a lower signal, which is consistent with the known monomeric activity of Nurr1. Measurements were performed in triplicate and the error bars show the SEM.

amino acid sequence was selected with a low intrinsic affinity for the LgBiT (K_D = 190 µM) to ensure that complementation of the reporter only occurs upon dimerization of the receptors.[26]

The NanoBiT-NR fusion constructs were designed using a GGS_8 linker between the N-terminus of the NR-LBD and the C-terminus of the NanoBiT fragment. In addition, an N-terminal His-tag with a thrombin cleavage site is added for purification purposes. Combining the purified SmBiT- and LgBiT-NR fusion proteins with furimazine (substrate) produced luminescence with a maximum intensity at a wavelength of 460 nm, which corresponds to the emission wavelength of the NanoLuc luciferase (Figure 4C). In particular, for the RXRα homo- and RXRα-Nurr1 heterodimer complexes, a high luminescent signal was observed, indicating the complexation of both receptors (Figure 4C). In comparison, the isolated LgBiT-NR fusion proteins generate a signal that is 50- to 250-fold weaker. The observed intensity of the interaction between SmBiT-Nurr1 and LgBiT-Nurr1 is similar to the intensity of the LgBiT alone, indicating that the Nurr1-LBD is primarily monomeric in solution (Figure 4C). In addition, a NanoBiT-construct of PPARα was prepared to determine if small molecules can induce distinct dimerization profiles for different RXR heterodimers.

General considerations for the NanoBiT complementation assay

The complemented NanoBiT luminescent signal intensity depends on various factors, including the protein concentration, the amount of available substrate and the temperature. Minor deviations in the amount of protein and substrate concentrations lead to a significantly different luminescent signal. Therefore, to qualitatively evaluate the impact of ligand binding on dimerization, the same stock solution of proteins and substrate is used, and the ligand is added right before measurement.

When a high concentration of a NanoBiT-ligated proteins is used, a progressive decrease in the luminescent signal is observed (Figure 5A). The high concentration of the active enzyme appears to rapidly deplete the substrate, lowering the available substrate for the enzyme and decreasing the luminescent signal. After 1 hour, the signal of the holoprotein (ligand-bound) and apo-protein is equalized. Upon adding fresh substrate, a higher luminescent signal is observed again for the apo-protein compared to the holoprotein. This shows that the relative signal does not change because of a kinetic effect but is caused by substrate depletion.

Moreover, the influence of temperature and protein sample dilution on the luminescent signal was analyzed. Varying the ligand volume added to the protein-substrate solution did not lead to an apparent change in the luminescent intensity (Figure 5B). However, the temperature had a significant effect on the luminescent signal. Similar

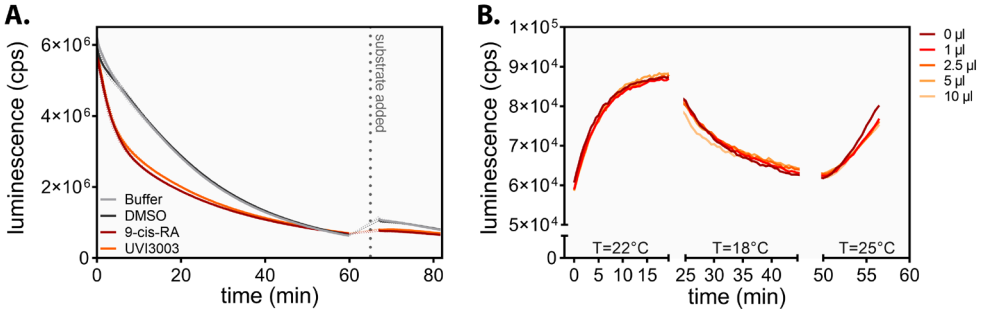

Figure 5 | Effect of substrate depletion and temperature on NanoBiT enzyme activity. A. Luminescence intensity at ~460 nm was measured over time for LgBiT-RXRα and SmBiT-Nurr1 (both 100 nM), with the addition of buffer, DMSO (0.01%), RXRα agonist 9-cis-RA (1µM) or RXRα antagonist UVI3003 (1µM). After ~60 minutes, fresh substrate was added. The restored luminescent profile indicates that the observed decrease is caused by substrate depletion. **B.** Luminescence intensity at 460 nm was measured over time. Different volumes of MilliQ (1-10 µl) were added to 1 nM LgBiT-RXRα and 1 nM SmBiT-PPARα supplied with 1000x diluted substrate. The temperature of the plate was adjusted during measurements at intervals of ~20 minutes.

to other enzymes, the activity of the NanoBiT complex increases upon higher temperatures within the physiological range.[27]

The protein and substrate concentrations were optimized to prevent substrate exhaustion. The furimazine substrate was used at the supplier's recommended concentration (1000x diluted). For RXRα-RXRα and RXRα-Nurr1, a protein concentration of 10 nM for both the SmBiT- and the LgBiT-NR fusion construct was used to produce a stable luminescent signal for one hour (Figure 6). The RXRα-PPARα complex produced a significantly more intense luminescent signal than RXRα-RXR and RXRα-Nurr1 at a protein concentration of 10 nM, accompanied by faster substrate depletion. Therefore, the protein concentration for the RXRα-PPARα complex was lowered to 1 nM, producing a stable signal for 30 minutes (Figure 6).

Two different rexinoids (LG100754 and LG101506) were supplemented to the protein-substrate solutions to determine whether rexinoids change the dimerization behavior of RXRα. The luminescent signal increase or decrease at the start of the measurement is produced by two factors: the temperature change of the microtiter plate and the protein-

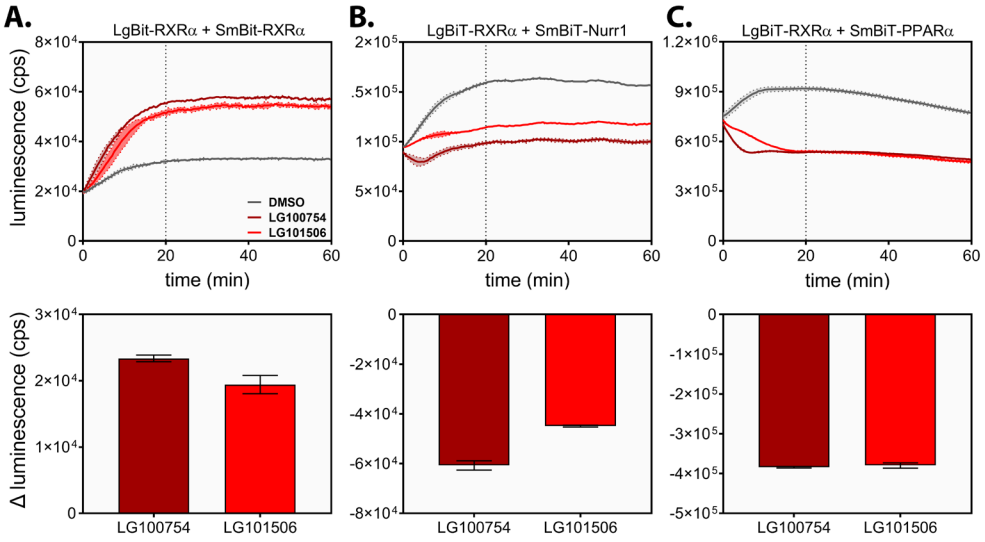

Figure 6 | Optimization of the RXRα dimerization assay using the NanoBiT technology. Luminescence intensity at 460 nm was measured over time upon addition of LG100754 (10 μM), LG101506 (10 μM) or DMSO for **A.** LgBiT-RXRα and SmBiT-RXRα (both at 10 nM) **B.** LgBiT-RXRα and SmBiT-Nurr1 (both at 10 nM) **C.** LgBiT-RXRα and SmBiT-PPARα (both at 1 nM). All measurements were performed in triplicate and the error bars show the SEM. The bottom graphs show the intensity difference with the DMSO control once a stable signal is reached.

ligand-binding equilibrium that needs to settle (Figure 6). Interestingly, each type of RXRα dimer responds differently to both ligands. For the RXRα homodimer, the luminescent signal significantly increases in the presence of both ligands, indicating that these ligands improve RXRα homodimerization. In contrast, for both heterodimer complexes, the luminescent signal decreases, suggesting that small molecules inhibit heterodimerization, potentially because of the competitive formation of the RXRα homodimer.

Because the signal intensity significantly depends on the protein concentration and the type of dimer analyzed, the changes in intensities cannot be compared across the dimer pairs. However, the intensity shift caused by ligand-binding can be compared for each dimer pair separately, as the change in luminescent intensity is directly correlated to the oligomeric state of the protein.

Rexinoid shape directs the RXRα dimerization behavior in a NanoBiT assay

A small library of high-affinity RXR ligands was produced with varying bulk towards either helix 7 or 11. To probe helix 7, analogs of ligand 4 were used, incorporating an incremental length of the alkyl tail (Figure 7A). These derivatives bind to RXRα with a high affinity, and the length of the alkyl chain appears to be correlated to the binding affinity for RXRα (Figure S1). For probing helix 11, a selection of commercial, high-affinity rexinoids were selected (Figure 7B and Table S1). Although the co-crystal structures were not available for all ligands, based on the structural similarities of the small molecules, a comparable binding mode is expected. From the available crystal structures of the helix 11 probing ligands, a displacement of helix 11 away from the LBP could be observed compared to the ligand 4 reference structure, thereby remodeling the dimerization surface (Figure 7D-G).

The ability of the ligands to direct the dimerization behavior of RXRα was investigated with the NanoBiT assay format. All ligands affected the luminescent intensity, indicating an altered abundance of the receptor's dimeric state. RXRα-RXRα, RXRα-Nurr1 and RXRα-PPARα responded differently to each of the ligands (Figure 8). For the ligand 4 derivatives, a modest decrease in the luminescent signal was observed for the RXRα homodimer (Figure 8A). In contrast, the luminescence incrementally decreased with the increasing size of the alkyl tail for RXR-Nurr1, indicating the destabilization of the heterodimer complex (Figure 8B). For the RXRα-PPARα heterodimer, the opposite behavior is observed. Here, the bulkier JV17 enhances the luminescent signal, while the compact PW95 decreases it (Figure 8C).

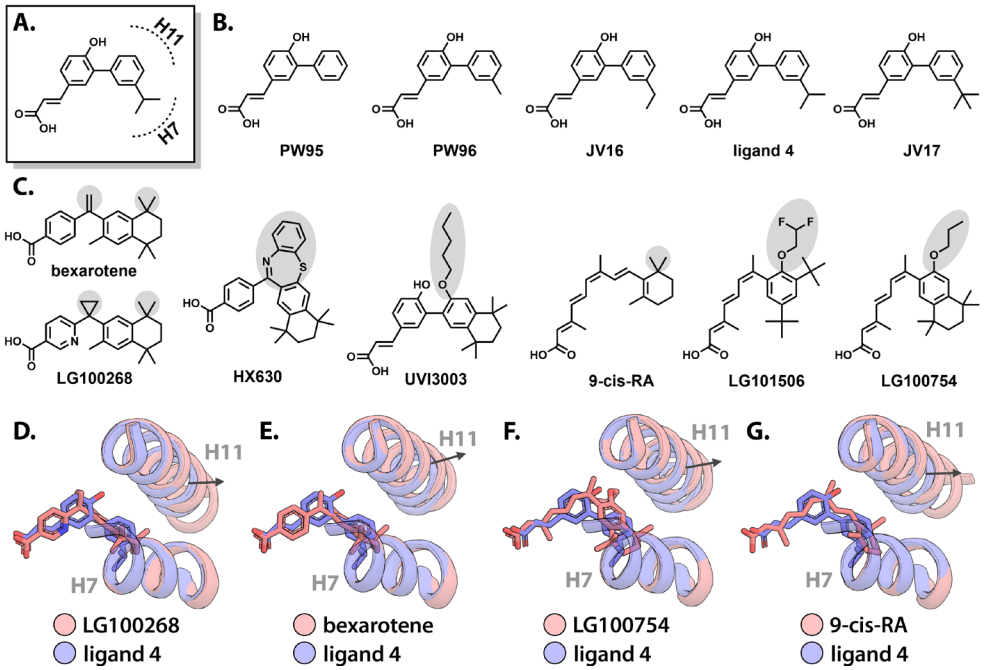

Figure 7 | RXRα ligands introducing steric bulk towards helix 7 or 11 of RXRα. A. Illustration of the ligand 4 and the relative position of helix 7 and helix 11 of RXRα. **B.** RXRα ligands that probe helix 7. **C.** RXRα ligands that probe helix 11. The parts of the ligands that introduce bulk towards helix 11 are highlighted in light grey. **D-G.** Comparison of the orientation of RXRα bound to ligand 4 (PDB: 5MKU; blue) and **D.** LG100268 (PDB: 1H9U) **E.** bexarotene (PDB: 4K6I) **F.** LG100754 (PDB: 6STI) **G.** 9-cis retinoic acid (PDB: 3OAP). The arrows indicate the direction of helix 11 displacements from the red structure compared to the blue structure (RXRα in complex with ligand 4).

The ligands probing helix 11 generally decrease the luminescence for both RXRα-Nurr1 and RXRα-PPARα (Figure 8B-C). However, the RXRα-Nurr1 and RXRα-PPARα heterodimers respond differently to the rexinoids. For example, LG100268 considerably reduced the luminescence of RXRα-Nurr1, while no effect was observed for the RXRα-PPARα heterodimer (Figure 8B-C). In contrast, LG101506 moderately decreased the signal for the RXRα-Nurr1 heterodimer while it generates the largest shift for RXRα-PPARα (Figure 8B-C). HX630 was the only ligand with bulk towards helix 11 that appears to stabilize the RXRα-PPARα heterodimer (Figure 8C). HX630 is an RXRα agonist that has been shown to selectively activate RXRα-PPARγ heterodimers.[28] Ligands that introduce bulk towards helix 11 significantly enhanced the luminescent signal of the RXRα homodimer (Figure 8A). Interestingly, rexinoids that introduce bulk towards helix 11 are

also known to destabilize the active conformation of helix 12.[8,20] The only two rexinoids behave similarly across all dimers are PW95 and PW96 (Figure 8). Both ligands are compact and do not contain bulky groups towards either helix 7 or 11 (Figure 7B).

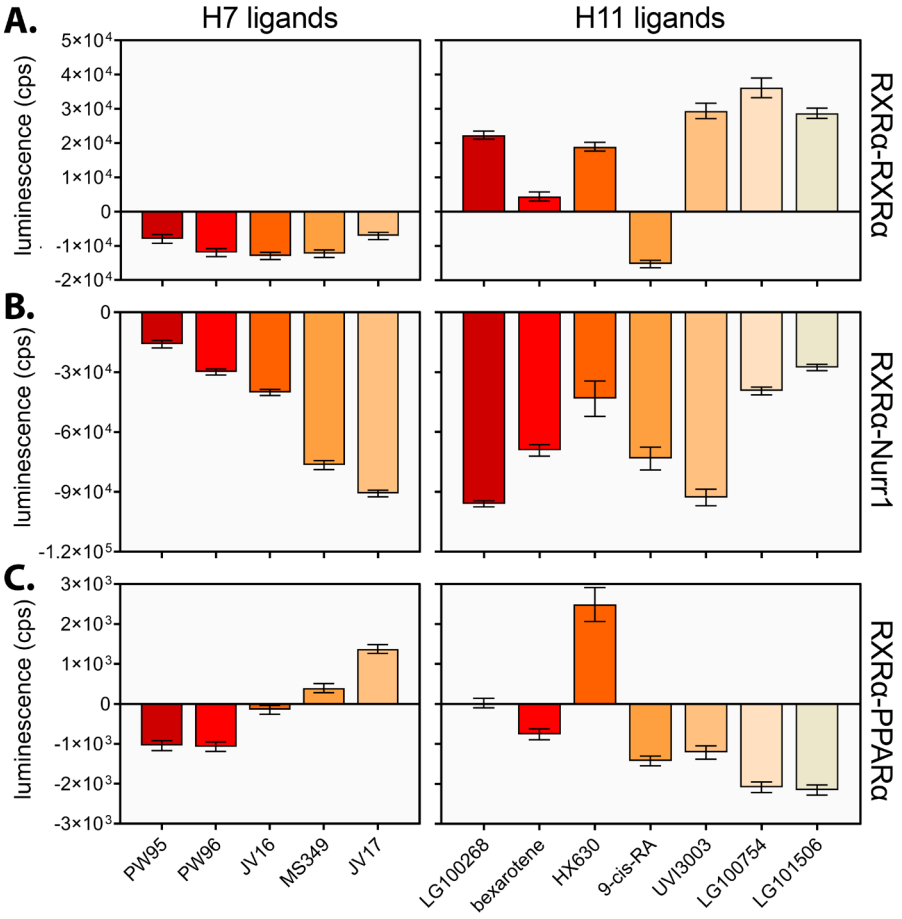

Figure 8 | Effect of rexinoid-binding on RXRα dimerization using a NanoBiT complementation assay. The bars represent the luminescent intensity difference with a DMSO control (triplicate measurements, error bars representing the SEM). **A.** RXRα-RXRα homodimer **B.** RXRα-Nurr1 heterodimer **C.** RXRα-PPARα heterodimer.

Conclusion

Regulation of RXR heterodimerization has proven to be promising for the treatment of disease.[3–5] Over the years, a wide variety of RXR ligands have been designed to bind RXR with a high affinity. Apart from receptor activation, rexinoids also showed to allosterically modulate the dimerization behavior of RXR via a yet unknown mechanism.[4,5,8–12] The RXRα-Nurr1 heterodimer model revealed that helix 12 of Nurr1 is present at the dimerization interface and is in close contact with helix 7 and 11 of RXRα. Our NanoBiT complementation assay was able to quantify the direct interaction between two NRs and confirmed that ligands could indeed change the dimerization behavior of RXRα. In agreement with the RXRα-Nurr1 model, the NanoBiT assay revealed that ligands introducing bulky groups towards either helix 7 or 11 of RXRα inhibit RXRα-Nurr1 heterodimerization. For RXRα-PPARα, bulk towards helix 7 showed to stabilize heterodimerization. These results suggest that the change in the dimerization is not only caused by the competitive formation of the RXRα homodimer but also by the ligands establishing a dimerization interface that is favored by specific NRs. Moreover, because the introduction of large groups on the rexinoid scaffold towards helix 7 and 11 does not appear to significantly alter the binding affinity of the rexinoid for RXRα[4,8], this suggests that this region of the LBP has a modulatory role.

Experimental Section

RXRα and Nurr1 expression and purification. Plasmids containing the RXRα (AA 223-462) and Nurr1 (AA 356-598) LBD were ordered from GenScript. The constructs were cloned into a pET15b vector using cloning sites NdeI and XhoI to introduce a N-terminal His-tag and a thrombin cleavage site. The plasmids were transformed into BL21 (DE3) using heat-shock and plated on agar plates with ampicillin. The next day, a single colony was picked and added to a 25 ml starter culture (LB medium). Cells grew overnight in a shaking incubator at 250 rpm and 37 °C. Next, the starter cultures were transferred to 2 L Terrific Broth (TB) medium supplied with 0.05% antifoam SE-15 (Sigma Aldrich) and 100 µg/ml ampicillin. When an OD600 of 1.0 was reached, the cultures were induced with 0.5 mM IPTG and placed back into the shaking incubator at 150 rpm at 18 °C overnight. Cell pellets were collected using centrifugation at 10.000 RCF for 10 minutes at 4 °C and resuspended in Buffer A1 (20 mM Tris (pH=8.0), 500 mM NaCl and 5 mM imidazole) for RXRα and Buffer A2 (25 mM Tris (pH=8.5), 100 mM NaCl, 20 mM imidazole, 1 mM Tris-(2-carboxyethyl)fosfine (TCEP) and 10% glycerol) for Nurr1, both supplemented with PMSF and 25 U/ml Benzonase® Nuclease (Millipore). The cell suspension was lysed using an Emulsiflex-C3 homogenizer (Avestin) and centrifuged at

40.000 RCF for 40 minutes at 4 °C to obtain the protein solution. These samples were loaded on separate 5 ml Ni-NTA Superflow Cartridge (QIAGEN) at 3 ml/min at 4 °C. The columns were washed with 10 column volumes (CVs) of buffer A and 10 CVs of buffer A with 50 mM imidazole. The purified proteins were eluted with 10 CVs of buffer A containing 200 mM imidazole. RXRα was buffer exchanged (10 mM Tris (pH=7.5), 150 mM NaCl and 5 mM DTT) and concentrated using an Amicon® Ultra centrifugal filter with a 10 kDa cutoff (Millipore). The purified Nurr1 was dialyzed to buffer B (25 mM Tris (pH=8.5), 200 mM NaCl, 1 mM TCEP and 5% glycerol) treated with 1.2 U/mg restriction-grade thrombin to remove the His-tag. The solution was loaded on a Superdex 75 pg 16/60 size-exclusion column (GE Life Sciences) using buffer B as running buffer. Fractions containing Nurr1 were concentrated and stored at -80 °C.

RXRα-Nurr1 complex purification. Purified RXRα, His-Nurr1 and ligand 4 were combined in a 2:1:6 stoichiometry and incubated for 1 hour on ice. A 1 ml Ni-NTA Superflow cartridge (QIAGEN) was equilibrated with buffer A (25 mM Tris (pH=8.0), 300 mM NaCl, 20 mM imidazole, 5% glycerol and 1 mM TCEP (pH=8.0)). The protein solution was loaded on the column. The column was washed with 10 CVs of buffer A and 10 CVs buffer A supplied with 45 mM imidazole. The product was eluted using 4 CVs of buffer A supplied with 200 mM imidazole. The solution was purified with SEC using 20 mM Tris (pH=8.0), 150 mM NaCl, 5% glycerol and 1 mM TCEP (pH=8.0) as the running buffer. The final product was concentrated and stored at -80 °C. SDS-PAGE and Q-ToF LC/MS were used to assess the sample composition.

NanoBiT proteins expression and purification. The SmBiT and LgBiT were N-terminally connected to the LBD of RXRα (AA 223-462), Nurr1 (AA 356-598) and PPARα (AA 200-468) via a GGS_8-linker. At the N-terminus, a His-tag with a thrombin cleavage side was added for purification purposes. All plasmids (pET21d(+)) were ordered from GenScript. Using heat shock, the plasmid was transformed into E.Coli BL21 (DE3) cells. A single colony was used to culture overnight at 37 °C in 8 ml of LB medium supplied with 100 µg/ml ampicillin. These cultures were transferred to 1 L of TB medium supplied with 0.05% antifoam SE-15 (Sigma Aldrich) with 100 µg/ml ampicillin. After an OD600 of 1.0 is reached, protein expression was induced by adding 1.0 mM IPTG. The protein expression continued overnight at 15°C. Using centrifugation at 10.000 RCF for 10 minutes at 4 °C, the cell pellet was collected and thereafter dissolved in lysis buffer (this buffer composition is different for every NR). The cells were lysed using an Emulsiflex-C3 homogeniser (Avestin) and the crude protein solution was obtained by centrifugation at 40.000 RCF for 40 minutes at 4°C. This solution was loaded on a 1 ml Ni-NTA Superflow cartridge (QIAGEN) which was equilibrated with buffer A (diff). The column was washed with 10 column volumes (CVs) of buffer A and 10 CVs of buffer A with 50 mM imidazole to eliminate unspecific binding of proteins to the resin. The product was eluted from the column using 8 CVs of buffer A with 200 mM imidazole. The elution fraction was dialysed overnight in buffer A without imidazole. In addition, 1.2 U/mg restriction-grade

thrombin was added to the purified protein sample to remove the purification tag. The purified sample was then concentrated using an Amicon® Ultra centrifugal filter with a 10 kDa cutoff (Millipore) and loaded on a Superdex 75 pg 16/60 size-exclusion column (GE Life Sciences) using buffer B as running buffer. The fractions containing the desired protein were collected, aliquoted and stored at -80 °C.

FITC labeled cofactor peptide synthesis. A FITC-labeled D22 peptide was synthesized (FITC- βA-LPYEGSLLLKLLRAPVEEV) using Fmoc solid-phase peptide synthesis (SPPS) making use of an automated multiple peptide synthesizer (Intavis MultiPep RSi). The peptides were synthesized using Rink amide AM resin (Novabiochem; 0.59 mmol/g loading). Deprotection of the residues was performed twice per cycle with 20% piperidine in DMF. This step was followed by two coupling steps (where HBTU was used as the activator and DIPEA as the base). After coupling the unreacted N-termini were acetylated (1:1:3 Ac2O/pyridine/DMF). The peptides were manually labeled with FITC (Sigma-Aldrich) using standard SPPS conditions. The peptide was cleaved from the resin using TFA/TIS/water (95:2.5:2.5) and precipitated in diethyl ether twice. The peptide was dissolved in 20% H2O in ACN + 0.1% TFA and purified using a mass directed auto purification system (preparative reversed-phase HPLC). After purification the peptides were lyophilized and stored at -30°C.

Fluorescence polarization assays. A dilution series of the ligands (100 µM – 48 pM) were made to a constant concentration of FL-RXRα (1 µM) and FITC-labeled D22 cofactor peptide (0.1 µM) in a 384-well low volume black round bottom plate (Corning®). The buffer contained 25 mM Tris (pH=7.8), 200 mM NaCl, 5 mM DTT and 0.1% (w/v) bovine serum albumin. Plates were incubated for 10 minutes at 4°C before the fluorescence polarization was measured with a Tecan Infinite F500 plate reader using an excitation and emission wavelength of 485 nm and 535 nm respectively. The experiment was performed in triplicate and the data were analyzed using GraphPad Prism 8.

Wavelength scan NanoBiT-NR fusion proteins. NanoBiT-LBD NR proteins were combined and diluted to a final concentration of 100nM in 25 mM Tris (pH=7.8), 200 mM NaCl, 1 mM TCEP and 0.1% BSA. After 5 minutes of incubation at room temperature, the samples were transferred to a white Thermo Fisher Nunc 384-well plate. Furimazine (substrate; 1000x diluted) was added and a wavelength scan was performed on a Tecan Spark plate reader at room temperature. The analysis was performed using GraphPad Prism 8.

NanoBIT assay. NanoBiT-LBD NR proteins were diluted a final concentration of 10 nM (1 nM for RXRα-PPARα) in 25 mM Tris (pH=7.8), 200 mM NaCl, 1 mM TCEP and 0.1% BSA. Substrate (1000x diluted) was added to the protein solution and transferred to a white Thermo Fisher Nunc 384-well plate. The plate incubated at room temperature for 5 minutes and just before measurement, all ligands were added simultaneously to the plate using a multichannel pipette. The emission was

measured at 460 nm on a Tecan Spark plate reader directly after. After 10 minutes, the luminescent signal stabilized and the intensity difference with the DMSO control was determined ($I_{ligand} - I_{DMSO}$). Measurements were performed at room temperature. The analysis was performed using GraphPad Prism 8.

Protein constructs

His6-RXRα (pET15b)

MGSSHHHHHHSSGLVPRGSHMTSSANEDMPVERILEAELAVEPKTETYVEANMGLNPSSPNDPVTNIC
QAADKQLFTLVEWAKRIPHFSELPLDDQVILLRAGWNELLIASFSHRSIAVKDGILLATGLHVHRNSA
HSAGVGAIFDRVLTELVSKMRDMQMDKTELGCLRAIVLFNPDSKGLSNPAEVEALREKVYASLEAYCK
HKYPEQPGRFAKLLLRLPALRSIGLKCLEHLFFFKLIGDTPIDTFLMEMLEAPHQMT

His6-Nurr1 (pET15b)

MGSSHHHHHHSSGLVPRGSHMVKEVVRTDSLKGRRGRLPSKPKSPQEPSPPSPPVSLISALVRAHVDS
NPAMTSLDYSRFQANPDYQMSGDDTQHIQQFYDLLTGSMEIIRGWAEKIPGFADLPKADQDLLFESAF
LELFVLRLAYRSNPVEGKLIFCNGVVLHRLQCVRGFGEWIDSIVEFSSNLQNMNIDISAFSCIAALAM
VT|ERHGLKEPKRVEELQNKIVNCLKDHVTFNNGGLNRPNYLSKLLGKLPELRTLCTQGLQRIFYLKL
EDLVPPPAIIDKLFLDTLPF

His6-LgBit-RXRα (pET21d)

MGSSHHHHHHSSGLVPRGSGGVFTLEDFVGDWEQTAAYNLDQVLEQGGVSSLLQNLAVSVTPIQRIVR
SGENALKIDIHVIIPYEGLSADQMAQIEEVFKVVYPVDDHHFKVILPYGTLVIDGVTPNMLNYFGRPY
EGIAVFDGKKITVTGTLWNGNKIIDERLITPDGSMLFRVTINSGGSGGSGGSGGSGGSGGSGGSGGSG
GSGGSTSSANEDMPVERILEAELAVEPKTETYVEANMGLNPSSPNDPVTNICQAADKQLFTLVEWAKR
IPHFSELPLDDQVILLRAGWNELLIASFSHRSIAVKDGILLATGLHVHRNSAHSAGVGAIFDRVLTEL
VSKMRDMQMDKTELGCLRAIVLFNPDSKGLSNPAEVEALREKVYASLEAYCKHKYPEQPGRFAKLLLR
LPALRSIGLKCLEHLFFFKLIGDTPIDTFLMEMLEAPHQMT

His6-LgBit-Nurr1 (pET21d)

MGSSHHHHHHSSGLVPRGSGGVFTLEDFVGDWEQTAAYNLDQVLEQGGVSSLLQNLAVSVTPIQRIVR
SGENALKIDIHVIIPYEGLSADQMAQIEEVFKVVYPVDDHHFKVILPYGTLVIDGVTPNMLNYFGRPY
EGIAVFDGKKITVTGTLWNGNKIIDERLITPDGSMLFRVTINSGGSGGSGGSGGSGGSGGSGGSGGSG
GSGGSVKEVVRTDSLKGRRGRLPSKPKSPQEPSPPSPPVSLISALVRAHVDSNPAMTSLDYSRFQANP
DYQMSGDDTQHIQQFYDLLTGSMEIIRGWAEKIPGFADLPKADQDLLFESAFLELFVLRLAYRSNPVE
GKLIFCNGVVLHRLQCVRGFGEWIDSIVEFSSNLQNMNIDISAFSCIAALAMVT|ERHGLKEPKRVEE
LQNKIVNCLKDHVTFNNGGLNRPNYLSKLLGKLPELRTLCTQGLQRIFYLKLEDLVPPPAIIDKLFLD
TLPF

His6-SmBit-RXRα (pET21d)

MGSSHHHHHHSSGLVPRGSGGVTGYRLFEEILGGSGGSGGSGGSGGSGGSGGSGGSGGSTSSANE
DMPVERILEAELAVEPKTETYVEANMGLNPSSPNDPVTNICQAADKQLFTLVEWAKRIPHFSELPLDD
QVILLRAGWNELLIASFSHRSIAVKDGILLATGLHVHRNSAHSAGVGAIFDRVLTELVSKMRDMQMDK
TELGCLRAIVLFNPDSKGLSNPAEVEALREKVYASLEAYCKHKYPEQPGRFAKLLLRLPALRSIGLKC
LEHLFFFKLIGDTPIDTFLMEMLEAPHQMT

His6-SmBit-Nurr1 (pET21d)

MGSSHHHHHHSSGLVPRGSGGVTGYRLFEEILGGSGGSGGSGGSGGSGGSGGSGGSGGSVKEVVR
TDSLKGRRGRLPSKPKSPQEPSPPSPPVSLISALVRAHVDSNPAMTSLDYSRFQANPDYQMSGDDTQH
IQQFYDLLTGSMEIIRGWAEKIPGFADLPKADQDLLFESAFLELFVLRLAYRSNPVEGKLIFCNGVVL
HRLQCVRGFGEWIDSIVEFSSNLQNMNIDISAFSCIAALAMVT|ERHGLKEPKRVEELQNKIVNCLKD
HVTFNNGGLNRPNYLSKLLGKLPELRTLCTQGLQRIFYLKLEDLVPPPAIIDKLFLDTLPF
ABCD = Purification tag

Supporting Information

Table S1 | Properties of the rexinoids targeting helix 11 of RXRα in the NanoBiT assay.

Name	Ligand Type	Affinity to RXRα	Reference
LG100268	RXRα agonist	EC_{50} = 150±40 nM	Scheepstra et al., J. Med. Chem. (2017)[8]
Bexarotene	RXRα agonist	K_i = 36 nM	Canan Koch et al., J. Med. Chem. (1999)[29]
HX630	RXRα agonist	EC_{50} = 900 nM	Umemiya et al., J. Med. Chem. (1997)[30]
9-cis-RA	RXRα agonist	EC_{50} = 100±425 nM	Allenby et al., PNAS (1993)[31]
UVI3003	RXRα antagonist	*nanomolar potent*	Nahoum et al., PNAS (2007)[32]
LG100754	RXRα antagonist	K_i = 3 nM	Canan Koch et al., J. Med. Chem. (1996) [33]
LG101506	RXRα antagonist	K_i = 3±2 nM	Michellys et al. J., Med. Chem (2003)[34]

Compound	RXR-Nurr1 pEC_{50}	RXR-RXR pEC_{50}	Fold Selectivity
LG100268	9.3 ± 0.3	8.2 ± 0.2	**12.6**
1	8.6 ± 0.2	7.5 ± 0.1	**12.6**
2	8.5 ± 0.2	7.5 ± 0.1	**10.0**
3	8.6 ± 0.2	7.7 ± 0.1	**7.9**
4	9.1 ± 0.4	7.7 ± 0.1	**25.1**
5	8.3 ± 0.2	7.0 ± 0.0	**20.0**
6	6.1 ± 0.2	6.8 ± 0.2	**0.2**
7	7.1 ± 0.4	7.5 ± 0.1	**0.4**
8	6.8 ± 0.2	7.7 ± 0.2	**0.1**

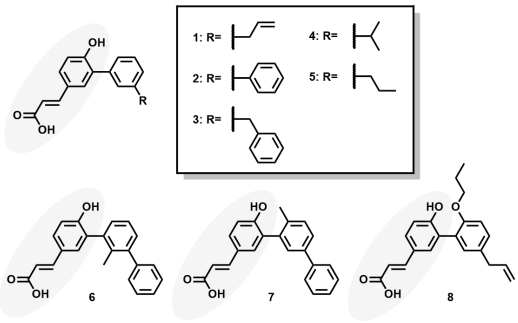

Figure S1 | BRET-2 assay to evaluate ligand-induced RXRα-RXRα homodimerization and RXRα-Nurr1 heterodimerization. The pEC_{50} is the negative logarithm of the EC_{50} in molar (e.g. if $EC_{50} = 10^{-6}$ M the pEC_{50} = 6). The values are the mean of three independent experiments and the error is shown as the SD. Data adapted from Scheepstra *et al.* (2017).[8]

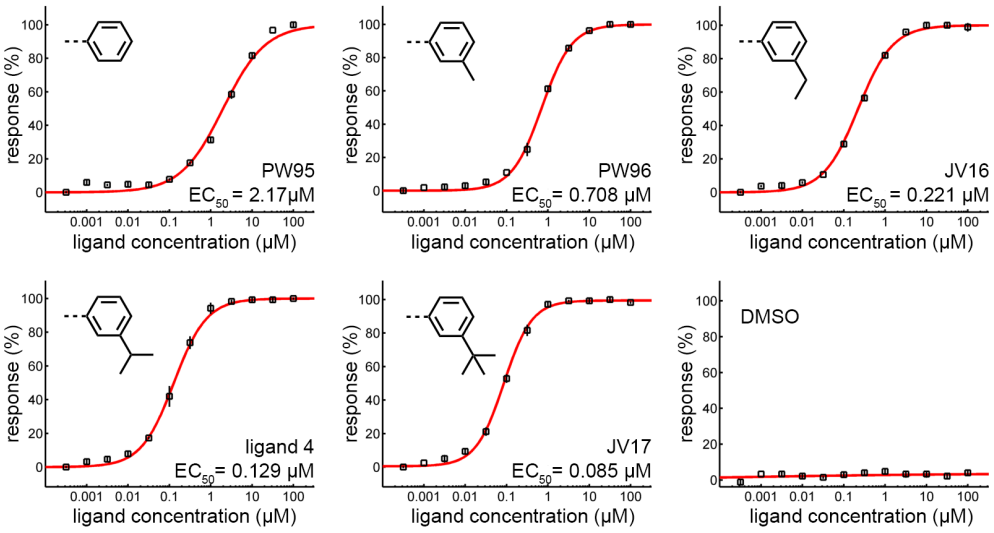

Figure S2 | FITC-labeled coactivator peptide recruitment assay of RXRα with ligand 4 derivatives. Agonist binding leads to recruitment of a FITC-labeled D22 coactivator peptide. Data measured in triplicate, datapoints showing the mean and the error bars represent the SD.

Acknowledgements

Anne de Dreu is greatly acknowledged for her work on the development and optimization of the NanoBiT assay. Johan Verhoeven, Pim Vendrig, Laureen de Bever and Timo Schaap are also greatly acknowledged for synthesizing the ligand 4 derivatives used in this chapter. Lech-Gustav Milroy is acknowledged for his input on the project design and the valuable discussions.

References

1. Kliewer, S. A., Umesono, K., Mangelsdorf, D. J. & Evans, R. M. Retinoid X receptor interacts with nuclear receptors in retinoic acid, thyroid hormone and vitamin D3 signalling. *Nature* **355**, 446–449 (1992).
2. Evans, R. M. & Mangelsdorf, D. J. Nuclear Receptors, RXR, and the Big Bang. *Cell* **157**, 255–66 (2014).
3. Dawson, M. I. & Xia, Z. The retinoid X receptors and their ligands. *Biochimica et Biophysica Acta - Molecular and Cell Biology of Lipids* vol. 1821 21–56 (2012).
4. McFarland, K. *et al.* Low Dose Bexarotene Treatment Rescues Dopamine Neurons and Restores Behavioral Function in Models of Parkinson's Disease. *ACS Chem. Neurosci.* **4**, 1430–1438 (2013).
5. Cesario, R. M. *et al.* The Rexinoid LG100754 Is a Novel RXR:PPARγ Agonist and Decreases Glucose Levels in Vivo . *Mol. Endocrinol.* **15**, 1360–1369 (2001).
6. Gampe, R. T. *et al.* Asymmetry in the PPARγ/RXRα Crystal Structure Reveals the Molecular Basis of Heterodimerization among Nuclear Receptors. *Mol. Cell* **5**, 545–555 (2000).

7. Kojetin, D. J. *et al.* Structural mechanism for signal transduction in RXR nuclear receptor heterodimers. *Nat. Commun.* **6**, 8013 (2015).
8. Scheepstra, M. *et al.* Ligand Dependent Switch from RXR Homo- to RXR-NURR1 Heterodimerization. *ACS Chem. Neurosci.* **8**, (2017).
9. Repa, J. J. *et al.* Regulation of absorption and ABC1-mediated efflux of cholesterol by RXR heterodimers. *Science* vol. 289 1524–1529 (2000).
10. le Maire, Teyssier, Balaguer, Bourguet & Germain. Regulation of RXR-RAR Heterodimers by RXR- and RAR-Specific Ligands and Their Combinations. *Cells* **8**, 1392 (2019).
11. Spathis, A. D. *et al.* Nurr1:RXRα heterodimer activation as monotherapy for Parkinson's disease. *Proc. Natl. Acad. Sci. U. S. A.* **114**, 3999–4004 (2017).
12. Giner, X. C., Cotnoir-White, D., Mader, S. & Lévesque, D. Selective ligand activity at Nur/retinoid X receptor complexes revealed by dimer-specific bioluminescence resonance energy transfer-based sensors. *FASEB J.* **29**, 4256–4267 (2015).
13. Castillo, S. O. *et al.* Dopamine biosynthesis is selectively abolished in substantia nigra/ventral tegmental area but not in hypothalamic neurons in mice with targeted disruption of the Nurr1 gene. *Mol. Cell. Neurosci.* **11**, 36–46 (1998).
14. Kim, C. H. *et al.* Nuclear receptor Nurr1 agonists enhance its dual functions and improve behavioral deficits in an animal model of Parkinson's disease. *Proc. Natl. Acad. Sci. U. S. A.* **112**, 8756–8761 (2015).
15. Castro, D. S., Arvidsson, M., Bolin, M. B. & Perlmann, T. Activity of the Nurr1 carboxyl-terminal domain depends on cell type and integrity of the activation function 2. *J. Biol. Chem.* **274**, 37483–37490 (1999).
16. Wang, Z. *et al.* Structure and function of Nurr1 identifies a class of ligand-independent nuclear receptors. *Nature* **423**, 555–560 (2003).
17. de Vera, I. M. S. *et al.* Defining a Canonical Ligand-Binding Pocket in the Orphan Nuclear Receptor Nurr1. *Structure* **27**, 66-77.e5 (2019).
18. Forman, B. M., Umesono, K., Chen, J. & Evans, R. M. Unique response pathways are established by allosteric interactions among nuclear hormone receptors. *Cell* **81**, 541–550 (1995).
19. Chandra, V. *et al.* Structure of the intact PPAR-γ–RXR-α nuclear receptor complex on DNA. *Nature* **456**, 350–356 (2008).
20. Sato, Y. *et al.* The 'phantom effect' of the rexinoid LG100754: Structural and functional insights. *PLoS One* **5**, (2010).
21. Lou, X. *et al.* Structure of the retinoid X receptor α-liver X receptor β (RXRα-LXRβ) heterodimer on DNA. *Nat. Struct. Mol. Biol.* **21**, 277–281 (2014).
22. Wang, N., Zou, Q., Xu, J., Zhang, J. & Liu, J. Ligand binding and heterodimerization with retinoid X receptor (RXR) induce farnesoid X receptor (FXR) conformational changes affecting coactivator binding. *J. Biol. Chem.* **293**, 18180–18191 (2018).
23. Chandra, V. *et al.* The quaternary architecture of RARβ-RXRα heterodimer facilitates domain-domain signal transmission. *Nat. Commun.* **8**, 1–9 (2017).
24. Aarnisalo, P., Kim, C. H., Lee, J. W. & Perlmann, T. Defining requirements for heterodimerization between the retinoid X receptor and the orphan nuclear receptor Nurr1. *J. Biol. Chem.* **277**, 35118–35123 (2002).
25. Bourguet, W. *et al.* Crystal structure of a heterodimeric complex of RAR and RXR ligand-binding domains. *Mol. Cell* **5**, 289–298 (2000).
26. Dixon, A. S. *et al.* NanoLuc Complementation Reporter Optimized for Accurate Measurement of Protein Interactions in Cells. *ACS Chem. Biol.* **11**, 400–408 (2016).
27. Peterson, M. E., Daniel, R. M., Danson, M. J. & Eisenthal, R. The dependence of enzyme activity on temperature: Determination and validation of parameters. *Biochem. J.* **402**, 331–337 (2007).

28. Nishimaki-Mogami, T. *et al.* The RXR agonists PA024 and HX630 have different abilities to activate LXR/RXR and to induce ABCA1 expression in macrophage cell lines. *Biochem. Pharmacol.* **76**, 1006–1013 (2008).
29. Koch, S. S. C. *et al.* Synthesis of retinoid X receptor-specific ligands that are potent inducers of adipogenesis in 3T3-L1 cells. *J. Med. Chem.* **42**, 742–750 (1999).
30. Umemiya, H. *et al.* Regulation of retinoidal actions by diazepinylbenzoic acids. Retinoid synergists which activate the RXR-RAR heterodimers. *J. Med. Chem.* **40**, 4222–4234 (1997).
31. Allenby, G. *et al.* Retinoic acid receptors and retinoid X receptors: Interactions with endogenous retinoic acids. *Proc. Natl. Acad. Sci. U. S. A.* **90**, 30–34 (1993).
32. Nahoum, V. *et al.* Modulators of the structural dynamics of the retinoid X receptor to reveal receptor function. *Proc Natl Acad Sci U S A* **104**, 17323–17328 (2007).
33. Koch, S. S. C. *et al.* Identification of the first retinoid X receptor homodimer antagonist. *J. Med. Chem.* **39**, 3229–3234 (1996).
34. Michellys, P. Y. *et al.* Novel (2E,4E,6Z)-7-(2-alkoxy-3,5-dialkylbenzene)-3-methylocta-2,4,6-trienoic acid retinoid X receptor modulators are active in models of type 2 diabetes. *J. Med. Chem.* **46**, 2683–2696 (2003).

CHAPTER 3

ERRα Influences the Transcriptional Activity of PPARα by a Direct Interaction

Abstract

The peroxisome proliferator-activated receptor α (PPARα) and the estrogen-related receptor α (ERRα) are two nuclear receptors that play essential roles in the regulation of mammalian oxidative metabolism. Researchers from Ghent University recently showed strong evidence for a direct interaction between both receptors. ERRα was revealed to act as a rheostat, fine-tuning the activity of PPARα and the associated transcription of PPARα-related genes. However, the interaction was observed in biological assays performed in, or derived from cells, which raises the possibility that other small molecules and proteins play a role in this interaction. In this chapter, the direct physical interaction between these two nuclear receptors is validated using isolated receptor protein constructs in an *in vitro* environment. A His-tag pulldown assay was developed and demonstrated that the full-length ERRα is required to interact with the PPARα LBD. Moreover, this interaction was shown to occur independently of the presence of the receptor ligands.

Part of this work will be published as:

1. Desmet, S. J., Thommis, J., de Vries, R. M. J. M., et al. ERRα functions as a rheostat of PPARα transcriptional activity controlling energy metabolism gene expression. *Submitted.*

Introduction

The nuclear receptor (NR) family plays an essential role in the regulation of cellular energy metabolism. The peroxisome proliferator-activated receptors (PPARs), liver X receptors (LXRs) and retinoid X receptors (RXRs) are activated by interacting with diet-derived small molecules such as fatty acids and bile acids.[1,2] The interaction with these ligands leads to downstream regulation of target genes that synthesize or catabolize these dietary ligands. The PPAR family consists of three isoforms: PPARα, PPARβ and PPARγ, which regulate genes involved in lipid metabolism, adipogenesis and inflammation. Despite the sequence and structural homology within this subfamily, each isoform is involved in the regulation of different pathways and respond to distinct ligands.[3,4] PPARα is expressed in the liver and brown adipose tissue and regulates genes involved in fatty acid transport and oxidation (FAO).[3,5] PPARγ, on the other hand, is expressed in both brown and white adipose tissue and has been labeled as a master regulator of adipogenesis and plays an essential role in lipid metabolism and insulin sensitivity.[3,6]

The orphan NR estrogen-related receptors (ERRs) also play an essential role in energy homeostasis, controlling oxidative metabolism. Like Nurr1, ERRα is an intrinsically active nuclear receptor of whose activity can be inhibited by an inverse agonist. Inhibition of ERRs has been demonstrated to be beneficial in diabetic mouse models.[7] Conversely, the PPARγ coactivator-1α (PGC-1α) was shown to enhance the transcriptional activity of ERRα.[8,9] Despite ERR sharing high sequence similarity with the estrogen receptor (ER), ERR cannot interact with estrogens and is, for this reason, occasionally referred to as the energy-related receptor.[9]

Circumstances that enhance FAO, like fasting, increase the expression and activity of ERRα, PPARα and their shared coactivator PGC-1α. Although both ERRα and PPARα each regulate their unique set of target genes, there are also overlapping target genes that modulate oxidative metabolism in liver.[10–12] This includes the regulation of pyruvate dehydrogenase kinase 4 (PDK4), a protein that regulates FAO and fatty acid synthesis.[10–12]

Recently, Sofie Desmet and coworkers from Ghent University demonstrated that the regulation between these two NRs occurs in an even more direct manner, through a direct interaction between the two receptors.* In this study, Array-MAPPIT (MAmmalian Protein-Protein Interaction Trap[13,14]) two-hybrid screening was used to identify interaction

* Manuscript submitted and under review.

partners of activated PPARα in a cellular context. From the 8500 "preys", ERRα was one of the proteins that interacted with PPARα in the presence of the PPARα-selective agonist GW7647.[15] This interaction was confirmed with a binary MAPPIT assay, co-immunoprecipitation experiments and a GST-pulldown assay (using *in vitro* translated ERRα from reticulocyte lysate). In a cellular setting, the interaction between ERRα and PPARα was demonstrated to be GW7647-dependent, while *in vitro*, the interaction was revealed to be independent of PPARα activation. The ERRα-specific inverse agonist compound 29 (C29)[10] significantly inhibited ERRα-PPARα heterodimerization under serum-starved conditions, despite the presence of GW7647 (Figure S1). Binding of inverse agonists like C29 or XCT790[16] to ERRα is known to reorient helix 12 to interact with its coactivator binding groove, preventing coactivator binding.[10,17] The combination of GW7647 and C29 significantly increased the mRNA levels of PPARα target genes (CPT1α

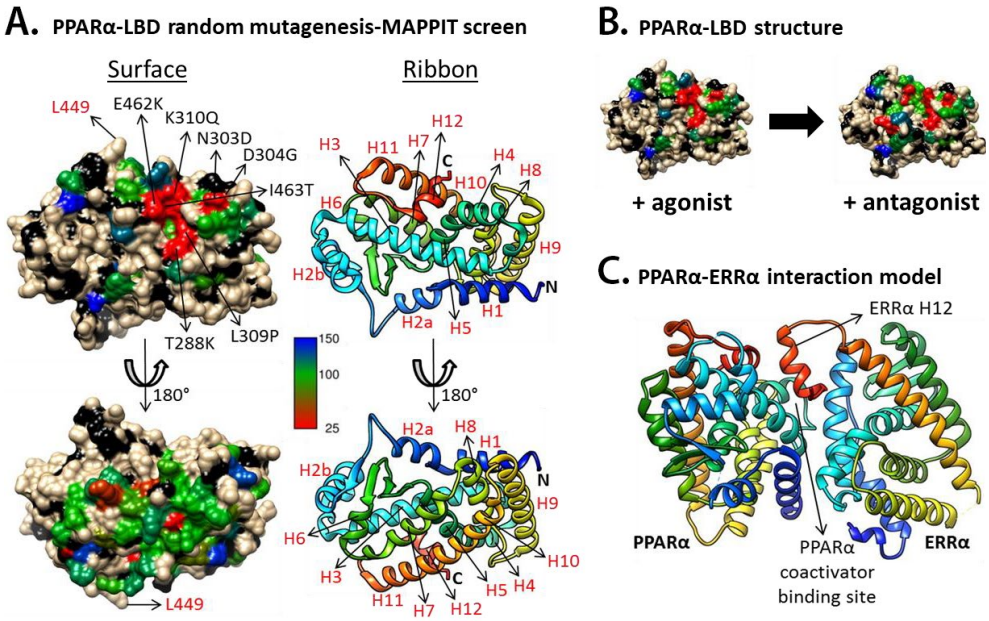

Figure 1 | ERRα directly interacts with the coactivator binding site of PPARα. A. Two orientations of the crystal structure of the PPARα-LBD (PDB: 2P54), with Leu449 as a point of reference. The residues were colored using a gradient that corresponds to the relative MAPPIT signals (as % of the wildtype), ranging from <25% (red) to >150% (blue). Backbone residues and non-mutated residues were colored black and light brown, respectively. The cartoon on the right shows the secondary structure of the structure. **B.** Comparison of the MAPPIT results mapped on the agonist (PDB: 2P54) and antagonist-bound (PDB: 1KKQ) PPARα-LBD. **C.** Molecular model of the ERRα-PPARα heterodimer. In this model, helix 12 of ERRα-LBD binds directly to the coactivator binding site of PPARα-LBD (PDB: 2P54).

and PDK4) compared to GW7647 alone, which further exemplified the cross-talk between both receptors (Figure S2).

Lastly, Desmet *et al.* elucidated the interaction surface between ERRα and PPARα by combining MAPPIT and random mutagenesis of PPARα. The interaction between ERRα and a collection of single (and some double) mutated PPARα was determined using the MAPPIT assay in the presence of GW7647. Mutations that strongly inhibited the interaction between both proteins were located in the AF-2 site of PPARα (Figure 1A-B). The authors proposed that helix 12 of ERRα interacts with the AF-2 site of the activated PPARα, a binding mode which has been observed in several dimeric NR complexes.[18–22] Mutations of key residues on helix 12 of ERRα indeed abolished the interaction with PPARα completely (Figure S3).

The work by Desmet and coworkers details the modulatory effect of ERRα on PPARα activity, a type of regulation that, to some extent, resembles the modulatory function of the universal NR heterodimer modulator RXR.[23] Although the interaction between both proteins has been demonstrated using various techniques, the assays were performed in, or derived from, a cellular environment. Therefore, other cell components could participate in stabilizing or inhibiting the interaction between these two receptors. In this chapter, the interaction between ERRα and PPARα will be further explored by isolating both receptors from all other components to study the direct interaction of these proteins *in vitro*. Desmet *et al.* used the full-length protein for their experiments, but the model suggests that the LBDs are the driving force of this interaction. Because purification and crystallization of single domains are more straightforward than of the full-length protein, both receptors' LBDs will be used as a starting point.

Results and Discussion

Purification of the ERRα-PPARα heterodimer complex for crystallography

The tandem purification method used in Chapter 2 was shown to be a successful method to isolate heterodimeric NR complexes. The tandem purification method was modified by substituting the size-exclusion chromatography (SEC) step with a Strep-Tactin column to overcome a potential dilution effect due to the large volume of the SEC-column (Figure 2A). First, the His-ERRα and Strep-PPARα LBDs were separately purified. ERRα produced

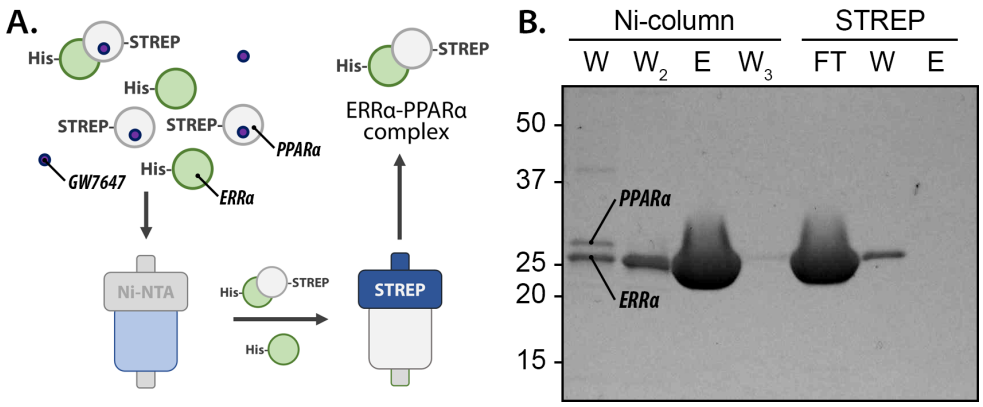

Figure 2 | Tandem purification of the ERRα-PPARα LBD-only complexes. A. His-ERRα, Strep-PPARα and GW7647 (stoichiometry 1:1:6 respectively) were purified using Ni-affinity chromatography to remove non-dimerized Strep-PPARα and excess ligand. Next, a Strep-Tactin column removes His-ERRα that is not in complex with Strep-PPARα, resulting in the purified ERRα-PPARα complex. **B.** SDS-PAGE analysis of the tandem purification. STREP-PPARα appears in the first washing step (W) of the Ni-NTA column, but not in any of the other chromatography steps. His-ERRα is most abundantly present in the elution step of the Ni-NTA column (E) and the flow-through step of the Strep-Tactin column (FT). Abbreviations: flow-through (FT), wash step ($W_{\#}$), product elution (E) and Strep-Tactin column (STREP).

high yields (60 mg per liter of cell culture), while lower yields were observed for Strep-PPARα (8-10 mg per liter cell culture). The purified proteins were combined and purified using the tandem purification method in the presence of GW7647. Gel electrophoresis showed that the elution fraction of the Ni^{2+}-column only contained His-ERRα, and only a faint band is observed for Strep-PPARα in the first washing step (Figure 2B). His-ERRα was also almost exclusively observed in the flow-through fraction of the Strep-Tactin column. Moreover, no product is present in the elution fraction of the Strep-Tactin column, demonstrating that His-ERRα is unable to retain Strep-PPARα on the Ni^{2+}-column (Figure 2A-B). The tandem purification was repeated, starting from the combined cell lysate. The SDS-PAGE analysis showed an identical profile as in the first attempt. These results suggest that there is weak or no interaction between the two LBDs under the purification conditions used. Crystallography was attempted by combining the purified proteins directly, but this did not yield crystal growth across multiple commercial crystallization screens (PACT Premium, JCSG+, JCSG Core I-IV, NR-LBD, $AmSO_4$, ProPlex and CRYOS).

ERRα-helix 12 peptide does not physically interact with the AF-2 site of PPARα

Using solid-phase peptide synthesis, a peptide was synthesized incorporating the C-terminal residues of ERRα (ERRα-H12; residue 409-423) to study the interaction of helix 12 of ERRα with the AF-2 site of PPARα (Figure 1C). A fluorescence polarization (FP) assay format was used to detect the interaction between PPARα and the peptide. The PPARα LBD was able to interact with a fluorophore-labeled PGC-1α coactivator peptide upon increasing concentrations of GW7647 (Figure 3A). However, GW7647 did not induce the binding of the labeled ERRα-H12 peptide (Figure 3B). In a competitive FP format, unlabeled ERRα-H12 peptide was also unable to displace fluorescein-labeled PGC-1α (Figure 3C). Only at the highest concentration of ERRα-peptide (25 μM), a minor decrease of the fluorescent signal is observed, which is within the margin of error of the assay. These results suggest that there is weak or no interaction between helix 12 of ERRα and the PPARα LBD. Therefore, additional features of the ERRα protein appear to be required to initiate the interaction with PPARα.

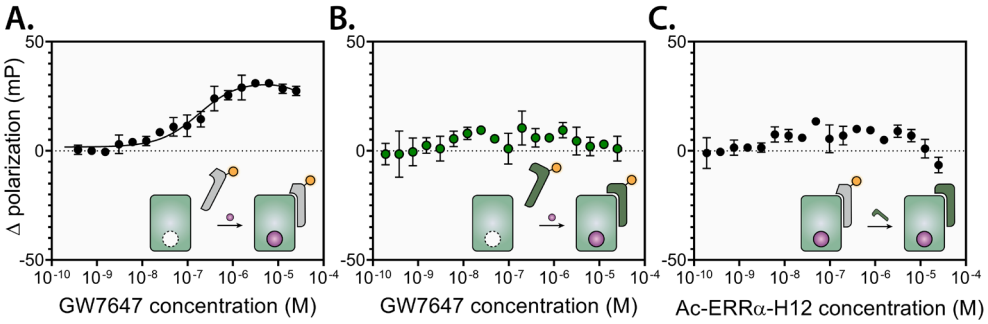

Figure 3 | Fluorescence polarization assay data with the assay schematic as an insert. A. The PPARα agonist GW7647 (purple sphere) titrated to a constant concentration of PPARα (green rectangle) and fluorescein-labeled PGC-1α (grey shape with yellow tag). **B.** GW7647 titrated to a constant concentration of PPARα and fluorescein-labeled ERRα-H12 peptide (dark green shape with yellow tag). **C.** ERRα-H12 peptide titrated to a constant concentration of PPARα, GW7647 and fluorescein-labeled PGC-1α. All polarization values were corrected for the polarization signal in the absence of protein. Data plotted as the average value and SD of three experimental replicates.

NanoBiT assay for the ERRα-PPARα heterodimer complex

The physical interaction between the LBDs of ERRα and PPARα was determined using the NanoBiT assay format described in Chapter 2. The SmBiT and LgBiT fragments were N-

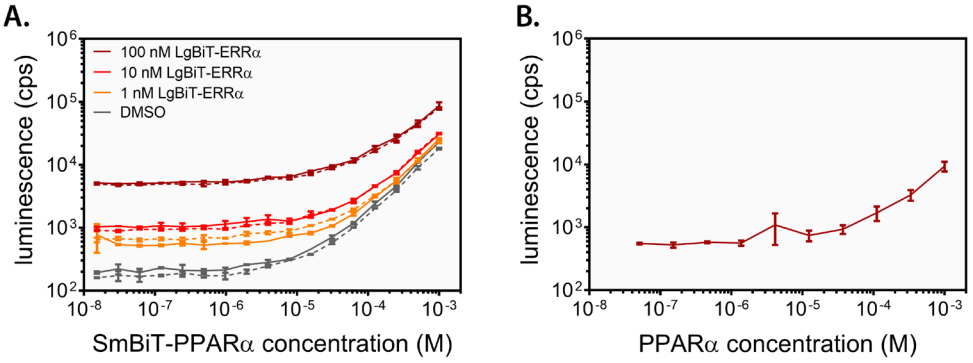

Figure 4 | Characterization of the interaction between the LBDs of ERRα and PPARα with NanoBiT. Luminescence intensity scan at 460 nm of **A.** Titration of SmBiT-PPARα to varying concentrations of LgBiT-ERRα (0, 1, 10 and 100 nM) and 10 μM GW7647 (slid lines). The dashed line represents the values in the absence of GW7647. **B.** Titration of Strep-PPARα to a constant concentration of furimazine (substrate). Data plotted as the average value and SD of three experimental replicates.

terminally fused to PPARα and ERRα with a GGS_8 linker. The interaction between the receptors was analyzed by titrating SmBiT-PPARα to varying concentrations of LgBiT-ERRα (0, 1, 10 and 100 nM) in the presence and absence of GW7647. All binding curves display a similar profile; a constant signal that starts to gradually increase at 10 μM of SmBiT-PPARα (Figure 4A). The addition of GW7647 did not alter the binding behavior of the NRs. Moreover, the luminescent signal is 100- to 1000-fold lower than the complexes described in Chapter 2 at the same protein concentration. The most significant difference is observed in the starting value of the lower asymptotic plateau, which is caused by the background luminescence of the LgBiT protein. Notably, the negative control (DMSO) shows a trend similar to the conditions containing LgBiT-ERRα (Figure 4A). Therefore, the gradual increase of the luminescent signal is likely to be produced by SmBiT-PPARα rather than heterodimerization. The fact that the SmBiT fragment is not able to convert the substrate suggests that the PPARα LBD is responsible for the increased fluorescence. Titration of Strep-PPARα to a constant concentration of substrate indeed produced binding curves identical to that of the NanoBiT construct, confirming that PPARα can bind and, to some extent, convert furimazine and produce a luminescent signal (Figure 4B). Together, the results of this NanoBiT assay give a strong indication that there is no direct physical interaction between the LBDs of ERRα and PPARα.

Purification of full-length ERRα

After the preceding results were produced, Desmet *et al.* applied MAPPIT to show that instead of ERRα LBD alone, full-length ERRα was required to interact with PPARα *in cellulo*. The ERRα LBD and other N-terminally truncated variants (LBD + hinge region and LBD + hinge region + DBD) demonstrated very weak to no interaction with PPARα. In contrast, for PPARα, the LBD alone was enough to interact with ERRα.

The full-length ERRα protein was produced using a construct and purification method described before.[24] Full-length ERRα was expressed with a C-terminal His-tag and purified using Ni^{2+}-affinity chromatography. The purification method resulted in a low yield of 3 mg per liter cell culture of the purified product. However, poor yields for full-length NRs occur more often because of reduced stability, low solubility and aggregation.[25–27] In the paper describing the full-length protein purification, the protein was used to detect antibody binding, but the bacterially-expressed protein's biological activity was not determined. The ERRα-selective inverse agonist XCT790 was titrated to the full-length ERRα to determine if the bacterially-expressed protein preserved biological activity in terms of ligand binding. XCT790 displaced a fluorophore-labeled coactivator peptide in a dose-dependent manner, showing that the bacterially expressed protein retains ligand-binding capacities after purification (Figure 5).

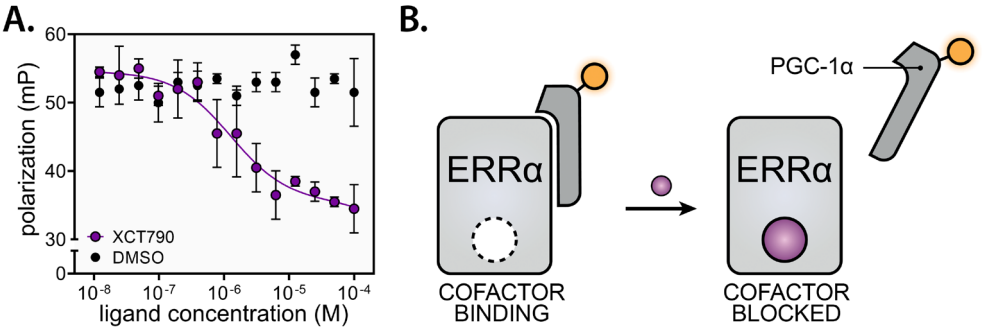

Figure 5 | Fluorescence polarization assay with FL-ERRα. A. The ERRα-specific inverse agonist XCT790 was titrated to a constant concentration of full-length ERRα with fluorescein-labeled PGC-1α cofactor peptide (dark grey shape with yellow tag). Upon binding the ligand, helix 12 of ERRα changes from the active conformation to an inactive conformation, releasing the PGC-1α cofactor peptide. Data plotted as the average value and SD of three experimental replicates. **B.** Assay schematic of (**A**).

Design of an in vitro His-tag pulldown assay to determine NR heterodimerization

A His-tag pulldown assay was developed to determine the direct interaction between full-length ERRα and PPARα LBD (Figure 6A). First, Ni-NTA magnetic beads were incubated with His-tagged ERRα. By applying a magnetic field to the sample, the His-ERRα-bound beads can be isolated while the buffer is exchanged, or other protein solutions are added.

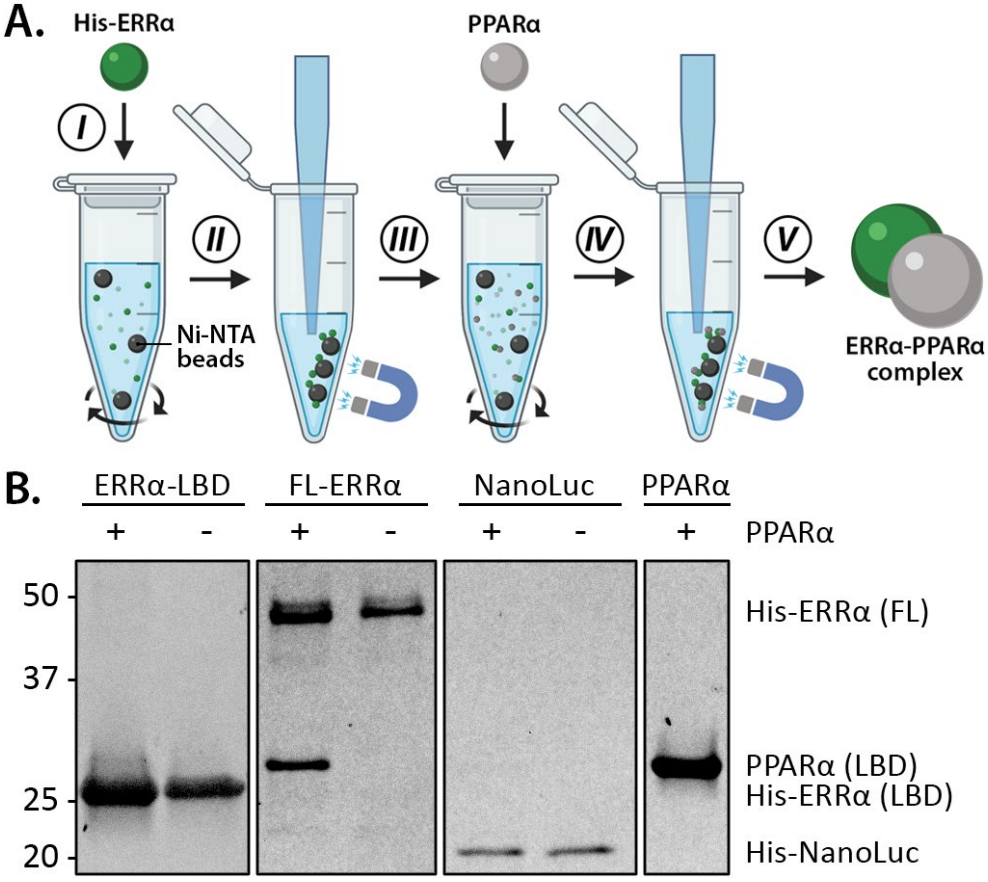

Figure 6 | His-tag pulldown to analyze the direct interaction between PPARα-LBD and (full-length) His-ERRα. A. Schematic of the His-tag pulldown assay. (i) His-tagged ERRα is incubated with the magnetic Ni-NTA beads. (ii) The beads, and the His-tagged protein, are pulled down using a magnet, the supernatant is extracted, and the beads are washed with buffer. (iii) PPARα is added to the solution. (iv) step ii was repeated, but this time the heterodimerized PPARα is also pulled down. (v) The product is eluted from the beads and analyzed using SDS-PAGE analysis. **B.** SDS-PAGE analysis of the His-tag pulldown assay. PPARα is pulled down by full-length ERRα but not by the ERRα-LBD or the negative control His-NanoLuc.

When a protein physically interacts with ERRα, both proteins are pulled down when a magnetic field is applied (Figure 6A).

To determine if ERRα and PPARα LBD physically interact, the magnetic beads and PPARα LBD were incubated with either full-length His-ERRα or His-ERRα LBD. SDS-PAGE analysis was performed on the elution fractions to determine the sample composition (Figure 6A-B). Using full-length His-ERRα, two bands with similar intensity are observed around 30 and 50 kDa, corresponding to the weights of PPARα and full-length ERRα, respectively (Figure 6B). In contrast, only a faint PPARα-band was observed when pulled down with the ERRα LBD (Figure 6B). For His-NanoLuc, which was used as a negative control, only a single band was observed. The significant difference in the PPARα band intensity between the LBD and the full-length protein confirms that more than the LBD of ERRα is required to interact with PPARα. Similar to the GST-pulldown assay performed by Desmet *et al.*, no ligands were required for the interaction between both proteins.

Conclusion

ERRs and PPARs play an essential role in the tight regulation of oxidative metabolism in humans. Sofie Desmet and coworkers demonstrated that aside from overlapping genes, these NRs exhibit an even more direct interaction through their capacity to heterodimerize in a cellular environment. Using a tandem purification approach and a NanoBiT complementation assay, we showed that the purified, bacterially expressed LBDs of ERRα and PPARα displayed no interaction. Moreover, the FP assay showed that, in contrast to what the ERRα-PPARα heterodimer model (Figure 1) would predict, the ERRα-H12 peptide by itself was still not able to interact with the coactivator binding site of PPARα both in the presence and absence of GW7647. Finally, the *in vitro* His-tag pulldown assay revealed that actually full-length ERRα was required in order to dimerize with the PPARα LBD. Because the pulldown assay was performed using the purified proteins, this shows that the interaction between full-length ERRα and the PPARα LBD is indeed direct.

Experimental section

Strep-PPARα LBD expression and purification. A plasmid encoding the Strep-PPARα LBD was ordered from GenScript. A sequence encoding for the human PPARα LBD (residue 200-468) with an N-terminal Strep-tag®II was cloned into a pET15b vector using NcoI and XhoI restriction sites. E. Coli

BL21 (DE3) competent cells were transformed with the plasmid using heat-shock. A single colony was used to start a culture of 25 ml LB medium supplied with 100 µg/ml ampicillin, which was incubated overnight at 37°C. The starter cultures were transferred to 2 L of TB medium supplied with 0.05% antifoam SE-15 (Sigma Aldrich) and 100 µg/ml ampicillin. Protein expression was induced using 0.5 M IPTG when an OD600 of 0.8 was reached. Expression continued overnight at 15°C and 150 rpm. The cell pellet was collected by centrifugation at 10.000 RCF for 10 minutes at 4°C and resuspended in lysis buffer (50 mM Tris (pH=7.8), 300 mM NaCl, 10% glycerol, 25 U/ml Benzonase® Nuclease (Millipore) and one cOmplete™ Protease Inhibitor Cocktail tablet (Roche) per 25 ml cell suspension). Cells were lysed using an Emulsiflex-C3 homogenizer (Avestin) and the lysate was centrifuged at 40.000 RCF for 40 minutes at 4°C. A 5 ml Strep-Tactin®XT Superflow® high capacity cartridge was equilibrated with buffer B (50 mM Tris (pH=7.8), 300 mM NaCl and 10% glycerol). The cleared solution was loaded onto the column, which was subsequently washed with 10 CVs of buffer B. The purified protein was eluted using 5 CVs of buffer B supplied with 50 mM EDTA. The sample was dialyzed overnight to buffer C (20 mM Tris (pH=7.8), 150 mM NaCl, 5 mM DTT and 10% glycerol). The dialyzed solution was loaded on a Superdex 75 pg 16/60 size-exclusion column (GE Life Sciences) using buffer C as a running buffer. The elution fractions were analyzed using high-resolution mass spectrometry (Xevo G2 Quadrupole Time of Flight) and SDS-PAGE. Fractions containing the correct mass were combined, concentrated and stored at -80 °C.

His-ERRα LBD expression and purification. A plasmid designed to encode for the His-ERRα LBD was ordered from GenScript. The construct was cloned into a pET15b vector using the NdeI and XhoI restriction sites. The steps from transformation to cell lysis were performed similarly to Strep-PPARα with the addition of 20 mM imidazole in the lysis buffer. The lysed sample was loaded on a pre-equilibrated 5 ml Ni-NTA Superflow cartridge (QIAGEN). The column was washed with 10 CVs of buffer A (50 mM Tris (pH=7.8), 300 mM NaCl, 20 mM imidazole and 10% glycerol) and 10 CVs of buffer A with 45 mM imidazole. His-ERRα was eluted using 8 CVs of buffer A supplied with 200 mM imidazole. This fraction was dialyzed overnight to buffer B (20 mM Tris (pH=7.8), 150 mM NaCl, 5mM DTT and 10% glycerol) supplied with 1.2 U/mg restriction grade thrombin. Size-exclusion chromatography was used to obtain the purified cleaved protein. The fractions were combined, concentrated and stored as aliquots at -80 °C.

FL-ERRα expression and purification. A plasmid encoding FL-ERRα was ordered from GenScript. The full-length human ERRα (residue 1-423) gene with NCoI and NotI restriction sites was cloned into a pET28b(+) vector to include a C-terminal His-tag. Transformation of E. Coli BL21 (DE3) competent cells with the plasmid was performed with heat-shock. A single colony was picked and transferred to 25 ml LB medium supplied with 50 µg/ml kanamycin. This culture was incubated overnight in a shaking incubator at 37°C. The small cultures were transferred to 2 L Terrific Broth (TB) medium supplied with 0.05% antifoam SE-15 (Sigma Aldrich) and 50 µg/ml kanamycin. Using

0.5 mM IPTG, protein expression was induced when an OD600 of 0.8 was reached. Protein expression proceeded overnight at 18°C at 150 rpm. After 15 hours, the cell suspension was centrifuged at 10.000 RCF for 10 minutes at 4°C. The resulting cell pellet was resuspended in lysis buffer (20 mM Tris (pH=7.9), 500 mM NaCl, 10 mM imidazole, 25 U/ml Benzonase® Nuclease (Millipore) and one cOmplete™ Protease Inhibitor Cocktail tablet (Roche) per 25 ml cell suspension). An Emulsiflex-C3 homogenizer (Avestin) was used to lyse the cells and the lysate was cleared using centrifugation at 40.000 RCF for 40 minutes at 4°C. The supernatant was loaded on a 1 ml Ni-NTA Superflow cartridge (QIAGEN). The column was washed with 10 column volumes (CVs) of buffer A (20 mM Tris (pH=7.9), 500 mM NaCl and 10 mM imidazole) and 10 CVs of buffer A supplied with 45 mM imidazole. The purified protein was eluted using 8 CVs of buffer A with 200 mM imidazole. This fraction was then dialyzed overnight to a buffer containing 50 mM Tris (pH=7.9), 100 mM NaCl, 50 µM EDTA and 20% glycerol. Subsequently, the solution was concentrated using an Amicon® Ultra centrifugal filter with a 10 kDa cutoff (Millipore). The product was aliquoted, flash-frozen and stored at -80°C. The purity of the product was assessed using SDS-PAGE analysis.

In vitro Ni-NTA pulldown assay. To remove traces of EDTA and to ensure proper folding of FL-ERRα, the protein samples of FL-ERRα and the PPARα LBD were both buffer-exchanged to buffer D (20 mM Tris (pH=8.0), 300 mM NaCl, 15 mM imidazole and 100 µM ZnCl2) using PD SpinTrap G-25 columns (GE Healthcare) following the manufacturer's protocol. In the pulldown assay, His-NanoLuc will be used as a negative control. Ni-NTA magnetic agarose beads (QIAGEN) were added to His-tagged FL-ERRα and His-NanoLuc. The samples incubated for 1 hour on a tube rotator at 4°C. The tubes were placed on a DynaMag-2 magnetic separator (Thermo Fisher) for 1 min to remove the solution. The beads were washed with an excess of buffer D before placing it back on the magnetic separator and extracting the solution. Next, PPARα solution was added to the magnetic beads. The solution was incubated for another hour on a tube rotator at 4°C. The solution was removed using the magnetic separator and the wash step was repeated with buffer D. Finally, buffer D supplied with 200 mM imidazole was used to elute the product from the beads. SDS-PAGE was used to analyze sample composition.

Peptide synthesis and purification. A FITC-labeled PGC1α coactivator peptide (FITC-βA-EAEEPSLLKKLLLAPANTQ; residue 137-155) and H12 of ERRα (FITC-βA-PMHKLFLEMLEAMMD; residue 409-423) were synthesized using Fmoc SPPS using an automated multiple peptide synthesizer (Intavis MultiPep RSi). The peptides were synthesized using Rink amide AM resin (Novabiochem; 0.59 mmol/g). Deprotection of the residues was performed twice per cycle with 20% piperidine in DMF. This step was followed by two coupling steps (HBTU was used as the activator and DIPEA as the base). After coupling, the unreacted N-termini were acetylated (1:1:3 Ac2O/pyridine/DMF). The peptides were manually labeled with FITC (Sigma-Aldrich) using standard SPPS conditions. The peptide was cleaved from the resin using TFA/TIS/water (95:2.5:2.5) and precipitated in diethyl ether

twice. The peptide was dissolved in 20% H2O in ACN + 0.1% TFA and purified using a mass directed auto purification system (preparative reversed-phase HPLC). After purification, the peptides were lyophilized and stored at -30°C.

NanoBIT assay. SmBiT-PPARα was titrated to a constant concentration of LgBiT-ERRα (final concentration of 1, 10 and 100 nM) in 25 mM Tris (pH=7.8), 200 mM NaCl, 1 mM TCEP and 0.1% BSA. Substrate (1000x diluted) was added to the protein solution and transferred to a white Thermo Fisher Nunc 384-well plate. The plate incubated at room temperature for 5 minutes and just before measurement 10 µM GW7647 or DMSO was added to the wells. The emission was measured at 460 nm on a Tecan Spark plate reader directly after. After 10 minutes, the luminescent signal stabilized and the intensity difference with the DMSO control was determined ($I_{ligand} - I_{DMSO}$). The analysis was performed using GraphPad Prism 8.

FL-ERRα fluorescence polarization assay. A dilution series of XCT790 (100 µM – 48 pM) was made to a constant concentration of FL-ERRα (1 µM) and fluorescein-labeled PGC-1α cofactor peptide (residue 137-155; 0.1 µM) in a 384-well low volume black round bottom plate (Corning®). The buffer contained 25 mM Tris (pH=7.8), 200 mM NaCl, 5 mM DTT and 0.1% (w/v) bovine serum albumin. Plates were incubated for 30 minutes at 4°C before the fluorescence polarization was measured with a Tecan Infinite F500 plate reader using an excitation and emission wavelength of 485 nm and 535 nm, respectively. The experiment was performed in duplicate and the data were analyzed using GraphPad Prism 8.

Fluorescence polarization assay ERRα-H12 and PPARα. GW7647 was serially diluted (100 µM – 48 pM) to a constant concentration of PPARα (1 µM) and either FITC-labeled ERRα-H12 peptide (0.1 µM) or FITC-labeled PGC-1α peptide (0.1 µM) in a 384-well low volume black round bottom plate (Corning®). The DMSO concentration was kept constant at 1%. The buffer contained 25 mM Tris (pH=7.8), 200 mM NaCl, 5 mM DTT and 0.1% (w/v) bovine serum albumin. Plates were incubated for 30 minutes at 4°C before the fluorescence polarization was measured with a Tecan Infinite F500 plate reader using an excitation and emission wavelength of 485 nm and 535 nm, respectively. Duplicate measurements were performed, and the data were analyzed using GraphPad Prism 8.

Protein constructs

His-ERRα (pET15b)

MGSSHHHHHHSSGLVPRGSHMAAPVNALVSHLLVVEPEKLYAMPDPAGPDGHLPAVATLCDLFDREIV
VTISWAKSIPGFSSLSLSDQMSVLQSVWMEVLVLGVAQRSLPLQDELAFAEDLVLDEEGARAAGLGEL
GAALLQLVRRLQALRLEREEYVLLKALALANSDSVHIEDAEAVEQLREALHEALLEYEAGRAGPGGGA
ERRRAGRLLLTLPLLRQTAGKVLAHFYGVKLEGKVPMHKLFLEMLEAMMD

FL-ERRα-His (pET28a)

MGSSQVVGIEPLYIKAEPASPDSPKGSSETETEPPVALAPGPAPTRCLPGHKEEEDGEGAGPGEQGGG
KLVLSSLPKRLCLVCGDVASGYHYGVASCEACKAFFKRTIQGSIEYSCPASNECEITKRRRKACQACR
FTKCLRVGMLKEGVRLDRVRGGRQKYKRRPEVDPLPFPGPFPAGPLAVAGGPRKTAAPVNALVSHLLV
VEPEKLYAMPDPAGPDGHLPAVATLCDLFDREIVVTISWAKSIPGFSSLSLSDQMSVLQSVWMEVLVL
GVAQRSLPLQDELAFAEDLVLDEEGARAAGLGELGAALLQLVRRLQALRLEREEYVLLKALALANSDS
VHIEDAEAVEQLREALHEALLEYEAGRAGPGGGAERRRAGRLLLTLPLLRQTAGKVLAHFYGVKLEGK
VPMHKLFLEMLEAMMDAAALEHHHHHH

Strep-PPARα (pET15b)

MGWSHPQFEKSSGLVPRGSHMTADLKSLAKRIYEAYLKNFNMNKVKARVILSGKASNNPPFVIHDMET
LCMAEKTLVAKLVANGIQNKEAEVRIFHCCQCTSVETVTELTEFAKAIPGFANLDLNDQVTLLKYGVY
EAIFAMLSSVMNKDGMLVAYGNGFITREFLKSLRKPFCDIMEPKFDFAMKFNALELDDSDISLFVAAI
ICCGDRPGLLNVGHIEKMQEGIVHVLRLHLQSNHPDDIFLFPKLLQKMADLRQLVTEHAQLVQIIKKT
ESDAALHPLLQEIYRDMY
ABCD = Purification tag

Supporting Information

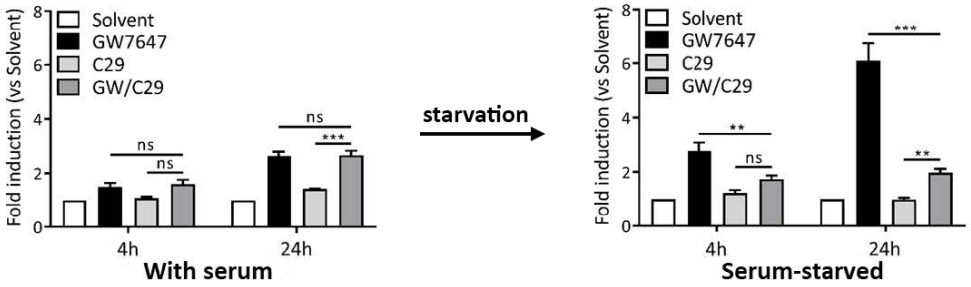

Figure S1 | Influence GW7647 and C29 on ERRα-PPARα heterodimerization. A. L929sA cells with a PDK4 promoter fused to the luciferase reporter gene under serum or serum-starved conditions. After 4 hours, the cells were supplied with the 0.5 µM GW7647 (GW) and/or 5 µM C29 for 4 or 24h. Promoter activities are expressed as relative induction factor versus solvent. Figure adapted from Desmet *et al.* (2020).

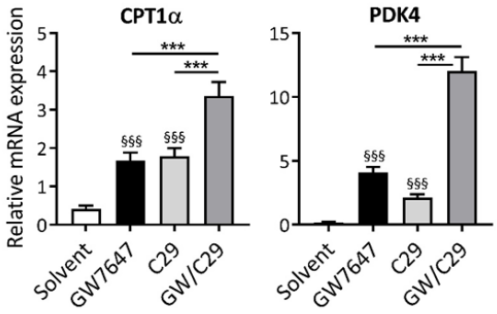

Figure S2 | Influence of ERRα on the transcriptional activity of PPARα. Serum-starved HepG2 cells were stimulated with 0.5 µM GW7647 and/or 5 µM C29 for 24h. RNA expression values were normalized to the reference genes GAPDH and TBP. The luciferase activities were analyzed with a Hierarchical Generalized Linear Mixed Model (HGLMM) fitting. Figure adapted from Desmet *et al.* (2020).

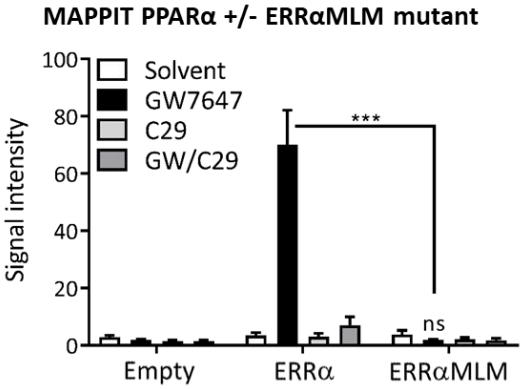

Figure S3 | MAPPIT with PPARα as bait and ERRα or ERRαMLM mutant as prey. Serum-starved cells were stimulated with leptin and 0.5 µM GW7647 and/or 5 µM C29 for 24 hours or were left untreated. Luciferase measurements were normalized by untreated values (Mean + SEM, n=3). Figure adapted from Desmet *et al.* (2020).

Confidentiality Statement

All scientific information, results and ideas described in this chapter are shared property between TU/e and VIB-UGent and are not allowed to be disclosed to any third party without the prior consent of the principal investigators Prof. Dr. Ir. L. Brunsveld and Prof. Dr. K. De Bosscher.

Acknowledgements

Sofie Desmet and Karolien De Bosscher from Ghent University are gratefully acknowledged for the fruitful collaboration and their valuable input on all aspects of this chapter.

References

1. Chawta, A., Repa, J. J., Evans, R. M. & Mangelsdorf, D. J. Nuclear receptors and lipid physiology: Opening the x-files. *Science* vol. 294 1866–1870 (2001).
2. Francis, G. A., Fayard, E., Picard, F. & Auwerx, J. Nuclear Receptors and the Control of Metabolism. *Annual Review of Physiology* vol. 65 261–311 (2003).
3. Evans, R. M., Barish, G. D. & Wang, Y. X. PPARs and the complex journey to obesity. *Nature Medicine* vol. 10 355–361 (2004).
4. Poulsen, L. la C., Siersbæk, M. & Mandrup, S. PPARs: Fatty acid sensors controlling metabolism. *Seminars in Cell and Developmental Biology* vol. 23 631–639 (2012).
5. Bougarne, N. *et al.* Molecular actions of PPARα in lipid metabolism and inflammation. *Endocrine Reviews* vol. 39 760–802 (2018).
6. Tontonoz, P. & Spiegelman, B. M. Fat and beyond: The diverse biology of PPARγ. *Annual Review of Biochemistry* vol. 77 289–312 (2008).
7. Patch, R. J. *et al.* Indazole-based ligands for estrogen-related receptor α as potential anti-diabetic agents. *Eur. J. Med. Chem.* **138**, 830–853 (2017).
8. Fan, W. & Evans, R. PPARs and ERRs: Molecular mediators of mitochondrial metabolism. *Current Opinion in Cell Biology* vol. 33 49–54 (2015).
9. Xia, H., Dufour, C. R. & Giguère, V. ERRα as a bridge between transcription and function: Role in liver metabolism and disease. *Front. Endocrinol. (Lausanne).* **10**, 206 (2019).
10. Patch, R. J. *et al.* Identification of diaryl ether-based ligands for estrogen-related receptor α as potential antidiabetic agents. *J. Med. Chem.* **54**, 788–808 (2011).
11. Wu, P., Peters, J. M. & Harris, R. A. Adaptive increase in pyruvate dehydrogenase kinase 4 during starvation is mediated by peroxisome proliferator-activated receptor α. *Biochem. Biophys. Res. Commun.* **287**, 391–396 (2001).
12. Zhang, Y. *et al.* Estrogen-related receptors stimulate pyruvate dehydrogenase kinase isoform 4 gene expression. *J. Biol. Chem.* **281**, 39897–39906 (2006).
13. Lievens, S. *et al.* Array MAPPIT: High-throughput interactome analysis in mammalian cells. *J. Proteome Res.* **8**, 877–886 (2009).
14. Lievens, S., Peelman, F., De Bosscher, K., Lemmens, I. & Tavernier, J. MAPPIT: A protein interaction toolbox built on insights in cytokine receptor signaling. *Cytokine and Growth Factor Reviews* vol. 22 321–329 (2011).
15. Brown, P. J. *et al.* Identification of a subtype selective human PPARα agonist through parallel-array synthesis. *Bioorganic Med. Chem. Lett.* **11**, 1225–1227 (2001).
16. Busch, B. B. *et al.* Identification of a selective inverse agonist for the orphan nuclear receptor estrogen-related receptor α. *J. Med. Chem.* **47**, 5593–5596 (2004).
17. Kallen, J. *et al.* Crystal structure of human estrogen-related receptor α in complex with a synthetic inverse agonist reveals its novel molecular mechanism. *J. Biol. Chem.* **282**, 23231–23239 (2007).
18. Nolte, R. T. *et al.* Ligand binding and co-activator assembly of the peroxisome proliferator-activated receptor-gamma. *Nature* **395**, 137–43 (1998).
19. Zhang, J. *et al.* DNA binding alters coactivator interaction surfaces of the intact VDR-RXR complex. *Nat. Struct. Mol. Biol.* **18**, 556–563 (2011).

20. Tanenbaum, D. M., Wang, Y., Williams, S. P. & Sigler, P. B. Crystallographic comparison of the estrogen and progesterone receptor's ligand binding domains. *Proc. Natl. Acad. Sci. U. S. A.* **95**, 5998–6003 (1998).
21. Westin, S. *et al.* Interactions controlling the assembly of nuclear-receptor heterodimers and co-activators. *Nature* **395**, 199–202 (1998).
22. Zhang, J., Hu, X. & Lazar, M. A. A Novel Role for Helix 12 of Retinoid X Receptor in Regulating Repression. *Mol. Cell. Biol.* **19**, 6448–6457 (1999).
23. Dawson, M. I. & Xia, Z. The retinoid X receptors and their ligands. *Biochimica et Biophysica Acta - Molecular and Cell Biology of Lipids* vol. 1821 21–56 (2012).
24. Esch, A. M., Thompson, N. E., Lamberski, J. A., Mertz, J. E. & Burgess, R. R. Production and characterization of monoclonal antibodies to estrogen-related receptor alpha (ERRα) and use in immunoaffinity chromatography. *Protein Expr. Purif.* **84**, 47–58 (2012).
25. Roehrborn, C. G., Zoppi, S., Gruber, J. A., Wilson, C. M. & McPhaul, M. J. Expression and characterization of full-length and partial human androgen receptor fusion proteins. Implications for the production and applications of soluble steroid receptors in Escherichia coli. *Mol. Cell. Endocrinol.* **84**, 1–14 (1992).
26. Liao, M. & Wilson, E. M. Production and purification of histidine-tagged dihydrotestosterone-bound full-length human androgen receptor. *Methods in molecular biology (Clifton, N.J.)* vol. 176 67–79 (2001).
27. Zhu, Z., Bulgakov, O. V., Scott, S. S. & Dalton, J. T. Recombinant expression and purification of human androgen receptor in a baculovirus system. *Biochem. Biophys. Res. Commun.* **284**, 828–835 (2001).

CHAPTER 4

Elucidation of an Allosteric Mode-of-Action of RORγt Inverse Agonists

Abstract

Allosteric targeting of nuclear receptors is in strong demand, but examples are limited and structural information is scarce. The RAR-related orphan receptor gamma t (RORγt) is an essential transcriptional regulator for the differentiation of T helper 17 cells for which the first, and some of the most promising, examples of allosteric nuclear receptor modulation have been reported and structurally proven. Using a combination of biochemical and X-ray crystallography studies, the allosteric binding mode of the *in silico*-derived FM26 and Glenmark's compound 13 was elucidated. These potent ligands are chemically distinct from the earlier reported MRL-871 and are valuable additional examples of allosteric nuclear receptor modulators.

Part of this work is published as:

1. Meijer, F. A., Doveston, R. G., de Vries, R. M. J. M., et al. Ligand-Based Design of Allosteric Retinoic Acid Receptor-Related Orphan Receptor γt (RORγt) Inverse Agonists. J. Med. Chem. 63, 241–259 (2020).
2. de Vries, R. M. J. M., Doveston, R. G., Meijer, F. A. & Brunsveld, L. Elucidation of an Allosteric Mode of Action for a Thienopyrazole RORγt Inverse Agonist. ChemMedChem 15, 561–565 (2020).

Introduction

The retinoic acid-related orphan receptor gamma t (RORγt) has garnered much attention as an intervention point to treat autoimmune diseases such as multiple sclerosis, psoriasis and inflammatory bowel disease. A significant characteristic of these diseases is the excessive production of the pro-inflammatory cytokine interleukin 17 (IL-17) by Th17 cells. RORγt plays a key role in Th17 cell differentiation. Disruption of the IL-17 signaling pathway using recently FDA-approved monoclonal antibodies has already been shown as an effective strategy for the treatment of psoriasis.[1–3] Therefore, inhibition of RORγt would be a highly promising alternative therapeutic strategy.[4–6] Numerous small molecules have been reported that effectively inhibit RORγt, which is transcriptionally active even in the absence of any endogenous agonist.[7–9] Typically, such inverse agonists bind to the orthosteric NR binding pocket; a pocket with contemporary challenges in achieving NR subtype selectivity and competition with endogenous ligands. Allosteric modulation of NR activity offers a promising novel concept for addressing such challenges and for novel modes of NR drug action in general.[10–12] However, examples of structurally characterized and sufficiently potent NR allosteric modulators are scarce. The discovery and development of such compounds is therefore urgently needed in order to steer their molecular design process and further our conceptual understanding of allosteric NR modulation.[11]

Recently, allosteric modulation of RORγt was shown to be a promising approach for drug development, featuring examples of allosteric ligands with high NR subtype selectivity and absence of competition with the endogenous ligands.[13–16] The first example to emerge was the indazole MRL-871, a potent inverse agonist. Originally disclosed by Merck Sharp and Dohme (MSD) in 2012, its allosteric mode-of-action was characterized three years later.[13,17] MRL-871 binds in an allosteric pocket of RORγt composed of helix 3, 4, 11 and 12 (Figure 1A). Glenmark Pharmaceuticals used the MRL-871 core as the basis for an in silico scaffold hopping screen in search of a novel but similarly potent compound class.[18] This led to the development of a family of thienopyrazole inverse agonists with nanomolar activity, which were disclosed in a 2015 patent, of which 'compound 13' was the most potent example (Figure 1B).[19] Although a comprehensive structure-activity relationship (SAR) study was conducted around the thienopyrazole scaffold, the binding mode to RORγt was not reported. MRL-871 and compound 13 differ mostly in their central heteroaromatic core (Figure 1B). Due to the

similarity between the two compounds, it is likely that the thienopyrazole series share the same allosteric binding mode as indazole MRL-871.

The structural characterization of new classes of allosteric RORγt inverse agonist is of great value in terms of better understanding SAR with respect to RORγt allosteric pocket. For this reason, a novel RORγt allosteric inverse agonist was designed using an *in silico*-guided 3D pharmacophore screening and optimization approach starting from the MRL-871 scaffold.[14] This computationally-driven approach allowed for efficient ligand design and optimization, resulting in the development of the trisubstituted isoxazole FM26, an inverse agonist with favorable pharmacokinetic properties (Figure 1B). FM26 significantly reduced IL-17a mRNA expression in murine lymphoblast cells by inhibiting RORγt.[14]

This chapter described, X-ray crystallography and biochemical assays used to confirm that the allosteric mode-of-action of FM26 and compound 13 is analogous to that of MRL-871. The design of the RORγt protein construct used for crystallography and the necessary purification optimization will be discussed in detail. The structural characterization of RORγt in complex with chemically diverse allosteric ligands will contribute to our growing conceptual understanding of allosteric modulation of NRs.

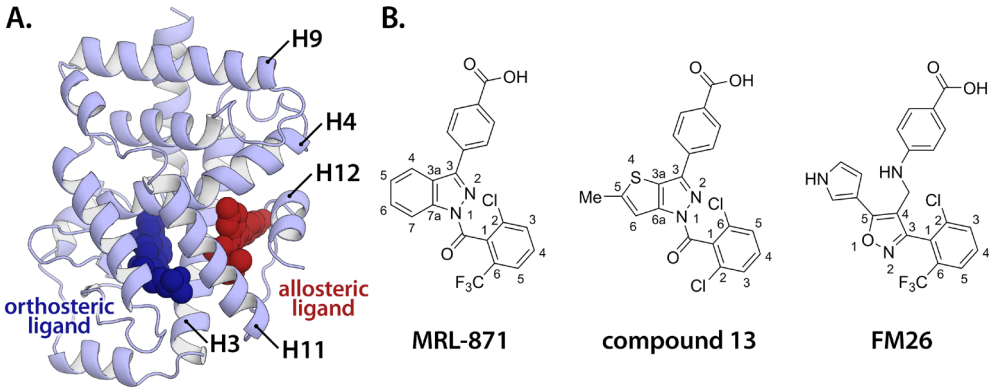

Figure 1 | Inhibition of RORγt using allosteric inverse agonists. A. Illustration of RORγt in complex with an orthosteric (dark blue; PDB: 3L0L) and an allosteric ligand (dark red; PDB: 6TLM). The allosteric ligand induces a conformation of helix 12 that prevents coactivator binding. **B.** The chemical structures of allosteric RORγt inverse agonists MRL-871, compound 13 and FM26. The numbers represent the standard IUPAC atom numbering.

Results and Discussion

Biochemical evaluation of allosteric ligand binding

A time-resolved FRET (TR-FRET) coactivator recruitment assay was used to evaluate the inhibitory activity of FM26 and compound 13. In the absence of ligand, RORγt is in the active conformation and interacts with coactivator peptides. Both FM26 (IC_{50} = 247.8 ± 17.7 nM) and compound 13 (IC_{50} = 425 ± 61 nM) inhibited coactivator binding with submicromolar potency (Figure 2A-B). However, in Glenmark's original patent disclosure, an IC_{50} value of <50 nM was reported using a similar assay format.[19] In agreement with previously reported values, MRL-871 was found to be ~50 times more potent (7.8 ± 0.5 nM).

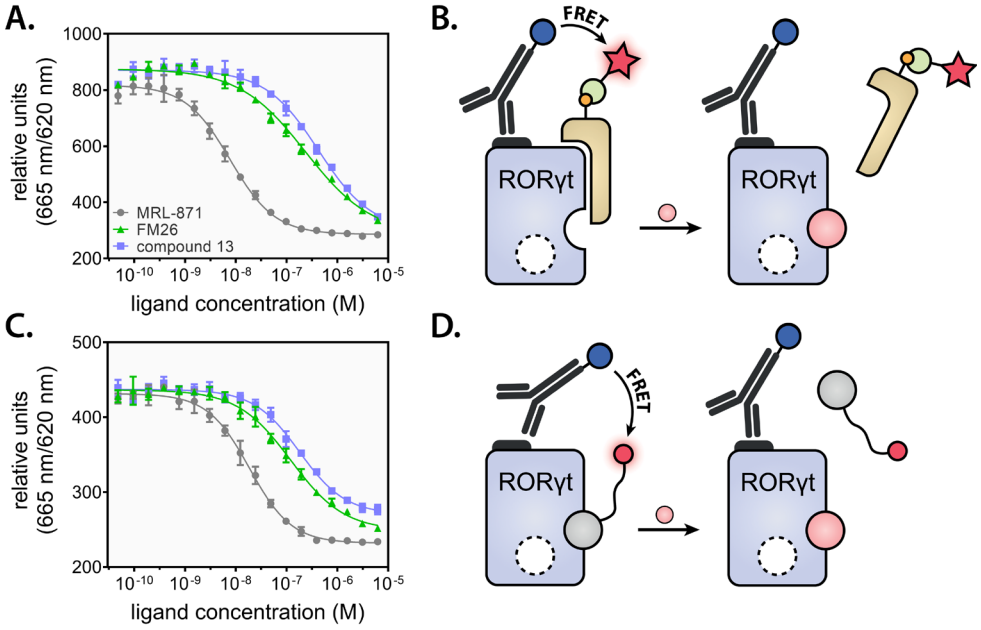

Figure 2 | Dose-response curves from TR-FRET assays. A. Coactivator recruitment assay titrating allosteric ligands MRL-871, FM26 and compound 13 to a fixed concentration of RORγt and labeled coactivator peptide. **B.** Schematic of the coactivator recruitment assay (**A**). RORγt interacts with the labeled coactivator peptide when no ligand is bound, leading to a high FRET signal. Upon binding an allosteric modulator (pink sphere), coactivator binding is inhibited, decreasing the FRET signal. **C.** MRL-871-probe displacement assay, titrating allosteric ligands to a fixed concentration of RORγt and AlexaFluor-labeled MRL-871. **D.** Schematic of the MRL-probe displacement assay (**C**). Upon increasing the allosteric ligand concentration, the AlexaFluor-labeled MRL-871 is displaced from the allosteric pocket, producing a lower FRET signal.

A ligand displacement assay was performed using a previously reported MRL-871-derived fluorescent probe known to bind the allosteric site of RORγt (Figure S1).[14] FM26 and compound 13 demonstrated to effectively displace the MRL-probe in a dose-dependent manner (Figure 2C-D). Thus, these results indicate that FM26 and compound 13 bind to the same allosteric pocket as MRL-871. However, probe displacement could also be caused by changes in protein conformation induced by ligand binding to another site on RORγt.

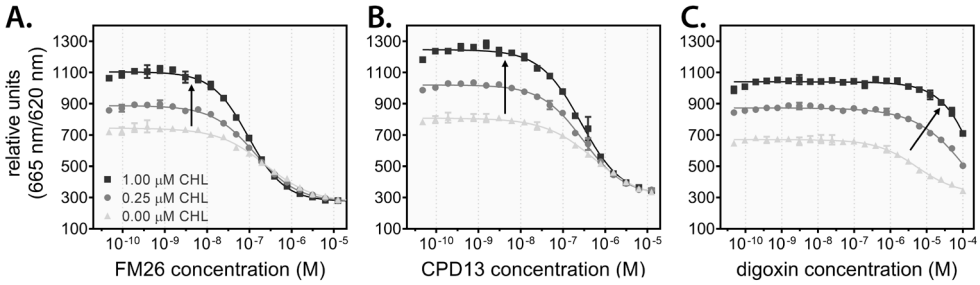

Figure 3 | Competitive TR-FRET coactivator recruitment assays in the presence of cholesterol. The inverse agonists were titrated to RORγt in the presence of fixed concentrations of cholesterol (CHL; 0, 0.25 and 1.0 μM). Dose-response curves of **A.** FM26, **B.** compound 13 (CPD13) and **C.** orthosteric inverse agonist digoxin.

A competition TR-FRET assay was performed as an orthogonal method to validate the binding to the allosteric pocket. Allosteric ligand titrations were performed in the presence of increasing concentrations of the well-characterized orthosteric agonist, cholesterol (Figure 3A-B).[20] Because of the presence of cholesterol, the upper asymptotic plateau increases as it stabilizes the active state of the receptor (Figure 3). The binding curves revealed that the presence of cholesterol does not lower the inhibitory potency of FM26 and compound 13, but instead slightly enhances it (94 ± 3 nM and IC_{50} = 269 ± 19 nM in the presence of 1.0 μM cholesterol, respectively; Table S2). In contrast, the orthosteric inverse agonist digoxin competes for the same binding site as cholesterol. As a result, higher concentrations of cholesterol reduce the affinity of digoxin for RORγt (Figure 3C and Table S2). The absence of competition between cholesterol and the proposed allosteric ligands suggests that the binding mode is independent of cholesterol and, therefore, likely binds to an allosteric pocket on RORγt.

Optimization of a RORγt protein construct for crystallography

To unambiguously confirm the binding mode of FM26 and compound 13 and to provide insights into the molecular details of the receptor-ligand interaction, the crystal structure of the binary complex is required. The crystal structure of the RORγt protein in complex with either orthosteric or allosteric ligands has been successfully solved in the past using the wildtype amino acid sequence. For most deposited structures, the C-terminus of the LBD is trimmed off, removing the flexible F-domain attached to helix 12, which can inhibit crystal formation.[20] Therefore, the wildtype construct (residues Ala265-Ser507) was used as a starting point was used in crystallization experiments.

RORγt was purified using a similar approach as the NRs described in Chapters 2 and 3. For the wildtype RORγt, a yield of 10-15 mg pure product was obtained per liter of cell culture, which was significantly lower than for the other NR LBDs. After Ni-NTA chromatography, reduced protein stability was observed. Particularly during the final concentration stage, small temperature fluctuations, and the associated pH-change of the buffer, resulted in severe protein aggregation.[21]

After protein purification, a significant impurity was detected, consisting of C-terminally truncated RORγt, terminating at either Val493 or Val494 (Figure 4). The truncation appears to be the result of proteolytic cleavage in the E. Coli cells, as it is already observed after Ni-affinity chromatography. Supplying the lysis buffer with high concentrations of protease inhibitors did not reduce the abundance of the cleavage product. Despite the impurity, crystallization screens were set up in the presence of the allosteric modulators using the commercial crystallization suites (PACT Premium, JCSG+, NR-LBD and $AmSO_4$). After one day, crystal growth was observed in multiple conditions

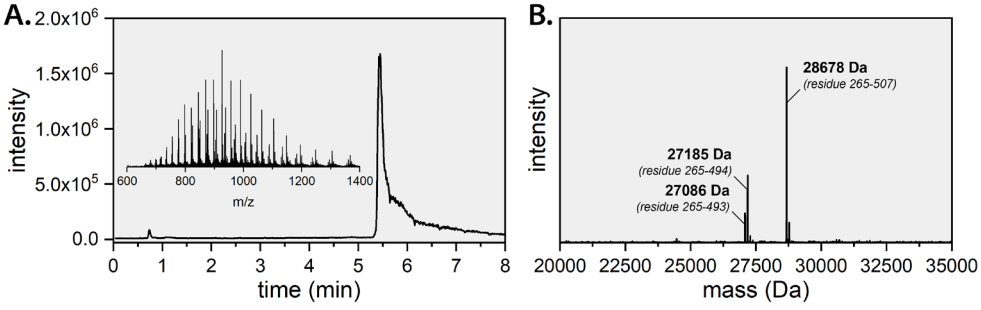

Figure 4 | Q-ToF LC/MS data of wildtype RORγt. A. Total ion count chromatogram and the mass range of the primary peak (5.35-6.05 min) reported as m/z (insert). **B.** Deconvoluted mass chromatogram showing the intact RORγt LBD and the C-terminal truncated product.

across the screens. In particular, the NR-LBD crystallization suite from Molecular Dimensions produced crystals in 31 of the 96 conditions. Crystals grew exclusively in an (elongated) hexagonal bipyramid shape and typically diffracted to a resolution of 2.3-2.8 Å (Figure S2A-B). The crystal structure shows clear electron density for the RORγt LBD up until Val493. After this residue, only weak and undefined electron density was observed. Moreover, no electron density was detected corresponding to the allosteric ligand, which is likely the result of the heterogeneity of the protein sample caused by the cleavage product.

The degree of proteolytic cleavage is, in part, dependent on the accessibility of the cleavage site.[22] Because the cleavage site is located in the loop between helix 11 and 12, the conformational stability of helix 12 plays a significant role in the accessibility of this site. Crystal structures derived from constructs with an elongated C-terminus regularly show additional electron density for Thr508 when RORγt is in the active conformation (Figure 5A).[20,23] This residue forms a salt-bridge with Gln484 and stabilizes the conformation of helix 12. This interaction could, therefore, be beneficial in preventing proteolytic cleavage. In addition, in the crystal structure of RORγt in complex with MRL-871, Cys455 is present at the protein's outer surface and close to the Cys455 of its symmetry mate. The distance between both thiols is 2.02 Å, and these cysteines probably form an intermolecular disulfide bridge (since the ideal S-S bond distance is 2.05 Å).[24]

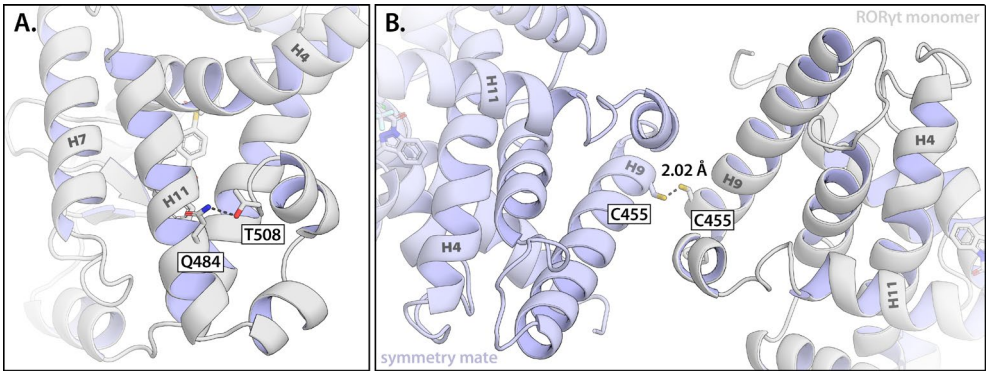

Figure 5 | RORγt-LBD construct optimization strategies for protein crystallography. A. The crystal structure of an extended construct (residue Pro263-Glu509) of the RORγt-LBD in the active conformation (PDB: 4NIE) shows that the C-terminal Thr508 interacts with Gln484 to stabilize the fold of helix 12. **B.** In the crystal structure of RORγt in complex with MRL-871 (PDB: 4YPQ), Cys455 is located at the interface of two symmetry mates. Cys455 is in close contact with the Cys455 of the symmetry mate and is likely to form a disulfide bond. Post-translational modifications on Cys455 are likely to abolish crystal packing.

Disulfide bonding or the oxidation of this cysteine can, therefore, hinder crystal growth. Cys455 is distant from both the orthosteric and allosteric LBPs, and mutating this residue is expected not to impact the protein function (Figure 5B).

A new DNA-construct was designed to encode for the RORγt-LBD incorporating the C455S mutation as well as an extended C-terminus (RORγtC455S; residues Ala265-Thr508). The protein was purified using the same method as the wildtype variant. The size-exclusion chromatography (SEC) chromatogram of the purified protein presented a single tailing peak (Figure 6A). This peak was collected in separate fractions and analyzed using SDS-PAGE, showing a single band for all the fractions (Figure 6B). However, Q-ToF LC/MS analysis revealed that this peak is composed of the intact LBD as well as the cleavage product (Figure 6C). The additional Thr508 did reduce the presence of the truncation

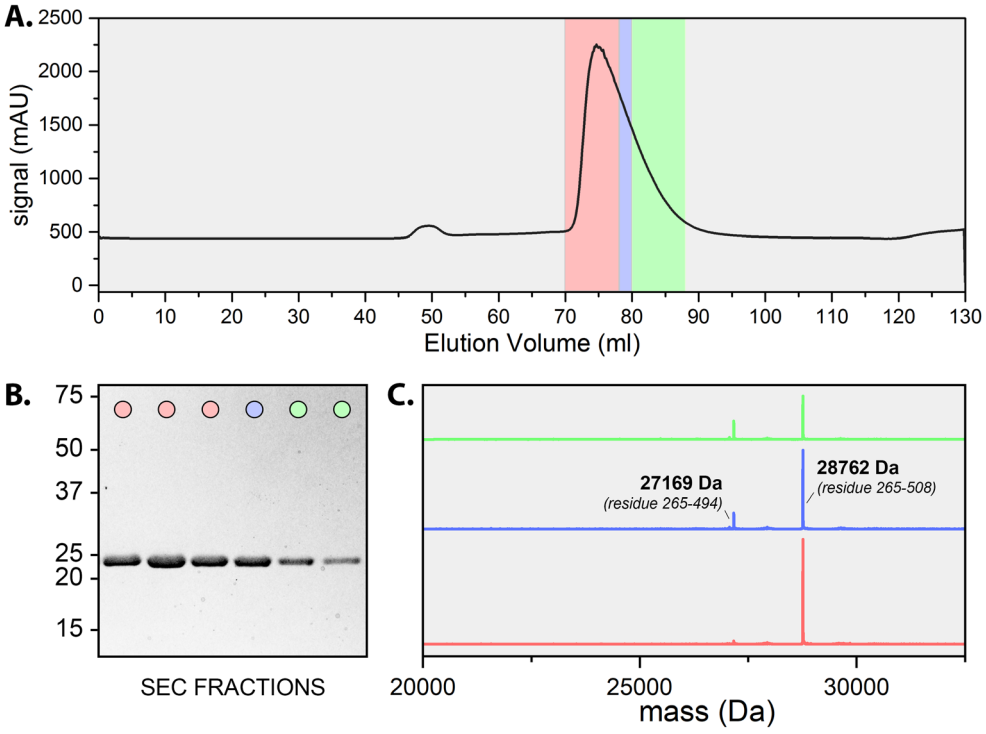

Figure 6 | Purification of the RORγtC455S LBD. A. Size-exclusion chromatography (SEC) chromatogram of RORγtC455S after Ni-affinity chromatography. The highlighted areas indicate the three separate fractions that were collected. **B.** SDS-PAGE analysis of the SEC fractions. The colored spheres match the fraction colors correspond with the highlighted areas in (**A**). The intact RORγtC455S LBD and the C-terminally truncated RORγtC455S show up as a single band. **C.** Deconvoluted mass of the three different fractions determined by Q-ToF LC/MS.

product but did not prevent proteolytic cleavage. Pure RORγtC455S could be isolated by selectively collecting the first part of the peak (Figure 6A, red section). Crystallization with the purified protein in the presence of an allosteric inverse agonist leads to crystals with a spherical shape with a rough surface (Figure S2C-D). Protein-related diffraction patterns were observed for these crystals but did not diffract beyond 4.8 Å.

Finally, a DNA-construct was designed for the RORγt LBD using the original sequence length (residue Ala265-Ser507) and a C455H mutation. The SEC-chromatogram of the purified protein showed an intense peak with a smaller shoulder peak (Figure 7), indicating that two or more proteins remain after Ni^{2+}-affinity chromatography.

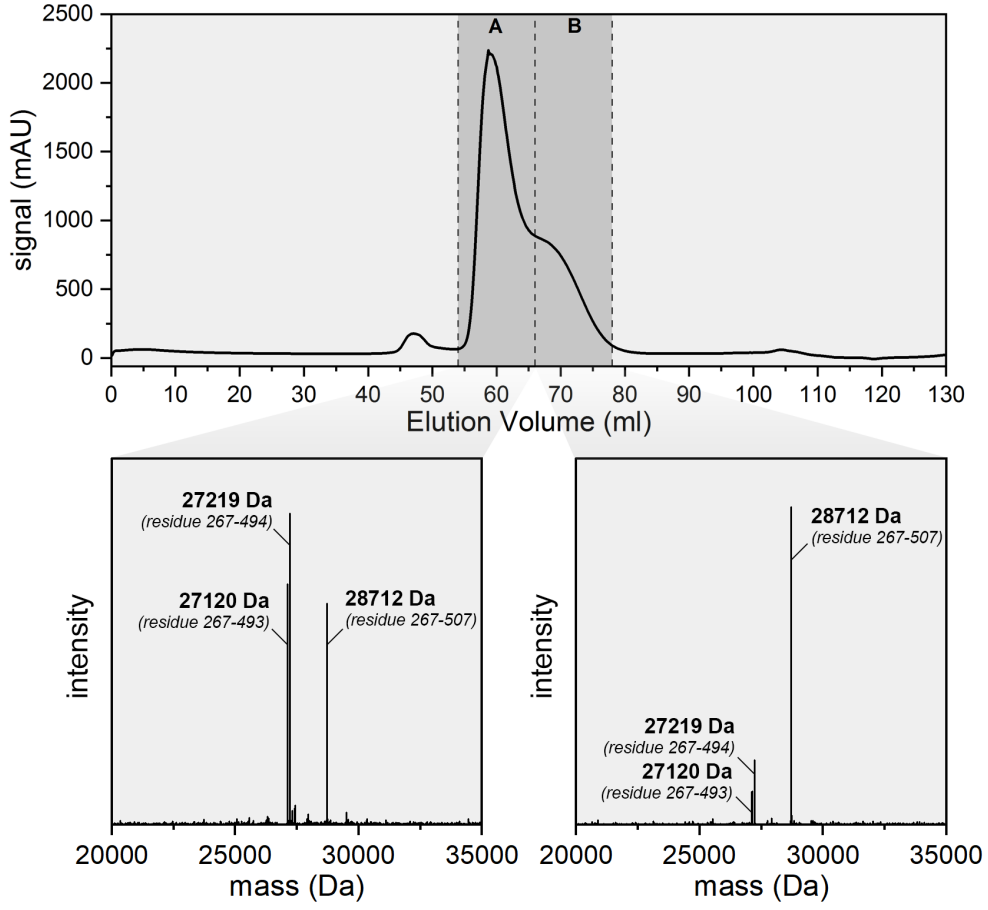

Figure 7 | Purification of the RORγtC455S LBD. SEC-chromatogram of RORγtC455H. The collected fractions A and B are highlighted. The graphs below show the deconvoluted mass spectrum of fractions A and B determined by Q-ToF LC/MS.

Interestingly, RORγtC455H starts to elute from the column after 55 ml (Figure 7A) of buffer compared to 70 ml for RORγtC455S (Figure 6A). The primary (fraction A) and the shoulder peak (fraction B) were collected separately and analyzed using Q-TOF LC/MS. Fraction A primarily contained the C-terminally truncated protein, while fraction B contained the intact RORγtC455H (Figure 7). Because the smaller, truncated protein has a shorter retention time, it can likely form oligomeric assemblies while the intact protein is exclusively monomeric. The first fractions from peak B were discarded to remove the impurity and the rest of the fractions were combined to be used for crystallography.

Missing electron density of RORγt-helix 12 in literature

RORγt is often crystallized in the presence of an inverse agonist because of its pharmacological relevance.[7,8] In a large number of these structures, electron density is observed up to and including helix 11.[25–28] The common argument is that this is caused by the C-terminus being flexible or lacking regular structure in the presence of an inverse agonist. However, there are numerous examples of crystal structures of NRs bound to inverse agonists or antagonists that do show helix 12, often stabilized by a symmetry mate.[29–31] For RORγt, the wildtype RORγt and the RORγtC455S mutant are generally used to obtain crystal structures applying a comparable protein purification protocol and using SDS-PAGE to assess the purity of the protein. However, SDS-PAGE showed that the intact and truncated products appear as a single band due to the subtle mass difference (Figure 6B). To determine the presence of both products, high-resolution LC/MS is required. Therefore, it is likely that the mentioned studies also experienced C-terminal truncation of RORγt, leading to the H12–truncated crystal structures, but that it was overlooked. In this chapter, the C-terminally truncated RORγt was also crystallized, and the structure could be successfully determined. Therefore, the absence of electron density in the crystal structures could be explained by the presence of the C-terminally truncated RORγt.

Crystal structure of RORγt in complex with FM26 and compound 13

RORγtC455H was co-crystallized with FM26 and compound 13, and crystals grew as hexagonal bipyramids into a $P6_122$ space group overnight using sitting-drop vapor diffusion (Figure S2E-H). The crystals diffracted to a resolution of 1.61 Å and 2.32 Å for FM26 and compound 13, respectively. The data collection and refinement statistics are provided in Table S1. The crystal structures show the complete LBD of RORγt and reveal that FM26 and compound 13 indeed bind in the allosteric pocket and that the orthosteric

pocket is devoid of ligand (Figure 8A&D). Of specific and notable interest is the folding of helix 12, which is in a conformation precluding coactivator binding. The carboxylic acid moiety of both ligands interacts with Gln329 and two backbone amides of Ala497 and Phe498 located in the loop between helix 11 and 12 of RORγt (Figure 8B&E). The pyrrole of FM26 is within hydrogen bonding distance of the backbone carbonyls of Leu353 and Lys354, which can explain the higher affinity of FM26 for RORγt than compound 13. The binding mode of both allosteric ligands to RORγt is comparable to that of MRL-871 (Figure 8C&F). A first notable difference in the binding to RORγt of both ligands lies in the increased bulk of both ligands towards helix 4 of RORγt. The methyl substituent on the thienopyrazole core of compound 13 and the pyrrole of FM26 induce a shift of helix 4,

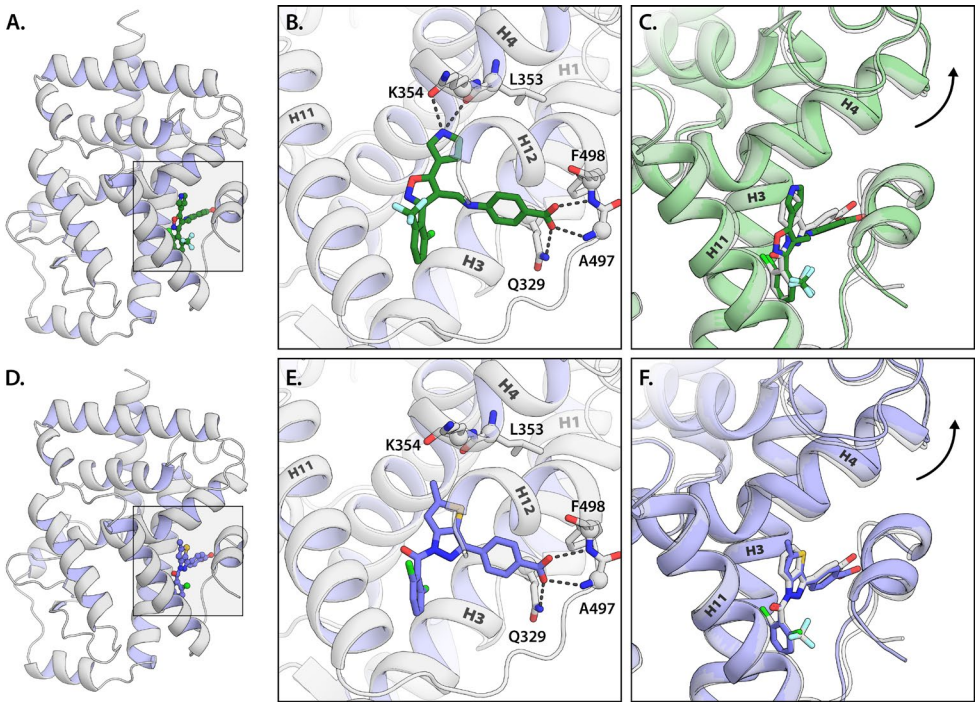

Figure 8 | Crystal structures of RORγt in complex with an allosteric ligand. A. The tertiary structure of RORγt in complex with FM26 (green sticks). **B.** Close-up of the allosteric ligand-binding pocket of RORγt. The polar interactions between RORγt and FM26 are shown as a grey dotted line. **C.** Superimposed structures of 6SAL (solid green) and RORγt in complex with MRL-871 (semi-transparent white; PDB: 5C4O). FM26 and compound 13 introduce more bulk towards helix 4 compared to MRL-871, causing helix 4 to move towards helix 9 (indicated by the arrow). **D.** The tertiary structure of RORγt in complex with compound 13 (blue sticks). **E.** Interaction network of compound 13 with RORγt. **F.** Superimposed structures of 6TLM (solid blue) and 5C4O (semi-transparent white).

correlated with a displacement of helix 9 (Figure 8C&F and Figure S3). A second difference can be observed in the loop between helix 11 and 12. Compared to MRL-871, the benzoic acid moiety of both ligands is orientated differently in the pocket, which is connected to a change in the overall fold of this loop.

Comparison of the IC_{50} values of MRL-871, FM26 and compound 13 would suggest that steric bulk towards helix 4 does not favor the affinity of the allosteric modulator for RORγt (Figure 2A). MSD's patent application showed that bulky substitutions on the 4 and 5 position of the indazole moiety also resulted in a reduced affinity for the receptor.[32] Glenmark did disclose the less bulky hydrogen-substituted thienopyrazole, but the biochemical activity of this analog was not evaluated. However, various compounds were evaluated incorporating bulkier amide substituents replacing the methyl group.[19] Such compounds generally showed a lower or no binding affinity for RORγt.

Conclusion

In summary, the optimization process of the RORγt construct for crystallography was described. This involved reducing the proteolytic cleavage of the C-terminus of the protein as well as a mutation of a surface-exposed cysteine to prevent post-translational modifications and intramolecular disulfide bonding. Although the C-terminal truncation of the protein could not be prevented, SEC could be used to effectively separate both proteins. Moreover, the C455H mutation did significantly improve crystal quality.

X-ray crystallography and biochemical studies revealed that FM26 and Glenmark's compound 13 bind to an allosteric pocket of RORγt. The binding mode of both ligands is similar to MRL-871, with small but notable differences. The structural data imply that the lower affinity of these ligands for RORγt relates to additional bulk to RORγt helix 4, which leads to changes in the overall protein fold. Such changes are likely to affect the dynamics of the protein and stability of the specific fold. The new structural data expand the collection of crystallized ligands binding to the allosteric binding pocket on NRs, and specifically on RORγt. The resulting new insights will aid in the understanding of reported compounds classes, potentially also addressing the same allosteric RORγt pocket and in the development of new compound classes with more diverse chemotypes or optimized pharmacodynamic profiles.

Experimental section

RORγt-LBD expression and purification (used for TR-FRET assays). A pET15b expression vector encoding the human RORγt LBD (residues 265-518) with an N-terminal His6-tag was transformed by heat shock into BL21(DE3) E. coli cells. Single colonies were used to inoculate pre-cultures of 8 ml LB-media containing 100 µg/ml ampicillin. After overnight incubation at 37 ˚C, each pre-culture was transferred to 1 liter TB media supplemented with ampicillin (100 µg/ml) and incubated at 37 ˚C until an OD600 nm = 1.0 was reached. Protein expression was then induced with 0.5 mM isopropyl-β-d-thiogalactoside (IPTG), and cultures were incubated for 16 h at 18˚C. The cells were collected by centrifugation and suspended in lysis buffer (300 mM NaCl, 20 mM Tris (pH=8.0), 20 mM imidazole, 1 mM TCEP, 10% v/v glycerol, cOmplete™ EDTA-free Protease Inhibitor Cocktail tablets (1 tablet/ 50 ml lysate) and benzonase (0.1 µl/ 1 ml)). After lysis using a C3 Emulsiflex-C3 homogenizer (Avestin), the cell lysate was cleared by centrifugation at 4 ˚C and the protein was purified via Ni^{2+} affinity column chromatography. Fractions containing the protein of interest were combined and dialyzed to 150 mM NaCl, 20 mM Tris (pH=8.0), 5 mM DTT and 10% v/v glycerol.

TR-FRET coactivator recruitment assay. Assays were conducted using 100 nM N-terminal biotinylated SRC-1 box 2 peptide (Biotin-N-PSSHSSLTARHKILHRLLQEGSPSD-CONH2) and 20 nM His6-RORγt-LBD in buffer containing 10 mM HEPES, 150 mM NaCl, 5 mM DTT, 0.1% BSA (w/v) and 0.1 mM CHAPS (adjusted to pH 7.5). Terbium labeled anti-His antibody (CisBio Bioassays, 61HISTLA) and D2-labelled streptavidin (CisBio Bioassays, 610SADLA) were used at the concentrations recommended by the supplier. Compounds (dissolved in DMSO) were titrated using a 2 x dilution series in Corning white low volume, low binding, 384-well plates at a final volume of 10 µl. The final DMSO concentration was 2% (v/v) throughout. The plate was incubated at room temperature for 30 min and centrifuged before reading (excitation = 340 nm; emission = 665 nm and 620 nm) on a Tecan infinite F500 plate reader using the parameters recommended by CisBio Bioassays. The data were analyzed with Origin Software. The dose-response curve was fitted using the following equation:

$$y = A_1 + \frac{A_1 - A_2}{1 + 10^{(\log(x_0) - x)p}}$$

where y represents the FRET ratio (1000*acceptor/donor), A_1 is the bottom asymptote, A_2 is the top asymptote, p is the Hill slope, x_0 is the EC_{50} and x is the ligand concentration. Whenever the dose-response curves did not reach a bottom asymptote, the value of the negative control was used. Data recorded in triplicate from three independent experiments. Error bars represent the SD of the mean.

RORγt-LBD expression and purification (used for crystallography). The plasmid used for crystallography was ordered from GenScript. The pET15b vector incorporated human RORγt LBD

(AA265-507) with a C455H mutation to enhance crystallization. Using heat shock, the plasmid was transformed into E.Coli BL21 (DE3) cells. A single colony was used to culture overnight at 37°C in 25 ml of LB medium supplied with 100 µg/ml ampicillin. These cultures were transferred to 2 liters of 2x YT medium supplied with 0.05% antifoam SE-15 (Sigma Aldrich) with 100 µg/ml ampicillin. After an OD600 of 0.6 is reached, protein expression was induced by adding 0.25 mM IPTG. The protein expression continued overnight at 15°C. Using centrifugation at 10.000 RCF for 10 minutes at 4°C, the cell pellet was collected and thereafter dissolved in lysis buffer (20 mM Tris, 500 mM NaCl, 2 mM TCEP, 0.1% Tween20, 10% glycerol, 10 cOmplete™ Protease Inhibitor Cocktail tablets (Roche) and 25 U/ml Benzonase® Nuclease (Millipore), adjusted to pH=8.0). The cells were lysed using an Emulsiflex-C3 homogenizer (Avestin), and the crude protein solution was obtained by centrifugation at 40.000 RCF for 40 minutes at 4°C. This solution was loaded on a 5 ml Ni-NTA Superflow cartridge (QIAGEN) equilibrated with buffer A (20 mM Tris, 500 mM NaCl, 20 mM imidazole, 2 mM TCEP, 0.1% Tween20 and 10% glycerol). The column was washed with 10 column volumes (CVs) of buffer A and 10 CVs of buffer A with 50 mM imidazole to eliminate unspecific binding of proteins to the resin. The product was eluted from the column using 8 CVs of buffer A with 200 mM imidazole. The elution fraction was dialyzed overnight in buffer A without imidazole. In addition, 1.2 U/mg restriction-grade thrombin was added to the purified protein sample to remove the purification tag. The purified sample was then concentrated using an Amicon® Ultra centrifugal filter with a 10 kDa cutoff (Millipore) and loaded on a Superdex 75 pg 16/60 size-exclusion column (GE Life Sciences) using 20 mM Tris, 100 mM NaCl and 5 mM DTT (adjusted to pH=8.0) as running buffer. Fractions of 3 ml were collected and analyzed using a Q-TOF LC/MS (Waters Xevo G2) and the MassLynx 4 software package to combine fractions where the correct mass of RORγtC455H was found. These fractions were concentrated to a final concentration of 11.1 mg/ml, aliquoted and stored at -80°C.

X-ray crystallography FM26. The RORγtC455H solution (11.1 mg/ml) was mixed with 2 equivalents of FM26 (in DMSO) and incubated on ice for 1 hour. Next, the sample was centrifuged at 20.000 RCF for 20 minutes at 4°C to remove precipitated proteins. MRC-2 well crystallization plates (Hampton Research, sitting drop) were prepared using a Mosquito pipetting robot (TTP Labtech). Well-diffracting crystals were obtained by mixing 0.9 µl of protein solution with 0.3 µl of 1.6-2.0 M ammonium sulfate and 0.1 M Tris (pH=8.5). The well was filled with 80 µl precipitant solution and plates were placed at 20°C. Crystals could be observed after one hour of incubation and grew to their final size overnight. The crystals were cryoprotected by briefly transferring the crystals to a solution containing 1.2 M $AmSO_4$, 0.1 M Tris (pH=8.5) and 25% glycerol before being flash cooled in liquid nitrogen. Diffraction data were collected at 100 K at the P11 beamline of the PETRA III facility at DESY (Hamburg, Germany) and processed using the CCP4i2 suite (version 7.0.075).[33] DIALS was used to integrate and scale the data.[34] The data was phased with PHASER using 5C4O as a molecular replacement model and ligand restraints of FM26 were generated with AceDRG.[35,36] Sequential

model building and refinement were performed with COOT and REFMAC, respectively.[37,38] Final refinement was performed using phenix.refine from the Phenix software suite (version 1.16_3459).[39,40] PyMOL (version 2.2.3, Schrödinger) was used to make the figures.[41] The structure of RORγtC455 in complex with FM26 was deposited in the protein data bank (PDB) under code 6SAL.

X-ray crystallography compound 13. Compound 13 was dissolved in 50% DMSO and 50% EtOH to a final concentration of 20 mM. One equivalent of compound 13 was added to the RORγt protein solution and the mixture was placed on ice (higher equivalents of compound 13 did not yield any crystals). The crystal plate setup was performed using the same steps as for FM26. The resulting crystal was briefly transferred to a cryo-solution containing 1.6M $AmSO_4$, 0.1M Tris, 25% glycerol and 200 µM compound 13 (adjusted to pH 8.5) before being flash-cooled. The crystal was measured at the i24 microfocus beamline of the Diamond Light Source (Oxford, United Kingdom). Data processing was performed using the same protocol as FM26. However, STARANISO was used to correct for the anisotropic diffraction.[42] The structure of RORγtC455H in complex with compound 13 was deposited in the PDB under code 6TLM.

Constructs

His6-RORγt (pET15b)

MGSSHHHHHHSSGLVPRGSHMASLTEIEHLVQSVCKSYRETCQLRLEDLLRQRSNIFSREEVTGYQRK
SMWEMWERCAHHLTEAIQYVVEFAKRLSGFMELCQNDQIVLLKAGAMEVVLVRMCRAYNADNRTVFFE
GKYGGMELFRALGCSELISSIFDFSHSLSALHFSEDEIALYTALVLINAHRPGLQEKRKVEQLQYNLE
LAFHHHLCKTHRQSILAKLPPKGKLRSLCSQHVERLQIFQHLHPIVVQAAFPPLYKELFS

His6-RORγtC455S (pET15b)

MGSSHHHHHHSSGLVPRGSHMASLTEIEHLVQSVCKSYRETCQLRLEDLLRQRSNIFSREEVTGYQRK
SMWEMWERCAHHLTEAIQYVVEFAKRLSGFMELCQNDQIVLLKAGAMEVVLVRMCRAYNADNRTVFFE
GKYGGMELFRALGCSELISSIFDFSHSLSALHFSEDEIALYTALVLINAHRPGLQEKRKVEQLQYNLE
LAFHHHLSKTHRQSILAKLPPKGKLRSLCSQHVERLQIFQHLHPIVVQAAFPPLYKELFST

His6-RORγtC455H (pET15b)

MGSSHHHHHHSSGLVPRGSHMASLTEIEHLVQSVCKSYRETCQLRLEDLLRQRSNIFSREEVTGYQRK
SMWEMWERCAHHLTEAIQYVVEFAKRLSGFMELCQNDQIVLLKAGAMEVVLVRMCRAYNADNRTVFFE
GKYGGMELFRALGCSELISSIFDFSHSLSALHFSEDEIALYTALVLINAHRPGLQEKRKVEQLQYNLE
LAFHHHLHKTHRQSILAKLPPKGKLRSLCSQHVERLQIFQHLHPIVVQAAFPPLYKELFS
ABCD = Purification tag

Supporting Information

Table S1 | Data collection and refinement statistics for the crystal structure of RORγt in complex with FM26 and Glenmark's compound 13.

	RORγt + FM26	**RORγt + compound 13**
Data collection		
Space group	P 6_1 2 2	P 6_1 2 2
Cell dimensions		
a, b, c (Å)	107.6, 107.6, 100.1	107.5 107.5 98.7
α, β, γ (°)	90, 90, 120	90, 90, 120
Resolution (Å)	47.38-1.61 (1.67-1.61)	93.12-2.32 (2.40-2.32)
I / σ(I)	25.0 (1.17)	6.9 (0.8)
Completeness (%)	97.77 (81.55)	100.00 (100.00)
Redundancy	28.3 (7.4)	35.9 (36.5)
$CC_{1/2}$	0.99 (0.439)	0.992 (0.422)
Refinement		
No. unique reflections	43698	15190 (1448)
Rwork/Rfree	0.181/0.203	0.2054/0.2520
No. atoms (non-H)		
Protein	1992	2020
Ligand	32	28
Water	257	23
Average B-factors		
Protein	37.26	58.86
Ligand	29.11	52.19
Water	49.88	57.94
R.m.s. deviations		
Bond lengths (Å)	0.008	0.016
Bond angles (°)	1.13	2.024
PDB ID	6SAL	6TLM

Table S2 | IC_{50} and Hill-slope values observed in the competitive TR-FRET cofactor recruitment assay.

	0 µM cholesterol		0.25 µM cholesterol		1.0 µM cholesterol	
compound	IC_{50} (nM)	Hill slope	IC_{50} (nM)	Hill slope	IC_{50} (nM)	Hill slope
FM26	247.8 ± 17.7	–0.77 ± 0.04	138.0 ± 5.9	–0.86 ± 0.03	94.1 ± 3.3	–1.01 ± 0.03
CPD13	547.3 ± 60.1	–0.74 ± 0.06	299.5 ± 18.0	–0.87 ± 0.04	268.9 ± 18.8	–0.90 ± 0.05
MRL-871[14]	12.7 ± 0.6	–0.97 ± 0.04	9.4 ± 0.3	–1.04 ± 0.03	7.8 ± 0.2	–1.20 ± 0.03
digoxin	7012 ± 588	–0.76 ± 0.05	33620 ± 1649	–0.77 ± 0.03	85400 ± 4276	–1.01 ± 0.06

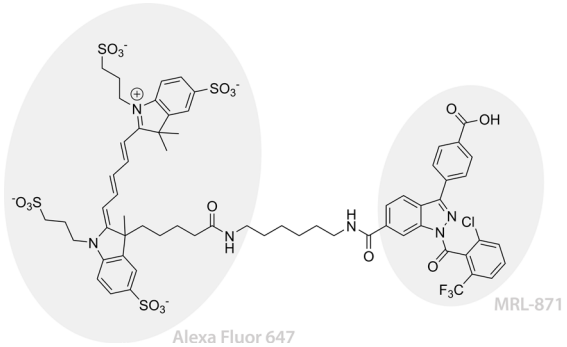

Figure S1 | Chemical structure of AlexaFluor-MRL-871 probe.

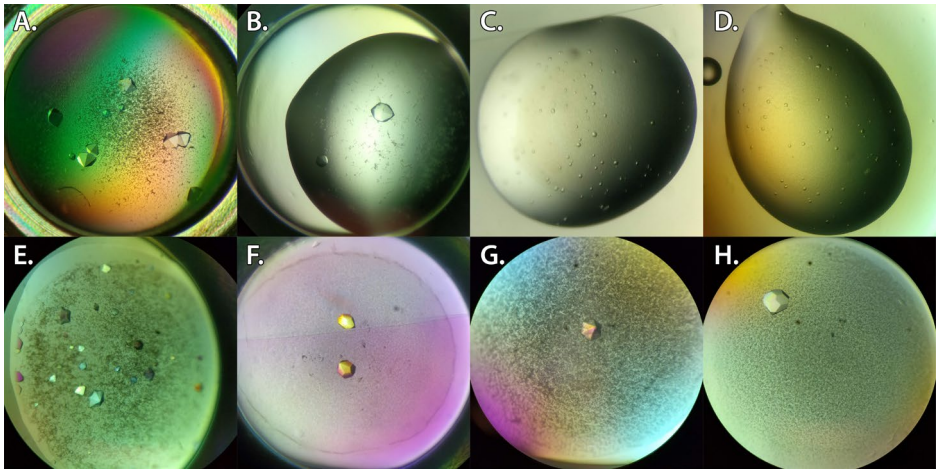

Figure S2 | Representative RORγt LBD crystals. A-B. Wildtype RORγt. **C-D.** RORγtC455S. **E-H.** RORγtC455H crystals.

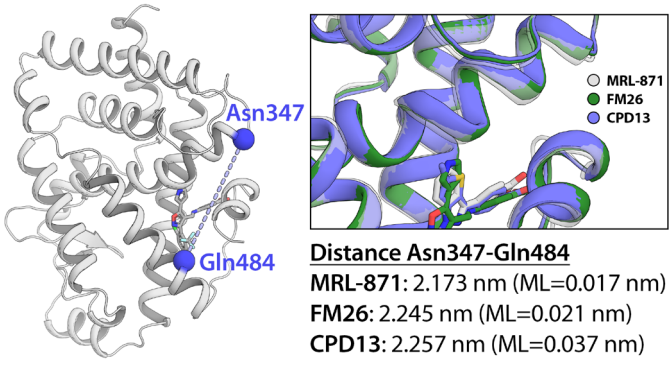

Figure S3 | Distance between the α-carbons (blue spheres) of Asn347 (helix 4) and Gln484 (helix 11) in the crystal structures. The maximum-likelihood coordinate error (ML) is provided for every structure.

Acknowledgements

Sanne van Zanten and Mario van Zeeland from Lead Pharma (Oss, The Netherlands) are gratefully acknowledged for their input in the RORγt construct optimization for crystallography. Femke A. Meijer, Richard G. Doveston and Iris A. Leijten-van de Gevel are greatly acknowledged for the valuable discussions. The tutors of the DLS-CCP4 Data Collection and Structure Solution Workshop 2017 at the Diamond Light Source (Oxfordshire, UK) are greatly acknowledged.

References

1. Mease, P. J. *et al.* Ixekizumab, an interleukin-17A specific monoclonal antibody, for the treatment of biologic-naive patients with active psoriatic arthritis: Results from the 24-week randomised, double-blind, placebocontrolled and active (adalimumab)-controlled period of the phase III trial SPIRIT-P1. *Ann. Rheum. Dis.* **76**, 79–87 (2017).
2. Attia, A. *et al.* Safety and Efficacy of Brodalumab for Moderate-to-Severe Plaque Psoriasis: A Systematic Review and Meta-Analysis. *Clinical Drug Investigation* vol. 37 439–451 (2017).
3. Hueber, W. *et al.* Effects of AIN457, a fully human antibody to interleukin-17A, on psoriasis, rheumatoid arthritis, and uveitis. *Sci. Transl. Med.* **2**, 52ra72 (2010).
4. Lock, C. *et al.* Gene-microarray analysis of multiple sclerosis lesions yields new targets validated in autoimmune encephalomyelitis. *Nat. Med.* **8**, 500–508 (2002).
5. Burkett, P. R. & Kuchroo, V. K. IL-17 Blockade in Psoriasis. *Cell* vol. 167 1669 (2016).
6. Duerr, R. H. *et al.* A genome-wide association study identifies IL23R as an inflammatory bowel disease gene. *Science (80-.).* **314**, 1461–1463 (2006).
7. Fauber, B. P. & Magnuson, S. Modulators of the nuclear receptor retinoic acid receptor-related orphan receptor-γ (RORγ or RORc). *Journal of Medicinal Chemistry* vol. 57 5871–5892 (2014).
8. Sun, N., Guo, H. & Wang, Y. Retinoic acid receptor-related orphan receptor gamma-t (RORγt) inhibitors in clinical development for the treatment of autoimmune diseases: a patent review (2016-present). *Expert Opin. Ther. Pat.* **29**, 663–674 (2019).
9. Qiu, R. & Wang, Y. Retinoic Acid Receptor-Related Orphan Receptor γt (RORγt) Agonists as Potential Small Molecule Therapeutics for Cancer Immunotherapy. *Journal of Medicinal Chemistry* vol. 61 5794–5804 (2018).
10. Moore, T. W., Mayne, C. G. & Katzenellenbogen, J. A. Minireview: Not picking pockets: Nuclear receptor alternate-site modulators (NRAMs). *Molecular Endocrinology* vol. 24 683–695 (2010).
11. Tice, C. M. & Zheng, Y. J. Non-canonical modulators of nuclear receptors. *Bioorganic Med. Chem. Lett.* **26**, 4157–4164 (2016).
12. Fernandez, E. J. *Allosteric pathways in nuclear receptors — Potential targets for drug design*. vol. 183 152–159 (2018).
13. Scheepstra, M. *et al.* Identification of an allosteric binding site for RORγt inhibition. *Nat. Commun.* **6**, 1–10 (2015).
14. Meijer, F. A. *et al.* Ligand-Based Design of Allosteric Retinoic Acid Receptor-Related Orphan Receptor γt (RORγt) Inverse Agonists. *J. Med. Chem.* **63**, 241–259 (2020).
15. Jiang, X. *et al.* A Novel Series of Cysteine-Dependent, Allosteric Inverse Agonists of the Nuclear Receptor RORγt. *Bioorg. Med. Chem. Lett.* 126967 (2020) doi:10.1016/j.bmcl.2020.126967.
16. Meijer, F. A., Leijten-van de Gevel, I. A., de Vries, R. M. J. M. & Brunsveld, L. Allosteric small molecule modulators of nuclear receptors. *Mol. Cell. Endocrinol.* **485**, 20–34 (2019).
17. Karstens, W. F. J. et al W. F. J. *et al.* RORgammat inhibitors. *PCT Int. Appl.* (2012).

18. Gege, C. Retinoid-related orphan receptor γ t modulators: comparison of Glenmark's me-too patent application (WO2015008234) with the originator application from Merck Sharp and Dohme (WO2012106995). *Expert Opin. Ther. Pat.* **25**, 1215–1221 (2015).
19. Chaudari, S. S. *et al.* Bicyclic Heterocyclic compounds as ROR Gamma Modulators. WO2015008234 (2015).
20. Kallen, J. *et al.* Structural States of RORγt: X-ray Elucidation of Molecular Mechanisms and Binding Interactions for Natural and Synthetic Compounds. *ChemMedChem* **12**, 1014–1021 (2017).
21. Durst, R. A. & Staples, B. R. Tris/Tris-HCl: a standard buffer for use in the physiologic pH range. *Clin. Chem.* **18 3**, 206–208 (1972).
22. Belushkin, A. A. *et al.* Sequence-derived structural features driving proteolytic processing. *Proteomics* **14**, 42–50 (2014).
23. Yang, T. *et al.* Discovery of tertiary amine and indole derivatives as potent RORγt inverse agonists. *ACS Med. Chem. Lett.* **5**, 65–68 (2014).
24. Bošnjak, I., Bojović, V., Šegvić-Bubić, T. & Bielen, A. Occurrence of protein disulfide bonds in different domains of life: a comparison of proteins from the Protein Data Bank. *Protein Eng. Des. Sel.* **27**, (2014).
25. Fauber, B. P. *et al.* Structure-based design of substituted hexafluoroisopropanol- arylsulfonamides as modulators of RORc. *Bioorganic Med. Chem. Lett.* **23**, 6604–6609 (2013).
26. Hirata, K. *et al.* SAR Exploration Guided by le and Fsp3: Discovery of a Selective and Orally Efficacious RORγ Inhibitor. *ACS Med. Chem. Lett.* **7**, 23–27 (2016).
27. Olsson, R. I. *et al.* Benzoxazepines Achieve Potent Suppression of IL-17 Release in Human T-Helper 17 (TH17) Cells through an Induced-Fit Binding Mode to the Nuclear Receptor RORγ. *ChemMedChem* **11**, 207–216 (2016).
28. Tanis, V. M. *et al.* 3-Substituted Quinolines as RORγt Inverse Agonists. *Bioorganic Med. Chem. Lett.* **29**, 1463–1470 (2019).
29. Eberhardt, J., Mcewen, A. G., Bourguet, W., Morasa, D. & Dejaegerea, A. A revisited version of the apo structure of the ligand-binding domain of the human nuclear receptor retinoic x receptor a. *Acta Crystallogr. Sect. F Struct. Biol. Commun.* **75**, 98–104 (2019).
30. Wurtz, J. M. *et al.* A canonical structure for the ligand-binding domain of nuclear receptors. *Nat. Struct. Biol.* **3**, 87–94 (1996).
31. Nolte, R. T. *et al.* Ligand binding and co-activator assembly of the peroxisome proliferator-activated receptor-gamma. *Nature* **395**, 137–43 (1998).
32. Karstens, W. F. J. et al. RORgammaT Inhibitors. *PCT Int. Appl.* (2012).
33. Potterton, L. *et al.* CCP4i2: the new graphical user interface to the CCP4 program suite. *Acta Crystallogr. Sect. D Struct. Biol.* **74**, 68–84 (2018).
34. Clabbers, M. T. B. *et al.* Electron diffraction data processing with *DIALS*. *Acta Crystallogr. Sect. D Struct. Biol.* **74**, 506–518 (2018).
35. McCoy, A. J. Solving structures of protein complexes by molecular replacement with Phaser. *Acta Crystallogr. D. Biol. Crystallogr.* **63**, 32–41 (2007).
36. Long, F. *et al. AceDRG*: a stereochemical description generator for ligands. *Acta Crystallogr. Sect. D Struct. Biol.* **73**, 112–122 (2017).
37. Emsley, P., Lohkamp, B., Scott, W. G. & Cowtan, K. Features and development of *Coot*. *Acta Crystallogr. Sect. D Biol. Crystallogr.* **66**, 486–501 (2010).
38. Murshudov, G. N. *et al.* REFMAC5 for the refinement of macromolecular crystal structures. *Acta Crystallogr. D. Biol. Crystallogr.* **67**, 355–67 (2011).
39. Afonine, P. V. *et al.* Towards automated crystallographic structure refinement with phenix.refine. *Acta Crystallogr. Sect. D Biol. Crystallogr.* **68**, 352–367 (2012).
40. Liebschner, D. *et al.* Macromolecular structure determination using X-rays, neutrons and electrons: Recent developments in Phenix. *Acta Crystallogr. Sect. D Struct. Biol.* **75**, 861–877 (2019).

41. Schrodinger LLC. *The PyMOL Molecular Graphics System, Version 2.2.3*. (Schrödinger LLC, 2015).
42. Tickle, I. J. *et al. STARANISO*. http://staraniso.globalphasing.org/cgi-bin/staraniso.cgi (2018).

TR-FRET assays were performed by Femke A. Meijer and Iris A. Leijten-van de Gevel expressed and purified the RORγt protein used for the TR-FRET assays.

CHAPTER 5

Elucidation of the Mechanism of Cooperative Dual Ligand Binding to RORγt

Abstract

Cooperative ligand binding is a common and important phenomenon in biological systems where ligand binding influences the binding of another ligand at a different site of the protein via an intramolecular network. The underlying mechanism behind cooperative binding remains poorly understood, primarily due to the lack of structural data of these ternary complexes. Using TR-FRET studies, we show that cooperative ligand binding occurs for RORγt, a nuclear receptor associated with the pathogenesis of autoimmune diseases. We solved twelve crystal structures of RORγt simultaneously bound to various orthosteric and allosteric ligands. The presence of the orthosteric ligand induces a clamping motion of the allosteric pocket via helix 4-5. Molecular dynamics simulations revealed an unusual mechanism behind this clamping motion, highlighting the ability of Ala355 to shift between helix 4 and 5. The orthosteric ligand was shown to regulate the absolute conformation of Ala355 and thereby to indirectly determine the conformation of the allosteric pocket.

Part of this work will be published as: R. M. J. M. de Vries, F. A. Meijer, R. G. Doveston, et al. Cooperativity in Ligand Binding between the Orthosteric and Allosteric Binding Sites of RORγt. *Submitted*. (2020)

Introduction

Allosteric ligands interact with pockets on the protein that are distinct from the canonical, orthosteric ligand-binding pocket (LBP). Therefore, allosteric ligands exert their effect through a different structural mechanism compared to the endogenous ligand.[1–3] Modulation of proteins via allosteric pockets can convey significant advantages over the orthosteric pocket. Allosteric ligands do not compete with the endogenous ligand for the same pocket and can achieve high target selectivity because their interaction is not limited to a single pocket. For some protein classes, the orthosteric LBP can be highly conserved across a receptor family, making it challenging to selectively target a single receptor via the classical, canonical approach.[1] Therefore, allosteric targeting of proteins is a prominent and auspicious subject in drug discovery. In the last decades, multiple allosteric ligands have been developed for important protein classes, including G-protein coupled receptors (GPCRs)[4,5] and kinases[6]. Some have since been approved by the FDA and are now marketed drugs.[7,8]

Although the orthosteric and allosteric LBPs are not physically overlapping, binding of the endogenous ligand can influence the binding behavior at an allosterically remote site, and vice versa. There is a particular interest for ligands that enhance the binding affinity of the other ligand, a phenomenon called cooperative dual ligand binding, which enhances the pharmacological response.[9–11] Cooperative dual ligand binding has been demonstrated for GPCR ligands.[12,13] However, the structural mechanism that enables dual ligand cooperativity remains poorly understood.[14] This, in part, results from the absence of high-resolution structural data, required to visualize the effects of dual ligand binding on the protein conformation. A mechanical understanding of how cooperative dual ligand binding can occur is essential to design allosteric ligands with a robust cooperative character.

Dual ligand binding has recently been demonstrated for NRs[15,16], a family of transcription factors which activity is modulated by endogenous and synthetic ligands.[17] Because of their essential role in gene transcription, NRs have been a prominent target for drug discovery, with 16% of all marketed drugs targeting this protein class.[18] The retinoic acid receptor-related orphan receptor γ t (RORγt) is an NR that is essential for T helper 17 (Th17) cell differentiation, and impaired proper functioning of this NR is associated with the pathogenesis of autoimmune diseases.[19–21] Disruption of the Th17/IL17 pathway can be achieved by inhibition of RORγt with small molecules and has been demonstrated to reduce the inflammatory response.[20,22,23] The LBD of RORγt contains an enclosed

orthosteric LBP that allows binding of both endogenous and synthetic small molecules (Figure 1A-B).[24–26] In addition, RORγt consists of an allosteric pocket composed of helices 3, 4, 11 and helix 12, that was shown to bind high-affinity allosteric inverse agonists (Figure 1).[27–31] Comparison of the crystal structures of the RORγt LBD in complex with either an orthosteric or allosteric modulator suggests that both ligands can simultaneously interact with the receptor (Figure 1B). Previous studies already produced some evidence for a potential interplay between both pockets.[29,31]

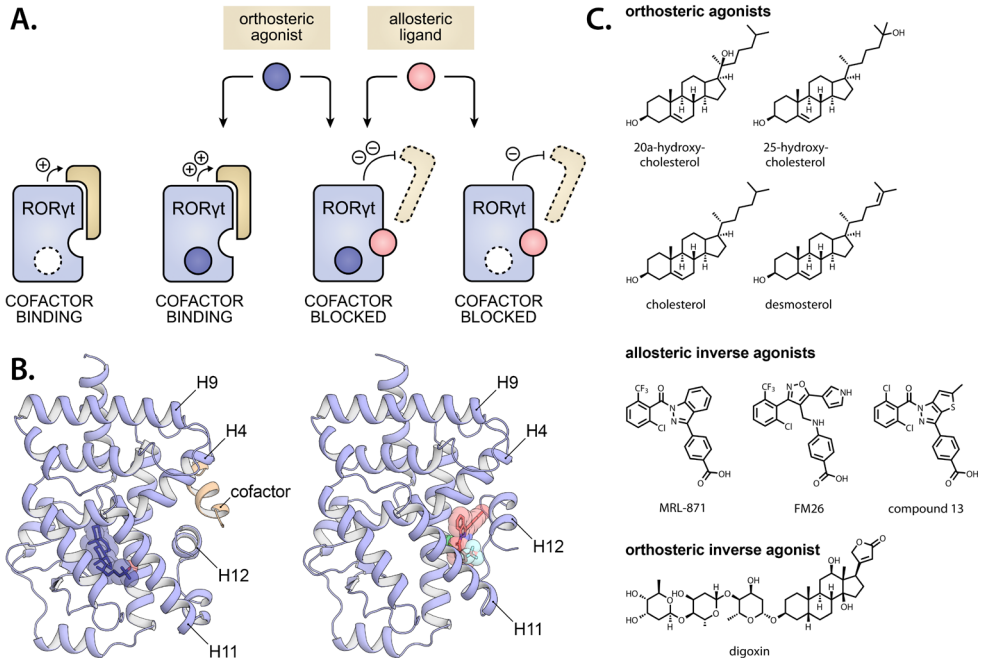

Figure 1 | Dual ligand binding in RORγt. A. Schematic illustration of the effect of orthosteric (blue) and allosteric modulators (pink) on the coactivator (wheat colored shape) recruitment of RORγt. Apo RORγt is intrinsically active and recruits coactivators. Binding of agonists enhances coactivator binding while binding of an allosteric inverse agonist blocks coactivator binding. The presence of both orthosteric and allosteric ligands can lead to more effective inhibition of coactivator recruitment through cooperative binding. **B.** Crystal structure of the LBD of RORγt in complex with the agonist 25-hydroxycholesterol bound to the orthosteric pocket (left; PDB: 3L0L), and the inverse agonist MRL-871 in the allosteric pocket (right; PDB: 5C4O). Both ligands induce a different conformation of helix 12, thereby regulating cofactor recruitment. **C.** Chemical structures of the orthosteric agonists (20α-hydroxycholesterol, 25-hydroxycholesterol, cholesterol and desmosterol), orthosteric inverse agonist (digoxin) and allosteric inverse agonists (MRL-871, FM26 and compound 13) of RORγt used for this study.

In this chapter, the existence of cooperative dual ligand binding in RORγt is confirmed using comprehensive biochemical and crystallography studies in the presence of both orthosteric and allosteric ligands. Careful analysis of the structural data revealed a subtle mechanism responsible for cooperative ligand binding in RORγt. Ultimately, molecular dynamics (MD) simulations of the crystal structures uncovered the precise molecular mechanism by which the ligands positively influence each other's potency.

Results and discussion

The recruitment of coactivators, and the associated transcriptional response, is dependent on the constitutive activity of the RORγt LBD and the presence of ligands (Figure 1A). The conformation of the C-terminal helix 12 is essential for the interaction with coactivators and can be modulated by ligands. A set of RORγt ligands was selected to evaluate if cooperative dual ligand binding occurs for RORγt (Figure 1C). Cholesterol and its derivatives 20α-hydroxycholesterol, 25-hydroxycholesterol, and desmosterol are established RORγt agonists and interact with the orthosteric LBP.[25,32] Digoxin interacts with the orthosteric pocket but instead destabilizes the active conformation of helix 12, thereby acting as an inverse agonist.[33] MRL-871[27,28], FM26[29] and Glenmark's compound 13[30,31,34] are chemically distinct inverse agonists that bind to an allosteric pocket of RORγt and prevent coactivator binding (Figure 1B-C).[28]

Dual ligand binding enhances the thermal stability of the RORγt LBD

The thermal stability of a protein can be enhanced upon binding of a ligand through changes in the protein dynamics and the overall fold.[35,36] Therefore, the melting temperature shift (ΔT_m) of RORγt can be used to indicate dual ligand binding.[36,37] The orthosteric agonist 20α-hydroxycholesterol increased the ΔT_m of RORγt by 3.6 °C compared to DMSO, demonstrating the enhanced thermal stability upon ligand binding (Figure 2, blue bar). Likewise, the binding of the allosteric ligands enhanced the thermal stability of RORγt with 1 to 7 °C (Figure 2, pink bars). Combining the allosteric ligands with 20α-hydroxycholesterol resulted in an increased ΔT_m of 7-14 °C, significantly exceeding the combined ΔT_m of both ligands (Figure 2, blue bars). The enhanced thermal stability of RORγt indicates that both ligands can bind RORγt simultaneously and hints at cooperativity between the orthosteric and allosteric sites.

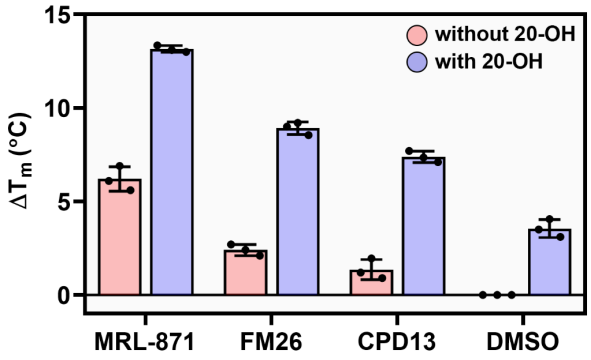

Figure 2 | Thermal stability assay of RORγt in the presence of orthosteric and allosteric ligands. Summary of the melting temperature shift (ΔT_m) of RORγt with MRL-871, FM26 or compound 13 (CPD13), in the presence (blue bars) and absence (pink bars) of 20α-hydroxycholesterol (20-OH). Data recorded in triplicate from three independent experiments. Data are presented as mean ΔT_m (corrected to DMSO) ± standard deviation (SD).

Orthosteric RORγt ligands enhance the potency of allosteric RORγt ligands

The effect of dual ligand binding on coactivator displacement was determined using a TR-FRET assay.[38] In the absence or presence of an agonist, a d2-labeled coactivator peptide and a terbium-cryptate-labeled anti-His antibody interact with RORγt, generating a high FRET signal (Figure S1). The orthosteric cholesterol derivatives further enhanced the FRET signal dose-dependently, demonstrating their agonistic behavior (dose-response curves and EC_{50}/IC_{50} values in Figure S2 and Table S1).[21,32] However, 25-hydroxycholesterol appears to act as a weak partial inverse agonist, while it has been reported as an agonist before (Figure S2A).[21,32] The affinity of the orthosteric inverse agonist digoxin could be reduced in the presence of cholesterol, confirming that both ligands compete for the same pocket (Figure S2D, Table S2).[29] The inverse agonistic behavior of the allosteric ligands has already been demonstrated previously using this TR-FRET assay format (Figure S2C).[28,29,31]

The effect of dual ligand binding on cofactor displacement was evaluated by producing the dose-response curves of the allosteric ligand titrations in the presence and absence of the orthosteric ligands (Figure 3). Interestingly, fixed concentrations of all the orthosteric cholesterol derivatives enhanced the binding affinity of the allosteric ligands (Figure 3, Figure S3 and Table S2). Increasing the concentration of the orthosteric ligands leads to a left-shift of the dose-response curves and a steeper Hill slope (Table S2),

suggesting synergistic binding of the ligands (Figure 3, Figure S3). These data provide compelling evidence for cooperative dual ligand binding in RORγt.

From the orthosteric ligands, 25-hydroxycholesterol and desmosterol increased the affinity of the allosteric ligands more effectively than 20α-hydroxycholesterol and cholesterol (Figure 3 and Figure S3). For both 25-hydroxycholesterol and desmosterol, the

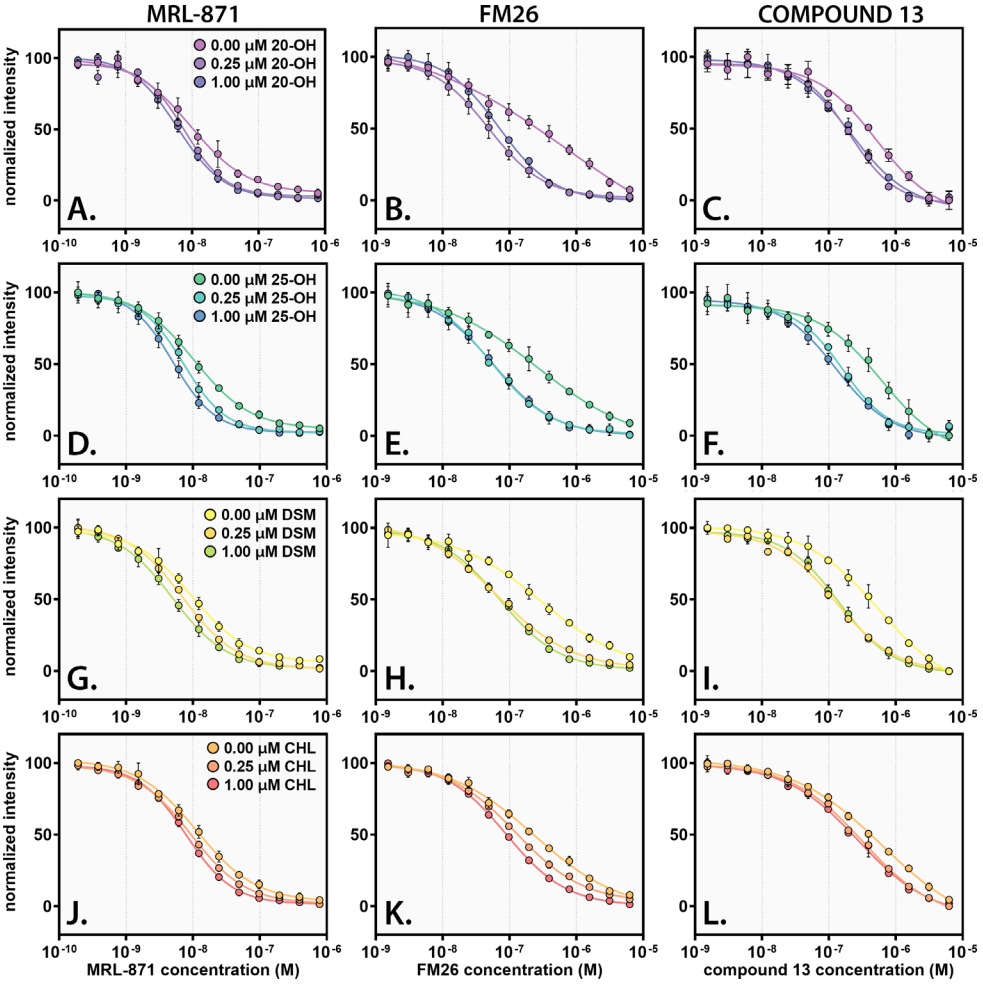

Figure 3 | Dose-response curves of competitive TR-FRET coactivator recruitment assays. A-L. Titration of allosteric ligands MRL-871 (**A**, **D**, **G** and **J**), FM26 (**B**, **E**, **H** and **K**) and compound 13 (**C**, **F**, **I** and **L**) to RORγt in the presence of fixed concentrations (0.00 µM, 0.25 µM and 1.00 µM) of 20α-hydroxycholesterol (20-OH; **A**-**C**), 25-hydroxycholesterol (25-OH; **D**-**F**), desmosterol (DSM; **G**-**I**) and cholesterol (CHL; **J**-**L**). The data were normalized with regards to plateau levels. The data for FM26 was adapted from Meijer *et al.* 2019.[29]

maximum cooperative response is established at an orthosteric ligand concentration of 0.25 µM, while 20α-hydroxycholesterol and cholesterol this is at 1.00 µM (Figure S3). These results suggest that the minor differences in the orthosteric ligand scaffold can have a meaningful impact on the binding affinity of the allosteric ligand.

Orthosteric ligands enhance the binding affinity of an MRL-871 probe

As an orthogonal approach to demonstrate that cooperative ligand binding occurs, the TR-FRET assay was modified by substituting the labeled coactivator peptide with an AlexaFluor647-labeled MRL-871 probe (Figure 4B). Like the other assay format, a high FRET signal is produced when the MRL-871 probe and the terbium cryptate antibody are into close proximity. However, this assay format directly determines allosteric recruitment instead of indirectly via a coactivator peptide. The MRL-871 probe is kept at a constant concentration at 50% of the maximum response. A dose-dependent increase of the FRET-signal is observed upon titration of any of the four orthosteric ligands, indicating an increased affinity of the MRL-871 probe for RORγt in the presence of increasing concentrations of orthosteric ligands (Figure 4A). The EC_{50} values determined by this assay format significantly rely on the affinity of the orthosteric ligand for the receptor. The more potent 20α-hydroxycholesterol can exhibit its cooperative binding behavior at lower

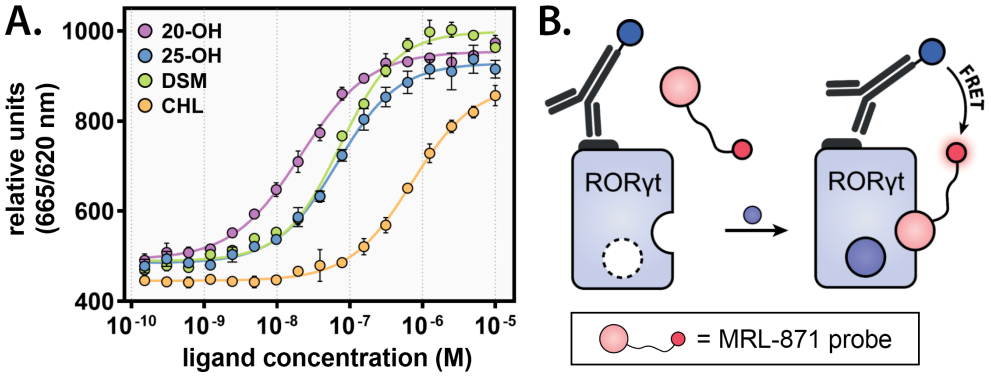

Figure 4 | Dose-response curves of a TR-FRET assay with an AlexaFluor647-MRL-871 allosteric probe. A. Titration of the orthosteric ligands 20α-hydroxycholesterol (20-OH), 25-hydroxycholesterol (25-OH), desmosterol (DSM) and cholesterol (CHL) to a fixed concentration of RORγt (20 nM) and allosteric MRL-871 probe (100 nM). **B.** Schematic representation of the TR-FRET assay using the AlexaFluor647-labeled MRL-871 probe. When the probe binds to the RORγt LBD, fluorescence emission occurs via FRET pairing between an anti-His terbium cryptate donor and the probe. Data recorded in triplicate from three independent experiments (one representative dataset shown). Error bars represent the SD of the mean.

concentrations than the less potent cholesterol. The EC_{50} values are, therefore, not indicative of the degree of cooperative ligand binding but rather confirm that orthosteric binding indeed effectively enhances the binding affinity of the MRL-871 probe.

Co-crystal structures provide detailed molecular insights into the simultaneous binding of orthosteric and allosteric RORγt ligands

X-ray protein crystallography was used to examine the impact of cooperative dual ligand binding on protein flexibility, protein folding and ligand binding modes. Crystal packing and buffer additives can significantly impact the overall fold and flexibility of parts of the protein. Therefore, conditions were screened that establish identical crystal packing. This allowed for a qualitative comparison of the crystal structures and minimized the possibility of crystallization artifacts (Figure S4 and Table S6). Using this approach, the first ternary complexes of RORγt bound to both an orthosteric and allosteric ligand were crystallized. In total, twelve novel high-resolution crystal structures were solved, including all combinations of the four orthosteric (20α-hydroxycholesterol, 25-hydroxycholesterol, desmosterol and cholesterol) and three allosteric ligands (MRL-871, FM26 and compound 13) (Figure 5D-O, Figure S12-23 and Table S3-5).

All twelve ternary RORγt crystal structures reveal the protein folded into a conformation where helix 12 is positioned over the allosteric ligand and thus physically preventing potential coactivator binding. This is consistent with the binary crystal structures of RORγt in complex with an allosteric modulator only.[28,29,31] Previously, we reported that allosteric ligands FM26 and compound 13 introduce more bulk towards helix 4 of RORγt compared to MRL-871. This shifts helix 4 towards helix 9.[29,31] Interestingly, the additional binding of an orthosteric ligand is seen to reverse this process in all the ternary crystal structures containing an orthosteric ligand and FM26 or compound 13 (Figure 6A). For the structures containing MRL-871, a similar but less pronounced effect is observed.

Superposition of the crystal structures showed that the binding modes of the cholesterol derivatives are comparable to those seen in earlier binary structures of RORγt in complex with the orthosteric ligands 20α- and 25-hydroxycholesterol (PDB: 3KYT and 3L0L respectively).[32] Comparison of the orthosteric pockets shows that the conformation of surrounding residues is predominantly unaffected by binding of the cholesterol derivatives , which is the same for the allosteric pocket. However, an altered conformation was observed for Met365, which was oriented towards the center of the orthosteric

pocket in the absence of an orthosteric ligand (Figure 5). The cholesterol derivatives occupy this part of the pocket, thereby "locking" Met365 in a distinctly repositioned conformation (Figure 6). This Met365 repositioning restricts the movement of helix 5 and

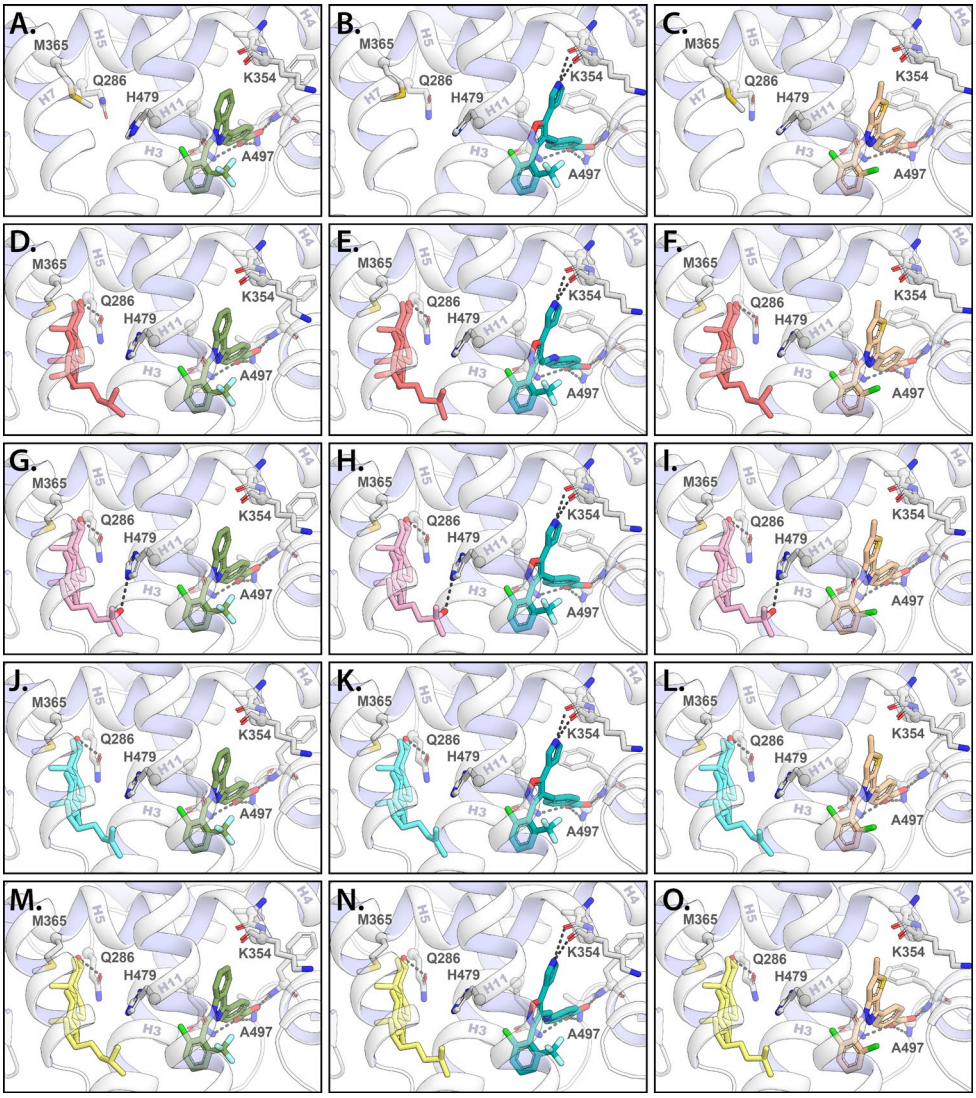

Figure 5 | Crystal structures of RORγt in complex with orthosteric and allosteric ligands. A-C. Focused view of the orthosteric and allosteric ligand-binding pockets from the previously published crystal structures containing only an allosteric ligand (MRL-871 (PDB: 5C4O) in green; FM26 (PDB: 6SAL) in teal or compound 13 (PDB: 6TLM) in brown). **D-O.** The orthosteric and allosteric ligand-binding pocket of RORγt in the presence of 12 combinations of orthosteric and allosteric ligands (20α-hydroxycholesterol in red, 25-hydroxycholesterol in pink, desmosterol in blue and cholesterol in yellow).

leads to a modest but relevant conformational change of helix 4 towards the allosteric ligand, a clamping effect observed in all the crystal structures (Figure 6A and Figure S7). The distance between α-carbons of Asn347 on helix 4 and Gln484 on helix 11 is used as a measure for the clamping motion (Figure S7). Although an allosteric ligand restricts the movement of helix 4, the presence of the orthosteric ligands further reduces this distance by 1 Å. Compared to the orthosteric ligand-free structures, an altered conformation for the allosteric ligands is observed, following the motion of helix 4 (Figure 6A and Figure S6). A larger movement of helix 4 towards the allosteric ligand is correlated with a larger twist of the allosteric ligand (Figure S6). Consequently, the conformation of the loop between helix 11 and 12 changes due to the polar interactions of the conserved carboxylic acid of the allosteric ligands with the protein backbone. Altogether, the structural data reveal a molecular mechanism of how an orthosteric ligand influences the binding of the allosteric ligand.

Orthosteric ligands restrict conformational flexibility of RORγt Met365 and alter the conformation of helix 7 and 11

MD simulations were performed to investigate the interplay between orthosteric and allosteric ligand binding. For this, cocrystal structures of RORγt in complex with both ligands were compared to the respective structure with only the allosteric modulator bound. To improve the reliability of the simulations, five independent simulations were performed per complex, each starting from a random initial velocity distribution.

For all simulations, no substantial conformational changes in the tertiary structure of the protein or ligand conformation were observed (Figure S9-11). The presence of any orthosteric ligand significantly reduced the overall flexibility of the complete protein backbone (Figure S9-11). Consistent with the crystal structures, Met365 of RORγt showed limited conformational freedom in the orthosteric pocket due to steric hindrance with the C-ring of the cholesterol derivatives. The specific conformation of Met365 leads to a repositioning of Ile400 on helix 7, thereby shifting this helix away from helix 5 (Figure 7B). The aliphatic tail of the cholesterol derivatives is oriented towards Leu483 on helix 11, causing this helix to move towards the allosteric ligand, restricting the overall mobility of both the allosteric ligand and helix 11 (Figure 7B and Supplementary Figure S9-11).

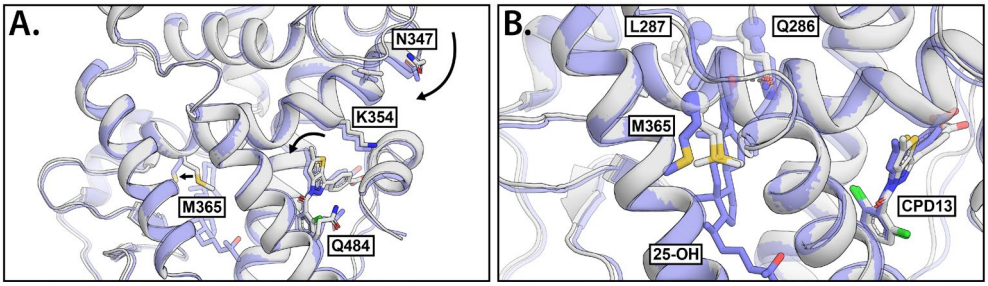

Figure 6 | Comparison of the crystal structures of RORγt in the presence (semi-transparent blue; PDB: 6T50) or absence (white; PDB: 6TLM) of an orthosteric modulator. A. The presence of the orthosteric modulator shifts helix 4 towards the allosteric pocket, thereby clamping the allosteric ligand. **B.** Focused view of the orthosteric ligand-binding pocket. Sidechains of Gln286, Leu287 and Met365 are shown for all crystal structures containing ligands in both pockets (twelve structures in blue) as well as in the absence of an orthosteric modulator (three structures in white). The presence of the orthosteric ligand locks Met365 into a defined state, which is conserved for all twelve crystal structures containing orthosteric ligands.

Orthosteric ligands influence the helix participation of Ala355 resulting in the clamping of the allosteric LBP

We investigated the helix 4 shift observed in our crystallographic data upon binding the orthosteric ligand in more detail. The MD simulations revealed an unusual mechanism of by which this helix movement takes place. In the crystal structures, Ala355 is located at the end of helix 4, but during our simulations, Ala355 showed the ability to exchange its participation between helices 4 and 5. The RORγt structures containing both ligands significantly bias Ala355 towards the helix 5 conformation compared to the complexes with only the allosteric ligand present (Figure 7C-F). This altered equilibrium of conformations is more distinct for complexes with the bulkier allosteric ligands FM26 and compound 13 since these ligands promote the helix 4 conformation for Ala355 in the absence of an orthosteric ligand. The participation in helix 5 by Ala355 induces a shift of helix 4 towards the allosteric ligand, moving the ligand deeper into the allosteric binding pocket (Figure S8). In agreement with the crystal structures, an apparent clamping motion of helix 4 can be observed for all structures containing an orthosteric ligand, characterized by the distance between the α-carbons of Asn347 and Gln484 (Figure S7).

The effect of different orthosteric ligands on the conformation of Ala355 was determined by measuring the average number of H-bonds of Ala355 with the backbone of Val351 (helix 4) and Glu359 (helix 5), respectively (Figure 7D-F). The structures containing MRL-871 showed that, together with binding any of the orthosteric ligands, Ala355 is almost exclusively in the helix 5 conformation (Figure 7D). For the complex of RORγt with FM26 alone, Ala355 is primarily in the helix 4 conformation, but in the

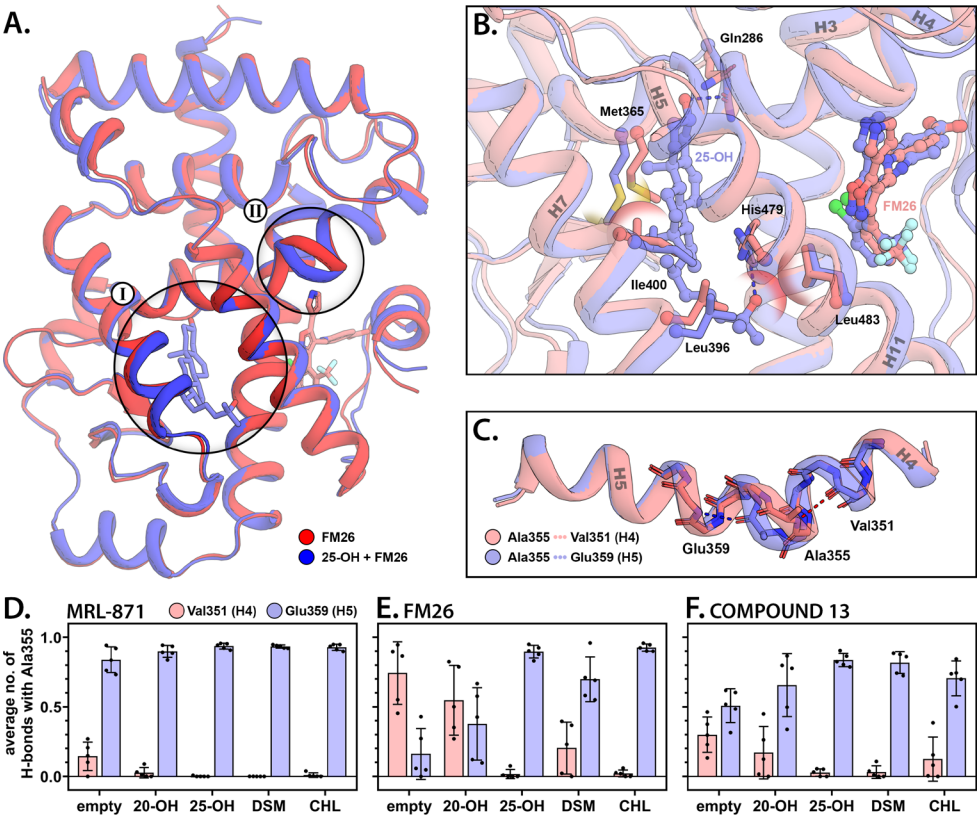

Figure 7 | Comparison of the RORγt complexes bound to an allosteric ligand in the presence (blue) or absence (red) of an orthosteric ligand using molecular dynamics. A. Superposition of the average structure of FM26 with and without 25-hydroxycholesterol. The orthosteric ligand-binding pocket (I) and the transition between helix 4 and 5 of RORγt (II) are highlighted. **B.** Focused view of the orthosteric ligand-binding pocket of RORγt. Polar interactions are shown as dashed lines and steric clashes as semi-transparent spheres. **C.** Isolated helix 4-5 showing the conformational switch of Ala355 from helix 4 to 5 upon orthosteric ligand binding. **D-F.** The average number of hydrogen bonds of Ala355 with Val351 (helix 4; red) or Glu359 (helix 5; blue) in the presence of different orthosteric and allosteric modulators throughout the simulation. Bars represent the average value over five independent simulations with the individual values represented as black spheres and the error bar showing the standard deviation.

presence of an orthosteric ligand, the equilibrium completely shifts towards helix 5 (Figure 7E). Similar behavior is observed for compound 13 (Figure 7F). For all structures containing 25-hydroxycholesterol, Ala355 appeared almost exclusively in the helix 5 conformation, independent of which allosteric ligand is bound. In contrast, 20α-hydroxycholesterol only had a minor effect on the conformational equilibrium. It appears that the flexibility of helix 5 plays a key role in defining the conformation of Ala355. Without an orthosteric ligand present, helix 5 acts as a flexible spring, allowing Ala355 to sample both conformations. Upon binding of an orthosteric ligand, the conformation of Met365 is locked, making the spring more rigid and promoting the helix 5 conformation. This provides an explanation of why orthosteric ligands with less conformational freedom in the LBP, due to additional polar interactions or more rigid alkene bonds for 25-hydroxycholesterol and desmosterol, respectively, more effectively induce the helix 5 conformation. The absolute conformation of Ala355 is directly correlated to the binding mode of the allosteric ligands. Therefore, the extent by which the orthosteric ligand adjusts the conformational equilibrium of this residue will define the cooperative binding behavior.

Conclusion

Cooperative dual ligand binding is a relevant but poorly understood concept in drug discovery. Instead of competing with an endogenous ligand, the endogenous ligand and an allosteric ligand can collaborate to produce a pharmacological response. It is difficult to rationally design ligands that show predictable cooperative binding behavior, primarily caused by a lack of structural understanding of the underlying cooperativity. In this work, we used a combination of biochemical data, protein crystallography, and MD simulations to produce a mechanistic explanation of how cooperative dual ligand binding occurs for the NR RORγt. The thermal shift data indicated cooperative stabilization of RORγt folding by dual ligand binding. The TR-FRET cofactor recruitment assays demonstrated the functional effect of the cooperative binding by an enhanced potency of the allosteric ligands in the presence of an orthosteric ligand. Although all orthosteric ligands show cooperative behavior in these TR-FRET data, they all do this to different extents. Desmosterol and 25-hydroxycholesterol provide the highest cooperative response, showing a significant improvement in IC_{50} values of the allosteric ligands, whereas cholesterol and 20α-hydroxycholesterol show only minor effects. In an orthogonal TR-

FRET assay format, we showed that orthosteric ligand binding increased the binding affinity of an allosteric probe, which provided additional evidence for cooperative dual ligand binding via a different molecular mechanism.

The determination of the ternary crystal structures of RORγt with all combinations of orthosteric and allosteric ligands allowed for the elucidation of a mechanistic explanation for the cooperative dual ligand binding behavior. Orthosteric ligands lock Met365 in a distinct conformation that leads to a conformational change of helix 4-5, which results in a clamping effect of the allosteric binding pocket. This results in a modest conformational change of the allosteric ligand. These small differences between crystal structures often go unnoticed because of a lack of proper reference structures, but they can be critical to explain protein functioning.[39] The generation of the twelve closely related ternary structures with identical crystal packing allowed for the qualitative detection of these differences.

MD simulations further confirmed the clamping behavior of the orthosteric pocket upon orthosteric ligand binding. The clamping motion was achieved by a yet, to our knowledge, unknown characteristic of Ala355. This residue demonstrated the ability to transition between the end of helix 4 and the beginning of helix 5, which plays a significant role in the clamping effect. Restricting the conformational flexibility of Met365 with an orthosteric ligand limits the movement of helix 4-5, promoting the helix 5 conformation of Ala355. This results in a conformational change of helix 4 towards the allosteric ligand. Owing to bulky functional groups, desmosterol and 25-hydroxycholesterol more effectively directed the absolute conformation of Ala355 to helix 5 compared to cholesterol and 20α-hydroxycholesterol. A similar trend was observed for these compounds in the TR-FRET data, where desmosterol and 25-hydroxycholesterol also induced the most substantial increase in potency for the allosteric ligands. This is likely caused by reduced flexibility of these ligands in the orthosteric LBP, thereby more effective locking Met365. Ultimately, the conformation of Ala355 is directly correlated to the binding mode and, as a result, the binding affinity of the allosteric ligand. Considering the TR-FRET data, the helix 5 conformation of Ala355, and the associated clamping motion of helix 4, shows to have a positive effect on the binding affinity of the allosteric ligand and explains the cooperative binding behavior.

Kojetin and coworkers already demonstrated the essential role of helix 4-5 in the allosteric regulation of dimerization and the AF-2 site of RXR.[39] The bent conformation of helix 4-5 is a common characteristic within the NR family. Like RORγt, most NR family

members contain a conformationally flexible residue at the transition between these two helices.[40] Therefore, it is likely that orthosteric ligand binding also has a significant effect on the dynamics and conformation of helix 4-5 of other NRs.[39] In addition to helix 12, helix 4 is essential for the recruitment of cofactors.[17] Therefore, the altered behavior of helix 4 resulting from orthosteric ligand binding could influence the cofactor binding behavior across all NRs.

In summary, our data provides the first mechanistic explanation for cooperative dual ligand binding in NRs, via a mechanism in RORγt that operates via an internal conformational change of the LBD. The specific RORγt cooperativity data in this study lets speculate that similar mechanistic concepts can also be found to govern other NRs and protein classes containing two binding sites. These mechanistic insights bring the pharmacological concept of cooperative dual ligand binding for NRs a step closer to implementation in NR drug discovery. The potential to further enhance the pharmacological effects of allosteric ligands by an interplay with the endogenous orthosteric NR ligands, provides a highly attractive entry for a novel NR pharmacology.

Experimental Section

RORγt-LBD expression and purification (used for TR-FRET assays). A pET15b expression vector encoding the human RORγt LBD (residues 265-518) with an N-terminal His-tag was transformed by heat shock into BL21(DE3) E. coli cells. Single colonies were used to inoculate precultures of 8 ml LB-media containing 100 µg/ml ampicillin. After overnight incubation at 37 ˚C, each preculture was transferred to 1 L TB media supplemented with ampicillin (100 µg/ml) and incubated at 37 ˚C until an OD600 of 1.0 was reached. Protein expression was then induced with 0.5 mM isopropyl-b-d-thiogalactoside (IPTG) and cultures were incubated overnight at 18˚C. The cells were collected by centrifugation and suspended in lysis buffer (300 mM NaCl, 20 mM Tris (pH=8.0), 20 mM imidazole, 1 mM TCEP, 10% v/v glycerol, cOmplete™, EDTA-free Protease Inhibitor Cocktail tablets (1 tablet/ 50 ml lysate) and 25 U/ml Benzonase® Nuclease (Millipore)). After lysis using an Emulsiflex-C3 homogenizer (Avestin), the cell lysate was cleared by centrifugation at 4 ˚C and the protein was purified via Ni^{2+}-affinity column chromatography. Fractions containing the protein of interest were combined and dialyzed to 150 mM NaCl, 20 mM Tris (pH=8.0), 5 mM DTT and 10% (v/v) glycerol.

Thermal shift assay. Thermal shift assays (TSA) were performed using 40 µL samples containing 2.5x SYPRO® Orange (Sigma), 5 µM RORγt-LBD, allosteric ligand (15 µM MRL-871, 60 µM FM26, 20 µM compound 13 (lowest concentrations giving a maximal ΔT_m)) in buffer containing 150 mM NaCl, 10 mM HEPES (pH=7.5), 1% DMSO and 1% ethanol. Measurements were performed in the presence

or absence of 60 µM 20α-hydroxycholesterol. The samples were heated from 35 °C to 75 °C at a rate of 0.3 °C per 15 s in a CFX96 Touch Real-Time PCR Detection System (Bio-Rad). Excitation (575/30 nm) and emission (630/40 nm) filters were used and the melting values were determined by extracting the minimum value of the negative derivative of the melting curve. Measurements were performed in triplicate and the data are presented as mean ± S.D from three independent experiments and normalized to DMSO.

TR-FRET coactivator recruitment assay. Assays were conducted using 100 nM N-terminal biotinylated SRC-1 box 2 peptide (Biotin-N-PSSHSSLTARHKILHRLLQEGSPSD-$CONH_2$) and 20 nM His-RORγt-LBD in buffer containing 10 mM HEPES, 150 mM NaCl, 5 mM DTT, 0.1% BSA (w/v) and 0.1 mM CHAPS (adjusted to pH=7.5). Terbium-labeled anti-His antibody (CisBio Bioassays, 61HISTLA) and D2-labeled streptavidin (CisBio Bioassays, 610SADLA) were used at the concentrations recommended by the supplier. Compounds (dissolved in DMSO) were titrated using a 2x dilution series in Corning white low volume, low binding, 384-well plates at a final volume of 10 µl. The final DMSO concentration was 2% (v/v) throughout. The plate was incubated at room temperature for 30 min and centrifuged before reading ($\lambda_{excitation}$ = 340 nm; $\lambda_{emission}$ = 665 nm and 620 nm) on a Tecan infinite F500 plate reader using the parameters recommended by CisBio Bioassays. The data were analyzed with Origin Software. The dose-response curve was fitted using the following equation:

$$y = A_1 + \frac{A_1 - A_2}{1 + 10^{(\log(x_0) - x)p}}$$

where y represents the FRET ratio (1000*acceptor/donor), A_1 is the bottom asymptote, A_2 is the top asymptote, p is the Hill slope, x_0 is the EC_{50} and x is the ligand concentration. Whenever the dose-response curves did not reach a bottom asymptote, the value of the negative control was used. Data recorded in triplicate from three independent experiments. Error bars represent the SD of the mean.

Competition TR-FRET coactivator recruitment assay. Competition assays were performed analogously to that described above only in the presence of fixed concentrations of 20α-hydroxycholesterol, 25-hydroxycholesterol, desmosterol or cholesterol: 0 µM (DMSO), 0.25 µM, 1.0 µM such that the final concentration of DMSO remained at 1.2% v/v.

MRL-871 probe recruitment TR-FRET assay. Assays were conducted using 100 nM Alexa647-labeled MRL-871 and 20 nM His6-RORγt-LBD in the buffer described above. A terbium-labeled anti-His antibody (CisBio Bioassays, 61HISTLA) was used at the concentrations recommended by the supplier.

RORγt-LBD expression and purification (used for crystallography). The plasmid used for crystallography was ordered from GenScript. The pET15b vector incorporated human RORγt LBD (AA265-507) with a C455H mutation to enhance crystallization. Using heat shock, the plasmid was

transformed into E.Coli BL21 (DE3) cells. A single colony was used to culture overnight at 37°C in 25 ml of LB medium supplied with 100 µg/ml ampicillin. These cultures were transferred to 2 L of 2x YT medium supplied with 0.05% antifoam SE-15 (Sigma Aldrich) with 100 µg/ml ampicillin. After an OD600 of 0.6 is reached, protein expression was induced by adding 0.25 mM IPTG. The protein expression continued overnight at 15°C. Using centrifugation at 10.000 RCF for 10 minutes at 4°C, the cell pellet was collected and dissolved in lysis buffer (20 mM Tris, 500 mM NaCl, 2 mM TCEP, 0.1% Tween20, 10% glycerol, 10 cOmplete™ Protease Inhibitor Cocktail tablets (Roche) and 25 U/ml Benzonase® Nuclease (Millipore), adjusted to pH=8.0). The cells were lysed using an Emulsiflex-C3 homogenizer (Avestin), and the crude protein solution was obtained by centrifugation at 40.000 RCF for 40 minutes at 4°C. This solution was loaded on a 5 ml Ni-NTA Superflow cartridge (QIAGEN), equilibrated with buffer A (20 mM Tris, 500 mM NaCl, 20 mM imidazole, 2 mM TCEP, 0.1% Tween20 and 10% glycerol). The column was washed with 10 column volumes (CVs) of buffer A and 10 CVs of buffer A with 50 mM imidazole to eliminate unspecific binding of proteins to the resin. The product was eluted from the column using 8 CVs of buffer A with 200 mM imidazole. The elution fraction was dialyzed overnight in buffer A without imidazole. In addition, 1.2 U/mg restriction-grade thrombin was added to the purified protein sample to remove the purification tag. The purified sample was then concentrated using an Amicon® Ultra centrifugal filter with a 10 kDa cutoff (Millipore) and loaded on a Superdex 75 pg 16/60 size-exclusion column (GE Life Sciences) using 20 mM Tris, 100 mM NaCl and 5 mM DTT (adjusted to pH=8.0) as running buffer. Fractions of 3 ml were collected and analyzed using a Q-TOF LC/MS only to combine fractions where the correct mass of RORγtC455H was found. These fractions were concentrated to a final concentration of 11.1 mg/ml, aliquoted and stored at -80°C.

X-ray crystallography. Allosteric ligands MRL-871, FM26 and compound 13 were dissolved in DMSO to a final concentration of 40 mM, 30 mM and 20 mM, respectively. The cholesterol derivatives were poorly soluble in DMSO and were, therefore, dissolved in EtOH to a final concentration of 40 mM. All ligands were aliquoted to prevent freeze-thaw cycles and to prevent evaporation of the orthosteric ligand solution. For both ligands, 1.7-2.5 equivalents were added to the RORγtC455H solution (11.1 mg/ml) and the mixture was incubated on ice. After 1 hour, the sample was centrifuged at 20.000 RCF for 20 minutes at 4°C to eliminate ligand and protein precipitate. All crystals were produced using a sitting drop crystallization method. MRC-2 well (Hampton Research) plates were prepared using a Mosquito pipetting robot (TTP Labtech) and stored at room temperature. Dependent on the ligand combination used, different crystallization and cryo-protection conditions were used, which are summarized in Table S6. In general, crystals grew to their final size overnight and nucleated at the bottom of the well, thereby attaching to the plastic surface. An Ultra Micro-Needle (HR4-849, Hampton Research) was used to dent the plastic right next to the crystal to release the crystal. Diffraction data of the crystals containing 20α-hydroxycholesterol were collected at the P11 beamline of the PETRA III facility at DESY (Hamburg,

Germany) while the other crystals were measured at the i03 beamline of the Diamond Light Source (Oxford, United Kingdom). All crystals were measured at 100K using a wavelength of 1 Å. Initial data processing was performed using the CCP4i2 suite (version 7.0.077).[41] DIALS was used to integrate the data and Aimless was used for scaling.[42,43] Using the RORγt crystal structure in complex with allosteric ligand FM26 (PDB: 6SAL)[29] as a search model for molecular replacement, PHASER was used to phase the data and ligand restraints were generated using AceDRG.[44,45] REFMAC and COOT were used for subsequent refinement and model building.[46,47] Final refinement was performed using phenix.refine from the Phenix software suite (version 1.16_3459).[48] For all structures, no Ramachandran outliers were observed, except for one in 6TLT. The Ramachandran statistics showed that 98-99% of the residues are in the preferred conformation and 1-2% are in the allowed conformation (Ramachandran statistics per dataset are available in Table S3-5). Figures were made with PyMOL (version 2.2.3, Schrödinger).[49]

Molecular dynamics studies. The GROMACS 2019.3 molecular dynamics package was used to perform the simulations.[50] X-ray structures of RORγt in complex with an allosteric ligand (PDB entries: 5C4O, 6SAL and 6TLM) and both the orthosteric and allosteric ligand (PDB entries: 6T4G, 6T4I, 6T4J, 6T4K, 6T4T, 6T4U, 6T4W, 6T4X, 6T4Y, 6T50, 6TLQ and 6TLT) were used. Whenever necessary, the protein was N-terminally truncated to Thr268 in order to use the same protein sequence for all simulations. The FF14SB force field was used to parameterize the protein.[51] Ligands were parameterized separately using the General AMBER force field (GAFF).[52] The complex was immersed in a cubic box with approximately 22500 TIP3P waters extending 20 Å away from the protein surface using periodic boundary conditions.[53] The system charge was neutralized using one Cl^- ion. The system was first energy minimized using the steepest descent minimization algorithm using a maximum of 50000 steps. Next, the system was progressively equilibrated by performing three heavy-atom restrained isothermal-isovolumetric (NVT) simulations for 100 ps at 100 K, 200 K and 300 K consecutively (Velocity-rescale thermostat) with a time (coupling) constant of 0.1 ns).[54] The final step of equilibration was performed for 100 ps in the isothermal-isobaric (NPT) ensemble at 300 K (Parrinello-Rahman barostat) with a time (coupling) constant of 2.0 ns.[55] During all stages, the maximum force on the protein and ligand atoms was set to 1000 kJ mol^{-1} nm^{-2} and the bonds were restrained using the LINCS algorithm.[56] The long-range electrostatics were calculated using the Particle Mesh Ewald (PME) method with a short-range cutoff of 1.0 nm and a grid spacing of 0.16 nm.[57] Five independent simulation runs of 100 ns were performed for each system with a time-step of 2 fs. Every run started from a random initial velocity distribution.

Supporting Information

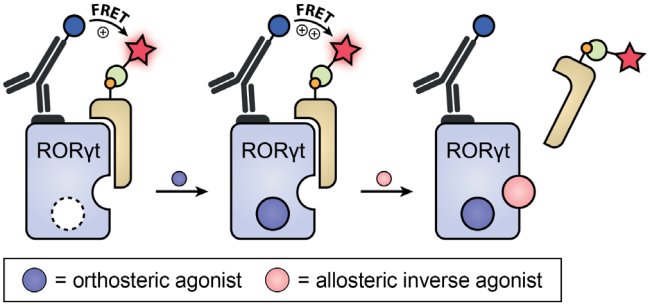

Figure S1 | Schematic representation of the TR-FRET coactivator recruitment assay. When His-RORγt is in its apo or agonist-bound state, the cofactor binds to the LBD, resulting in FRET pairing from an anti-His terbium cryptate donor to a D2-labeled streptavidin, which binds to the biotin-labeled cofactor.

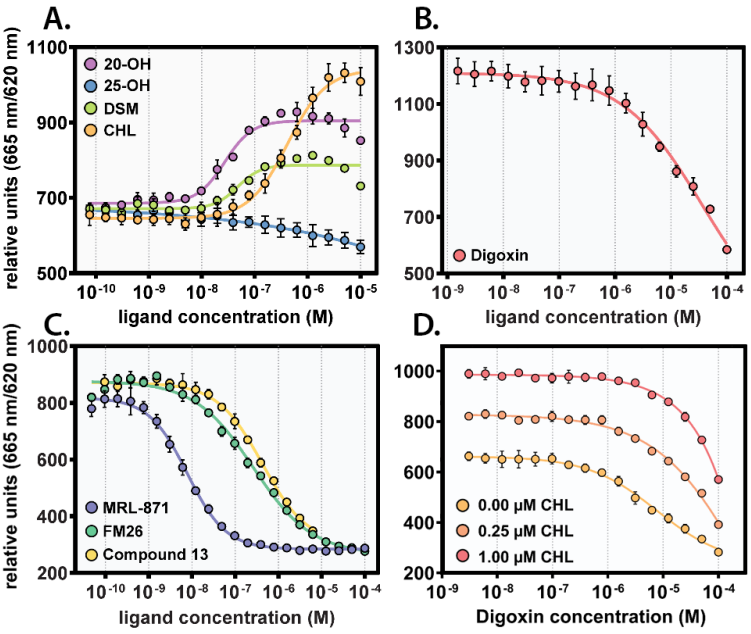

Figure S2 | Dose-response curves from the TR-FRET coactivator assay: titration of all ligands used in the manuscript to a fixed concentration of the RORγt LBD (20 nM). A. Cholesterol, desmosterol, 20α-hydroxycholesterol and 25-hydroxycholesterol (orthosteric agonists). **B.** Digoxin (orthosteric inverse agonist). **C.** MRL-871, FM26 and compound 13 (allosteric inverse agonists). **D.** Dose-response curves from the competitive TR-FRET coactivator recruitment assay with fixed concentrations of cholesterol (0.00 μM, 0.25 μM and 1.00 μM) and titration of digoxin. Data recorded in triplicate from three independent experiments (one representative dataset shown). Error bars represent the SD of the mean.

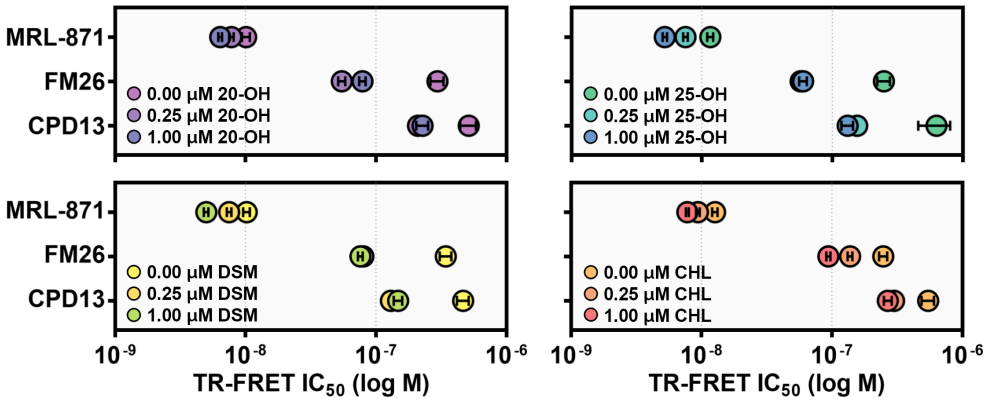

Figure S3 | Overview of the IC_{50} values for MRL-871, FM26 and compound 13 at different fixed concentrations of the orthosteric ligands. The IC_{50} values decreased as the concentration of orthosteric ligand increased.

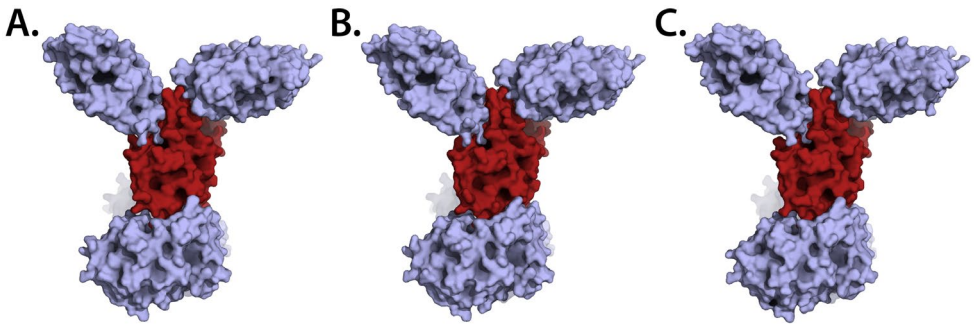

Figure S4 | Comparison of the crystal packing of RORγt using different crystallization buffers. The RORγt monomer is shown as a red surface and directly neighboring crystallographic symmetry-mates are shown in blue. **A.** 20α-hydroxycholesterol + MRL-871 without the addition of crystallization buffer **B.** 25-hydroxycholesterol + MRL-871 in 1.6M AmSO4 + 0.1M Tris (pH=8.5) **C.** desmosterol + MRL-871 in 0.2M MgCl2 + 6% PEG6000 + 0.1 M Tris (pH=8.5).

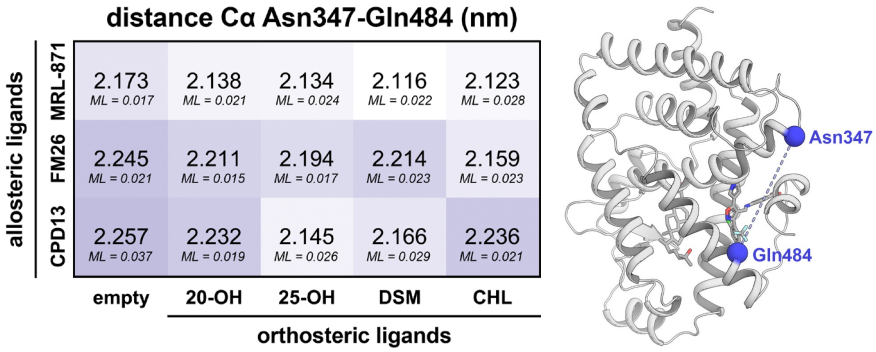

Figure S5 | Distance (in nm) between the α-carbons of Asn347 (helix 4) and Gln484 (helix 11) in the crystal structures. The maximum-likelihood coordinate error (ML; in nm) is provided for every structure. The cartoon of RORγt shows the positions of the alpha carbons of Asn347 and Gln484 as blue spheres.

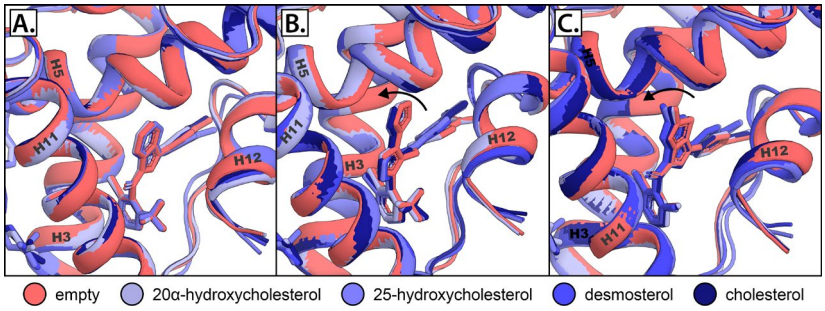

Figure S6 | Comparison of the allosteric ligand binding mode in the crystal structures in the absence (red) or presence of orthosteric ligands (blue-tones). Structural overlay of crystal structures containing **A.** MRL-871 **B.** FM26 or **C.** compound 13.

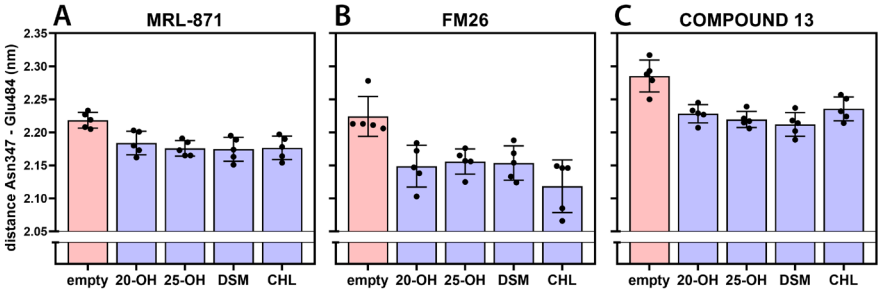

Figure S7 | Distance between the alpha carbons of Asn347 and Gln484. A-C. Bars represent the average distance between the alpha carbons of Asn347 and Gln484 (Figure S5) over five independent simulations with the individual values represented as black spheres and the error bar showing the standard deviation.

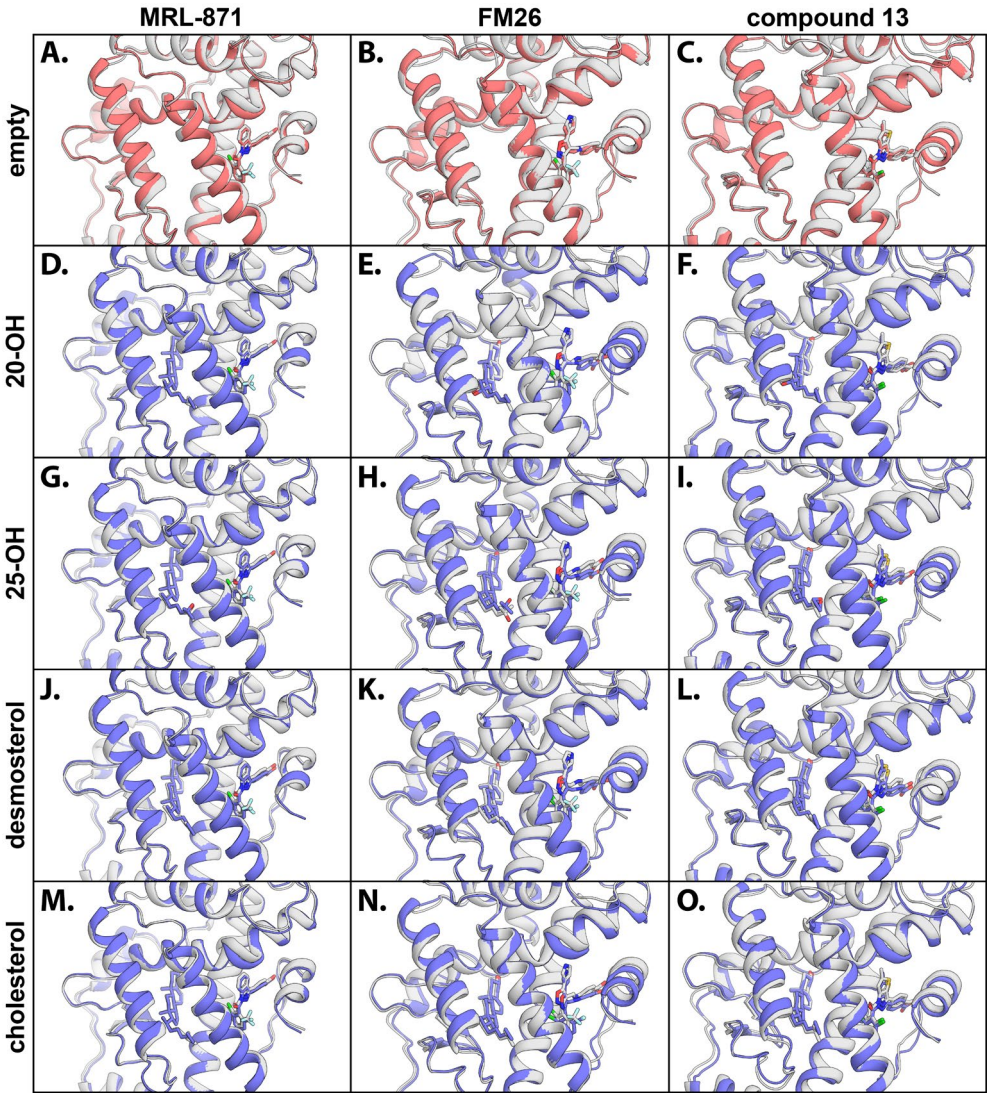

Figure S8 | Comparison of the crystal structure (white cartoon) and the average coordinates derived from the molecular dynamics simulations (red or blue cartoon). For the averaged structures, some unphysical bond lengths are present due to the averaging process. **A**-**C.** Structure comparison of the orthosteric and allosteric ligand-binding pockets from the previously published crystal structures containing only an allosteric ligand: MRL-871 (**A**), FM26 (**B**) and compound 13 (**C**). **D**-**O.** Structure comparison of the orthosteric and allosteric ligand-binding pocket of RORγt in the presence of combinations of orthosteric (20α-hydroxycholesterol (**D**-**F**), 25-hydroxycholesterol (**G**-**I**), desmosterol (**J**-**L**) and cholesterol (**M**-**O**)) and allosteric ligands (MRL-871 (**D**, **G**, **J** and **M**), FM26 (**E**, **H**, **K** and **N**) and compound 13 (**F**, **I**, **L** and **O**).

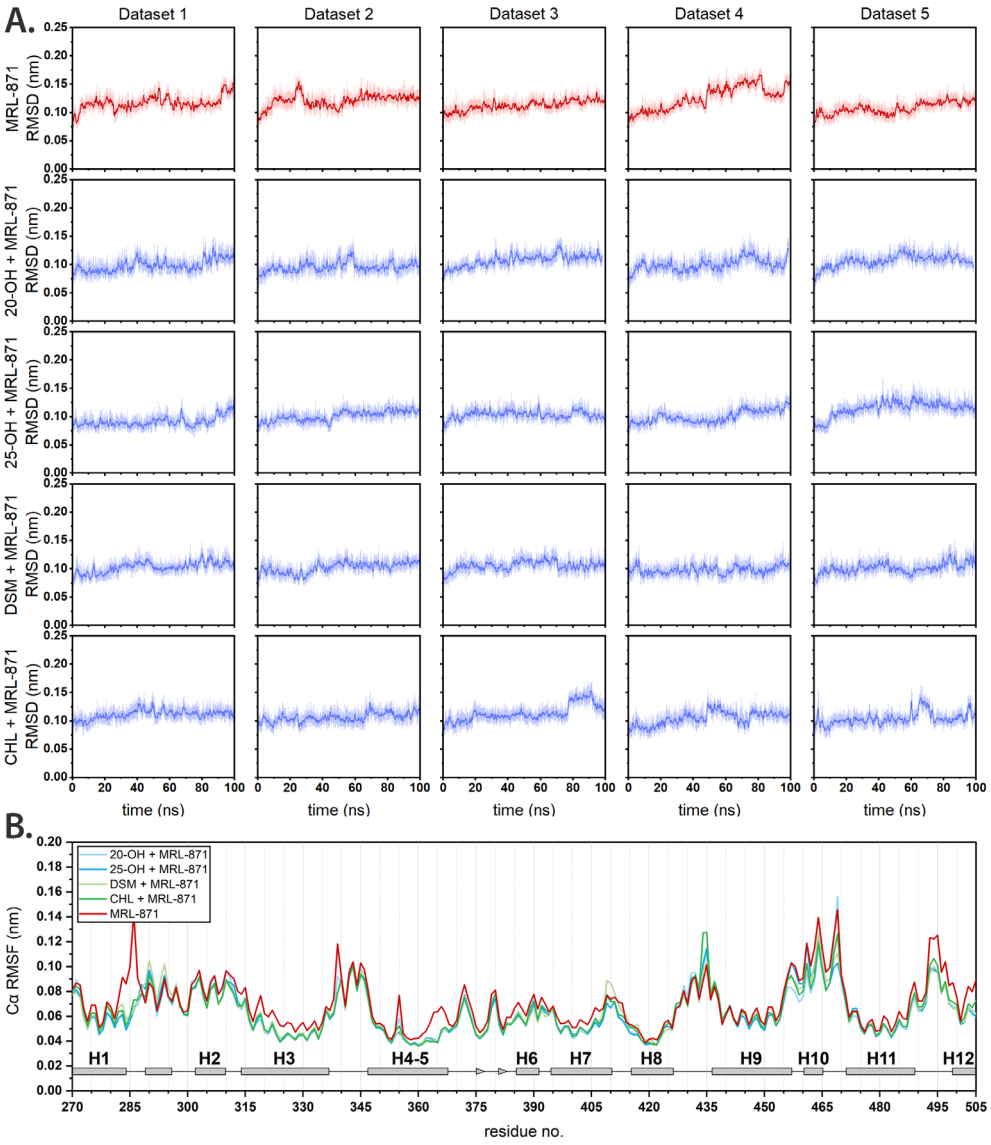

Figure S9 | A. Root mean square deviation (RMSD) of RORγt in complex with MRL-871 (red) and MRL-871 in the presence of different orthosteric modulators (blue). Data of each dataset was plotted individually using the first frame of each simulation as the reference structure. The dark line was obtained using the Savitzky-Golay smoothing method using a 100-point quadratic polynomial. **B.** Average root mean square fluctuation (RMSF) of the α-carbons of RORγt in complex with MRL-871 and different orthosteric ligands derived from five simulations per complex. The red lines show the RMSF in the absence of an orthosteric modulator. The secondary structure of the protein is represented as a rectangle, triangle and a line for α-helices, β-sheets and loops, respectively.

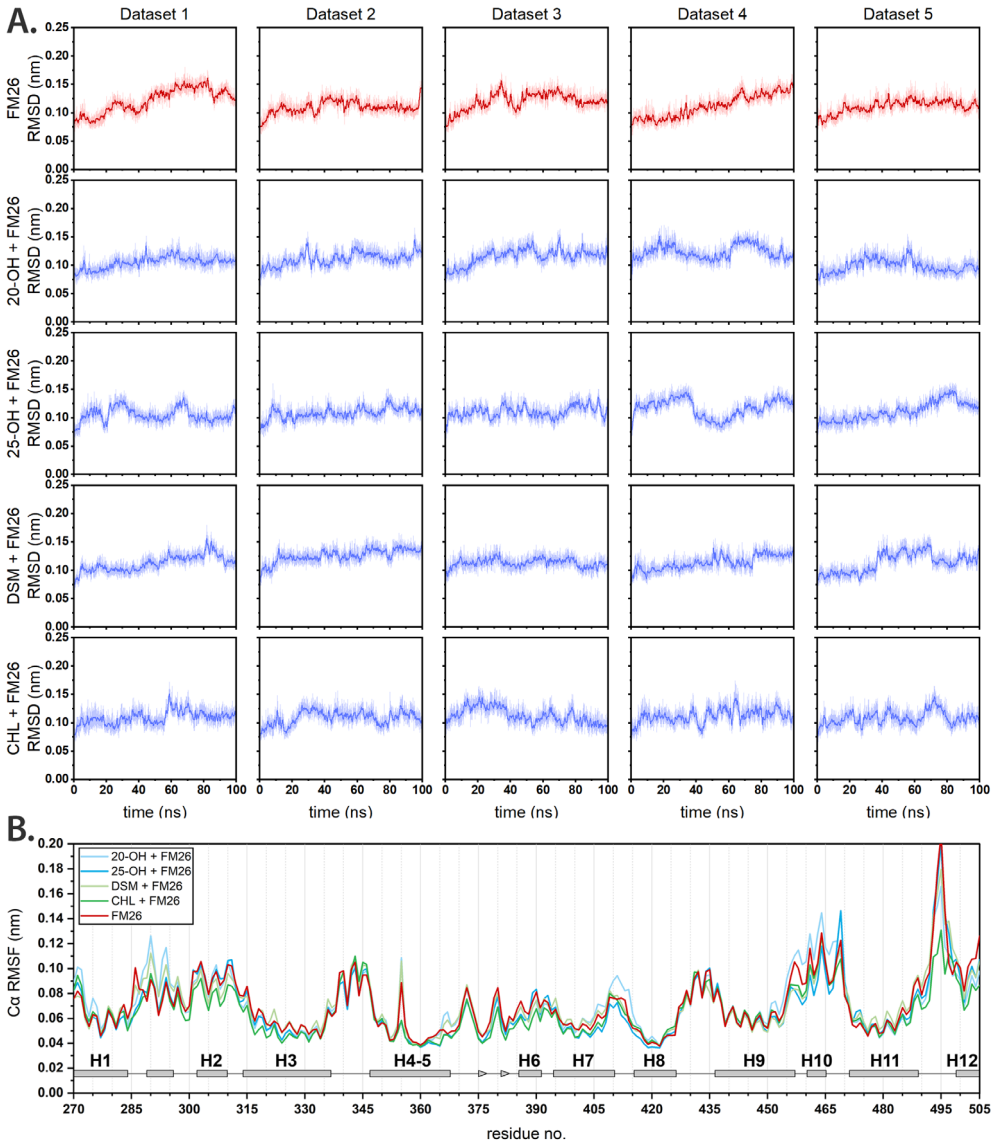

Figure S10 | A. Root mean square deviation (RMSD) of RORγt in complex with FM26 (red) and FM26 in the presence of different orthosteric modulators (blue). Data of each dataset was plotted individually using the first frame of each simulation as the reference structure. The dark line was obtained using the Savitzky-Golay smoothing method using a 100-point quadratic polynomial. **B.** Average root mean square fluctuation (RMSF) of the α-carbons of RORγt in complex with FM26 and different orthosteric ligands derived from five simulations per complex. The red lines show the RMSF in the absence of an orthosteric modulator. The secondary structure of the protein is represented as a rectangle, triangle and a line for α-helices, β-sheets and loops, respectively.

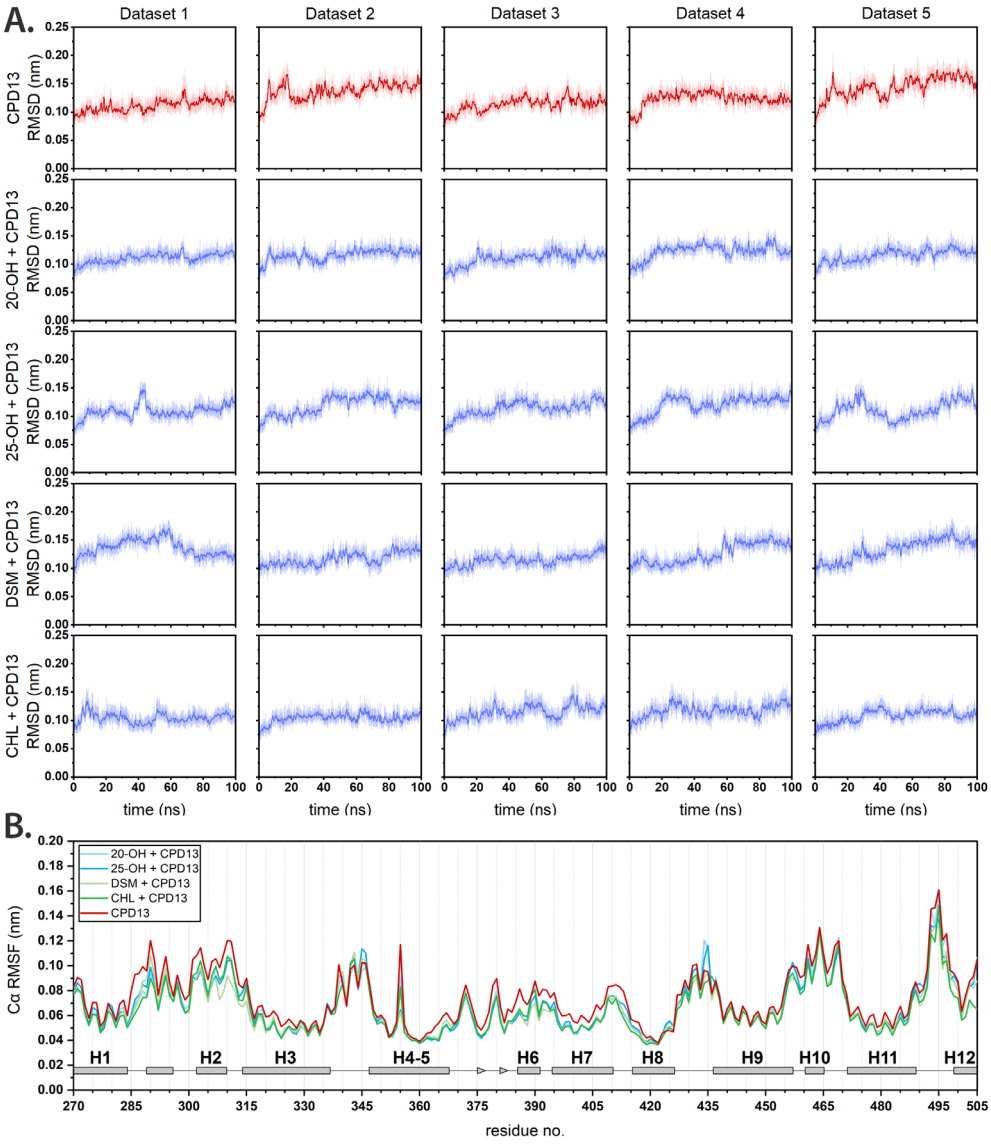

Figure S11 | A. Root mean square deviation (RMSD) of RORγt in complex with compound 13 (red) and compound 13 in the presence of different orthosteric modulators (blue). Data of each dataset was plotted individually using the first frame of each simulation as the reference structure. The dark line was obtained using the Savitzky-Golay smoothing method using a 100-point quadratic polynomial. **B.** Average root mean square fluctuation (RMSF) of the α-carbons of RORγt in complex with compound 13 and different orthosteric ligands derived from five simulations per complex. The red lines show the RMSF in the absence of an orthosteric modulator. The secondary structure of the protein is represented as a rectangle, triangle and a line for α-helices, β-sheets and loops, respectively.

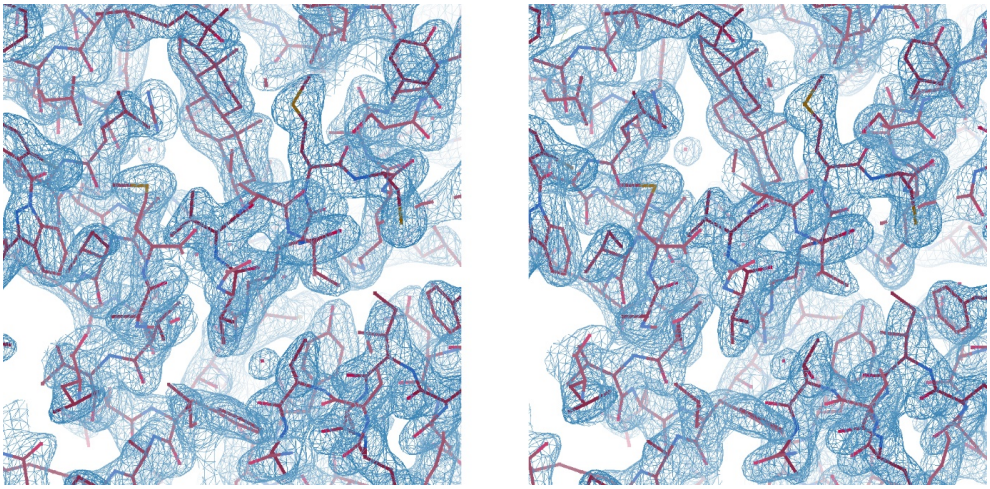

Figure S12 | Stereo image of a portion of the electron density map (2Fo-Fc) of RORγt in complex with 20α-hydroxycholesterol and MRL-871 (6T4U).

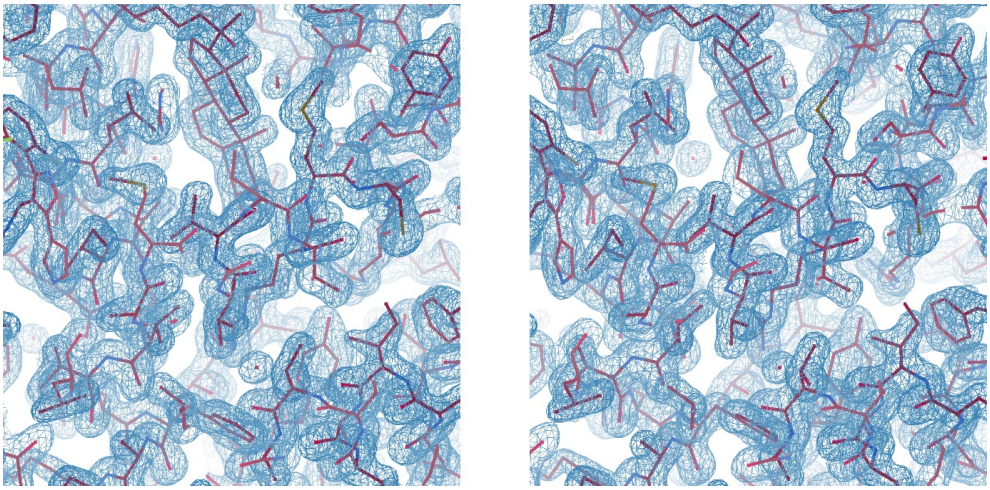

Figure S13 | Stereo image of a portion of the electron density map (2Fo-Fc) of RORγt in complex with 20α-hydroxycholesterol and FM26 (6T4T).

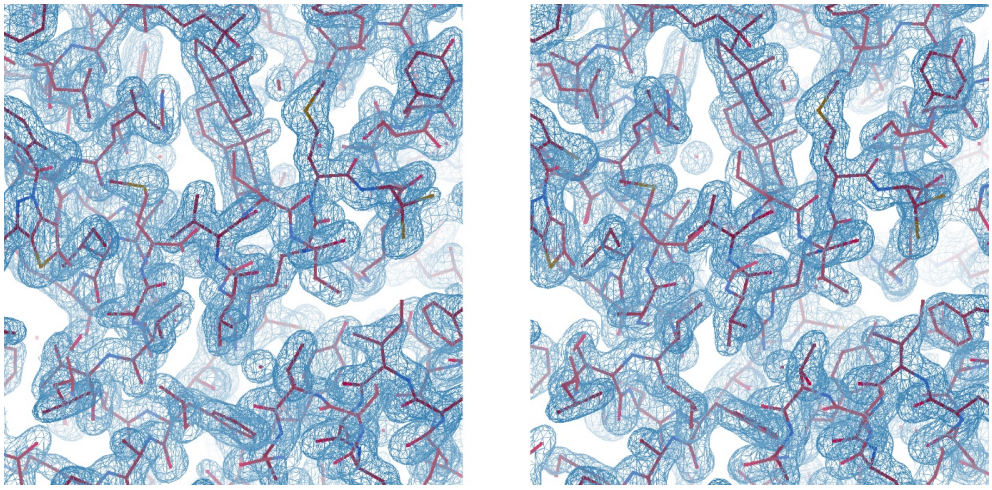

Figure S14 | Stereo image of a portion of the electron density map (2Fo-Fc) of RORγt in complex with 20α-hydroxycholesterol and compound 13 (6T4W).

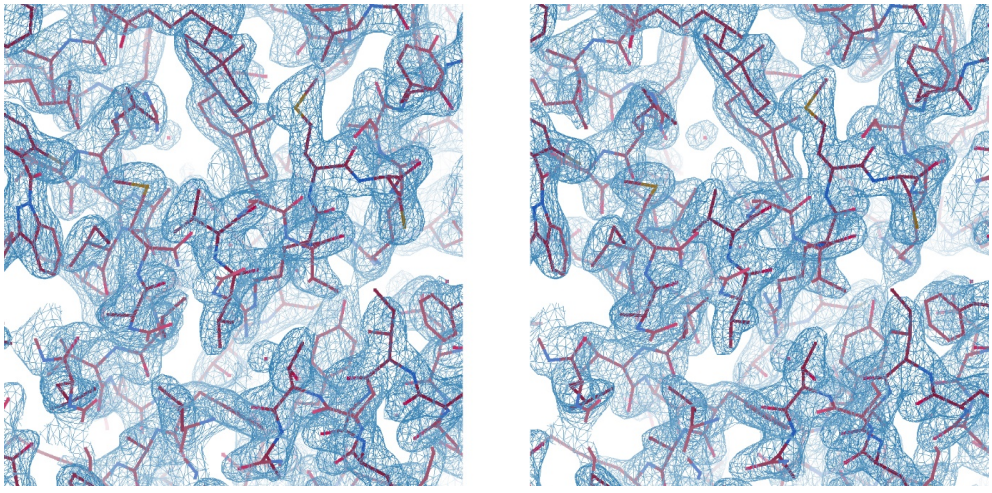

Figure S15 | Stereo image of a portion of the electron density map (2Fo-Fc) of RORγt in complex with 25-hydroxycholesterol and MRL-871 (6T4Y).

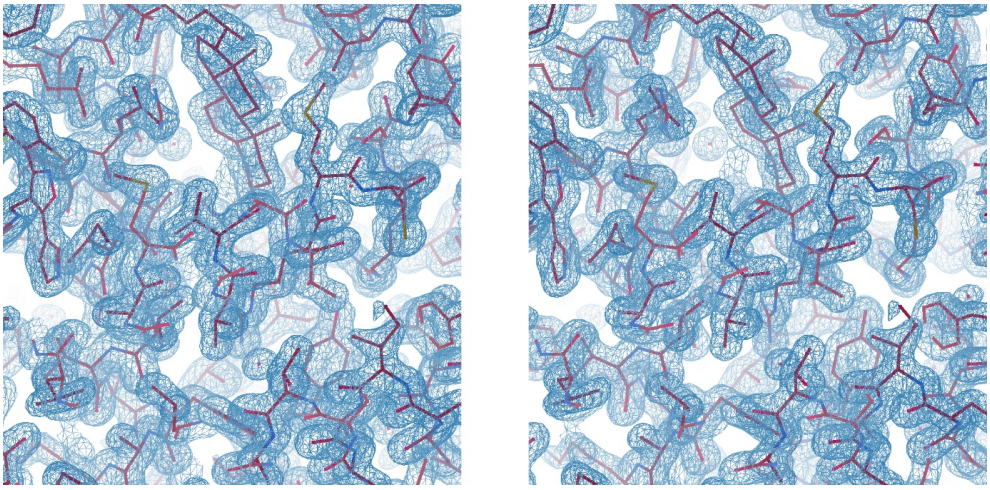

Figure S16 | Stereo image of a portion of the electron density map (2Fo-Fc) of RORγt in complex with 25-hydroxycholesterol and FM26 (6T4X).

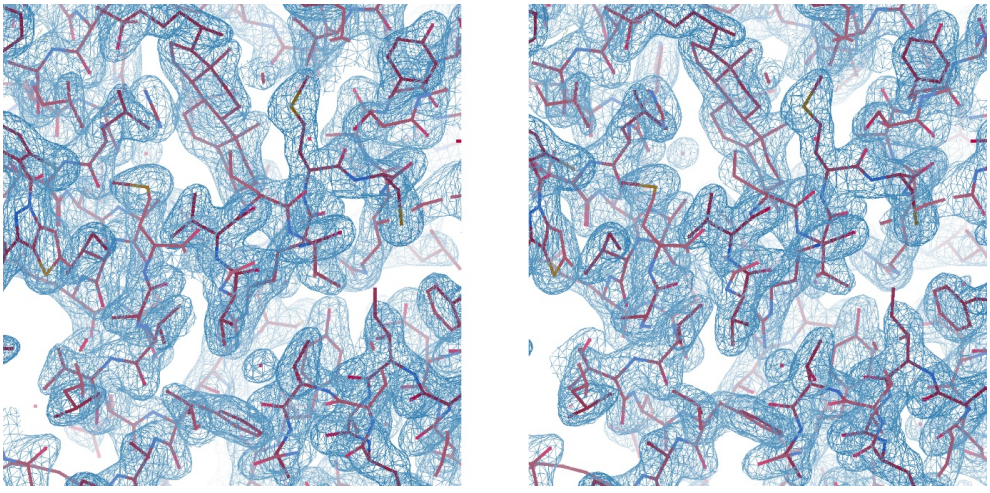

Figure S17 | Stereo image of a portion of the electron density map (2Fo-Fc) of RORγt in complex with 25-hydroxycholesterol and compound 13 (6T50).

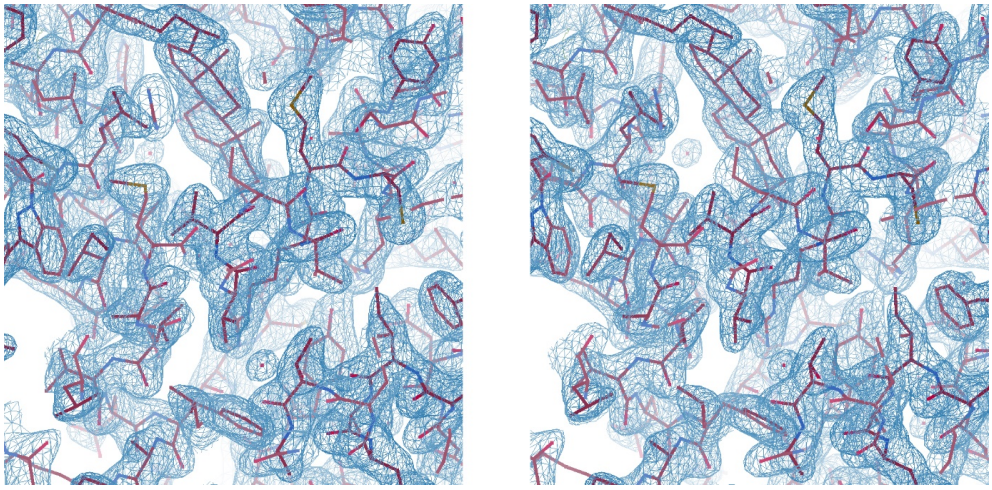

Figure S18 | Stereo image of a portion of the electron density map (2Fo-Fc) of RORγt in complex with desmosterol and MRL-871 (6T4K).

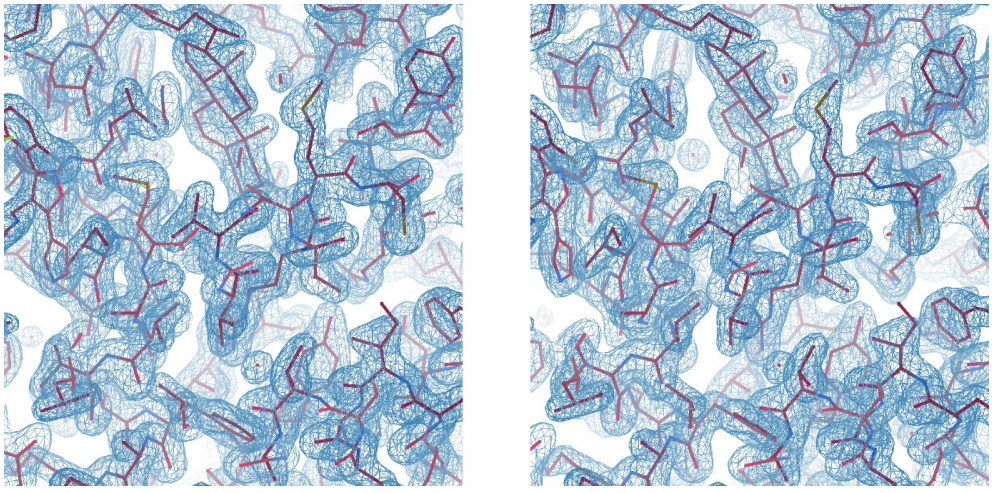

Figure S19 | Stereo image of a portion of the electron density map (2Fo-Fc) of RORγt in complex with desmosterol and FM26 (6T4J).

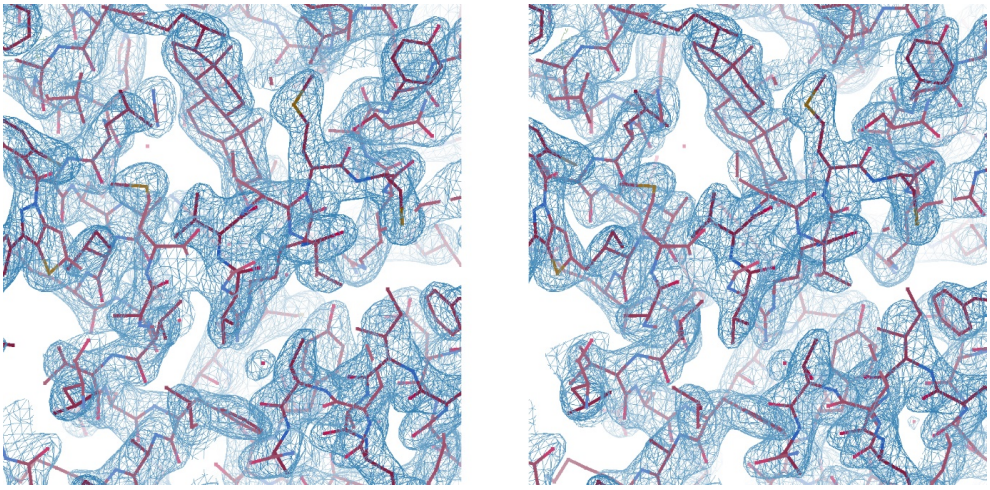

Figure S20 | Stereo image of a portion of the electron density map (2Fo-Fc) of RORγt in complex with desmosterol and compound 13 (6TLT).

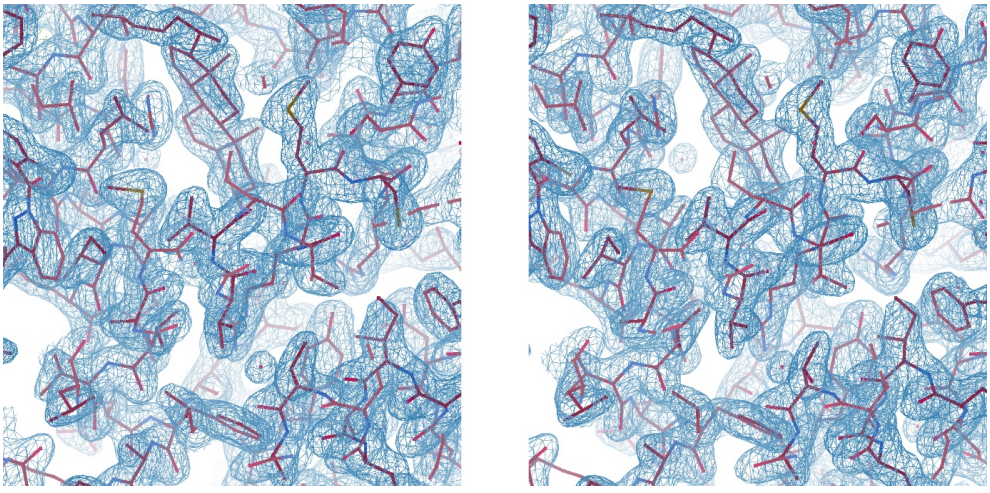

Figure S21 | Stereo image of a portion of the electron density map (2Fo-Fc) of RORγt in complex with cholesterol and MRL-871 (6T4I).

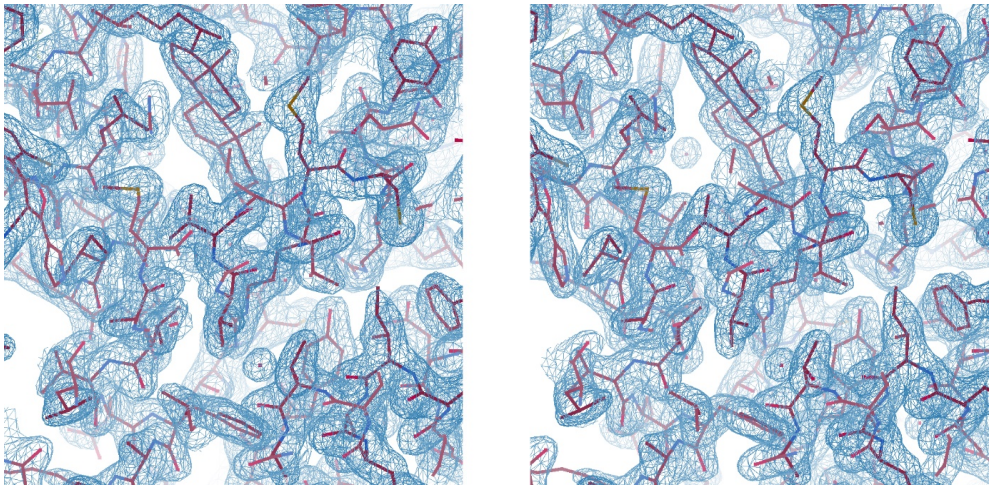

Figure S22 | Stereo image of a portion of the electron density map (2Fo-Fc) of RORγt in complex with cholesterol and FM26 (6T4G).

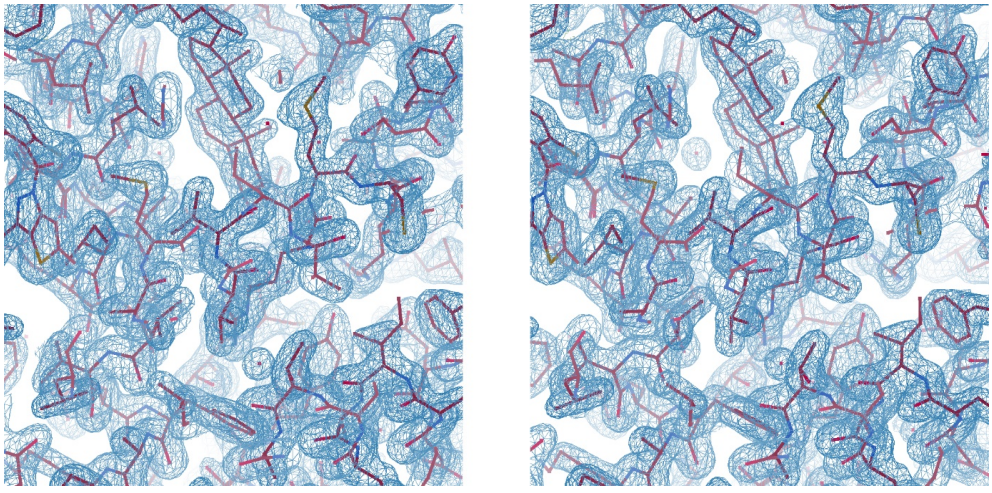

Figure S23 | Stereo image of a portion of the electron density map (2Fo-Fc) of RORγt in complex with cholesterol and compound 13 (6TLQ).

Table S1 | EC_{50} & IC_{50} values for all compounds, determined in TR-FRET coactivator assays (from Figure S1).

Compounds	EC_{50}/IC_{50} (nM)
20α-hydroxycholesterol	24.0 ± 2.8
25-hydroxycholesterol	ambiguously*
desmosterol	43.0 ± 7.3
cholesterol	416.3 ± 40.6
digoxin	15090 ± 1300
MRL-871	7.8 ± 0.5
FM26	264.1 ± 22.7
compound 13	424.9 ± 60.6

* Acts as a partial inverse agonist, flattening the binding curve.

Table S2 | IC_{50} and Hill slope values from the competitive TR-FRET coactivator recruitment assay with fixed concentrations of orthosteric ligands. Abbreviations: 20α-hydroxycholesterol (20OH), 25-hydroxycholesterol (25OH), desmosterol (DSM), cholesterol (CHL) and compound 13 (CPD13).

orthosteric ligand	allosteric ligand						
	MRL-871		FM26		compound 13		
conc. (μM)	IC_{50} (nM)	Hill slope	IC_{50} (nM)	Hill slope	IC_{50} (nM)	Hill slope	
0	10.1 ± 0.7	-0.95 ± 0.06	296 ± 34	-0.60 ± 0.04	514 ± 72	-1.10 ± 0.13	20-OH
0.25	7.8 ± 0.3	-1.34 ± 0.07	55 ± 3	-1.13 ± 0.07	210 ± 19	-1.34 ± 0.14	
1	6.4 ± 0.2	-1.30 ± 0.05	79 ± 4	-1.23 ± 0.07	228 ± 24	-1.13 ± 0.11	
0	11.6 ± 0.6	-0.98 ± 0.04	249 ± 28	-0.65 ± 0.04	629 ± 173	-0.84 ± 0.12	25-OH
0.25	7.5 ± 0.3	-1.37 ± 0.06	57 ± 2	-1.03 ± 0.04	155 ± 12	-1.16 ± 0.09	
1	5.2 ± 0.2	-1.36 ± 0.06	60 ± 4	-1.02 ± 0.06	131 ± 13	-1.09 ± 0.11	
0	10.2 ± 0.6	-0.93 ± 0.04	343 ± 35	-0.70 ± 0.05	466 ± 49	-0.98 ± 0.08	DSM
0.25	7.5 ± 0.3	-1.13 ± 0.04	80 ± 4	-0.86 ± 0.04	130 ± 9	-1.06 ± 0.07	
1	5.0 ± 0.2	-1.05 ± 0.04	76 ± 4	-1.02 ± 0.04	148 ± 11	-1.21 ± 0.10	
0	12.7 ± 0.6	-0.97 ± 0.04	248 ± 18	-0.77 ± 0.04	547 ± 60	-0.74 ± 0.06	CHL
0.25	9.4 ± 0.3	-1.04 ± 0.03	138 ± 6	-0.86 ± 0.03	300 ± 18	-0.87 ± 0.04	
1	7.8 ± 0.2	-1.20 ± 0.03	94 ± 3	-1.01 ± 0.03	269 ± 19	-0.90 ± 0.05	

orthosteric ligand

cholesterol conc. (μM)	digoxin IC_{50} (nM)
0	7012 ± 588
0.25	33620 ± 1694
1	85400 ± 4276

Table S3 | Data collection and refinement statistics for RORγt in complex with both an orthosteric and an allosteric ligand. Abbreviations: 20α-hydroxycholesterol (20-OH), 25-hydroxycholesterol (25-OH) and compound 13 (CPD13).

RORγt in complex with:	*20-OH + MRL-871*	*20-OH + FM26*	*20-OH + CPD13*	*25-OH + MRL-871*
Data collection				
Space group	P 6_1 2 2	P 6_1 2 2	P 6_1 2 2	P 6_1 2 2
Cell dimensions				
a, b, c (Å)	108.52 108.52 105.94	108.50 108.50 99.29	108.32 108.32 99.33	108.64 108.64 107.67
α, β, γ (°)	90 90 120	90 90 120	90 90 120	90 90 120
Resolution (Å)	54.26-2.00 (2.07-2.00)	54.25-1.62 (1.68- 1.62)	54.16-1.71 (1.77-1.71)	93.97-1.95 (2.02-1.95)
I/σ(I)	10.13 (0.27)	23.04 (2.69)	31.00 (0.88)	28.39 (1.63)
Completeness (%)	97.86 (82.70)	99.60 (96.99)	99.86 (99.62)	99.97 (100.00)
Redundancy	27.6 (8.2)	137.1 (73.2)	37.4 (37.3)	38.9 (38.0)
$CC_{1/2}$	0.985 (0.551)	1.000 (0.977)	0.991 (0.219)	1.000 (0.741)
Refinement				
No. unique reflections	24921 (2070)	44254 (4235)	37646 (3706)	27179 (2667)
Rwork/Rfree	0.1923/0.2282	0.1478/0.1887	0.1596/0.2000	0.186/0.215
No. atoms (non-H)				
Protein	1978	2053	2016	2040
Ligand	66	73	69	66
Water	64	198	176	47
Average B-factors				
Protein	56.31	29.44	34.44	61.26
Ligand	46.63	26.11	31.76	50.67
Water	54.58	42.05	45.48	57.05
R.m.s. deviations				
Bond lengths (Å)	0.007	0.024	0.013	0.014
Bond angles (°)	0.820	1.850	1.820	1.710
Ramachandran				
Favored/allowed (%)	97.9/2.1	98.8/1.2	99.2/0.8	98.8/1.2
Outliers (%)	0.0	0.0	0.0	0.0
PDB ID	6T4U	6T4T	6T4W	6T4Y

Table S4 | Data collection and refinement statistics for RORγt in complex with both an orthosteric and an allosteric ligand. Abbreviations: 25-hydroxycholesterol (25-OH), desmosterol (DSM) and compound 13 (CPD13).

RORγt in complex with:	*25-OH + FM26*	*25-OH + CPD13*	*DSM + MRL-871*	*DSM + FM26*
Data collection				
Space group	P 6_1 2 2	P 6_1 2 2	P 6_1 2 2	P 6_1 2 2
Cell dimensions				
a, b, c (Å)	108.88 108.88 98.54	108.33 108.33 108.51	108.32 108.32 108.52	108.91 108.91 98.48
α, β, γ (°)	90 90 120	90 90 120	90, 90, 120	90 90 120
Resolution (Å)	94.29-1.48 (1.53-1.48)	48.46-1.87 (1.94-1.87)	48.46-1.89 (1.95-1.89)	47.66-1.79 (1.85-1.79)
I/σ(I)	25.51 (1.87)	35.83 (1.61)	35.74 (1.67)	22.70 (1.82)
Completeness (%)	99.99 (100.00)	99.96 (100.00)	99.97 (99.97)	99.98 (100.00)
Redundancy	39.1 (39.5)	39.1 (39.4)	39.1 (40.4)	39.0 (40.1)
$CC_{1/2}$	1.000 (0.757)	1.000 (0.799)	1.000 (0.777)	1.000 (0.689)
Refinement				
No. unique reflections	30639 (2992)	31584 (3088)	30639 (2992)	32984 (3222)
Rwork/Rfree	0.1749/0.1852	0.1857/0.2108	0.1847/0.2055	0.175/0.197
No. atoms (non-H)				
Protein	2055	2040	2175	2046
Ligand	73	63	71	66
Water	255	241	71	186
Average B-factors				
Protein	28.79	55.11	59.92	36.46
Ligand	24.03	42.73	52.19	32.77
Water	42.38	53.75	56.28	48.35
R.m.s. deviations				
Bond lengths (Å)	0.017	0.015	0.014	0.009
Bond angles (°)	1.790	1.780	1.760	1.190
Ramachandran				
Favored/allowed (%)	99.2/0.8	98.0/2.0	98.4/1.6	98.8/1.2
Outliers (%)	0.0	0.0	0.0	0.0
PDB ID	6T4X	6T50	6T4K	6T4J

Table S5 | Data collection and refinement statistics for RORγt in complex with both an orthosteric and an allosteric ligand. Abbreviations: desmosterol (DSM), cholesterol (CHL) and compound 13 (CPD13).

RORγt in complex with:	*DSM + CPD13*	*CHL + MRL-871*	*CHL + FM26*	*CHL + CPD13*
Data collection				
Space group	P 6_1 2 2	P 6_1 2 2	P 6_1 2 2	P 6_1 2 2
Cell dimensions				
a, b, c (Å)	108.73 108.73 104.73	107.96 107.96 107.42	108.51 108.51 105.04	108.86 108.86 98.64
α, β, γ (°)	90 90 120	90 90 120	90 90 120	90 90 120
Resolution (Å)	94.16-2.11 (2.16-2.10)	46.75-1.84 (1.91-1.84)	48.5-1.93 (2.00-1.93)	98.64-1.75 (1.78-1.75)
I/σ(I)	10.2 (0.5)	29.39 (1.15)	27.97 (1.81)	8.7 (0.5)
Completeness (%)	99.4 (92.0)	98.75 (92.59)	99.97 (99.96)	100.0 (99.8)
Redundancy	37.6 (38.8)	32.8 (13.7)	39.0 (40.0)	37.3 (35.7)
$CC_{1/2}$	0.999 (0.414)	1.000 (0.527)	1.000 (0.848)	0.998 (0.297)
Refinement				
No. unique reflections	21797 (1611)	32217 (2967)	28750 (2806)	35249 (1900)
Rwork/Rfree	0.196/0.235	0.191/0.214	0.178/0.213	0.178/0.212
No. atoms (non-H)				
Protein	2005	2053	2030	2042
Ligand	62	65	66	74
Water	17	113	105	181
Average B-factors				
Protein	66.01	52.32	52.30	35.61
Ligand	58.22	45.29	45.89	39.38
Water	56.45	54.27	53.92	46.39
R.m.s. deviations				
Bond lengths (Å)	0.016	0.015	0.016	0.017
Bond angles (°)	2.100	1.940	1.890	1.930
Ramachandran				
Favored/allowed (%)	98.4/1.2	99.2/0.8	99.2/0.8	98.8/1.2
Outliers (%)	0.4	0.0	0.0	0.0
PDB ID	6TLT	6T4I	6T4G	6TLQ

Table S6 | Overview of the crystallization conditions of RORγt. Abbreviations: 20α-hydroxycholesterol (20-OH), 25-hydroxycholesterol (25-OH), desmosterol (DSM), cholesterol (CHL) and compound 13 (CPD13).

Ligands	Crystallization Buffer	P:B* (nl)	Cryoprotection
20-OH + MRL-871	Empty**	-	1.6M $AmSO_4$ + 0.1M Tris + 25 % glycerol (pH=8.5)
20-OH + FM26	Empty**	-	1.6M $AmSO_4$ + 0.1M Tris + 25 % glycerol (pH=8.5)
20-OH + CPD13	Empty**	-	1.6M $AmSO_4$ + 0.1M Tris + 25 % glycerol (pH=8.5)
25-OH + MRL-871	1.6M $AmSO_4$ + 0.1M Tris (pH=8.5)	800 : 400	1.6M $AmSO_4$ + 0.1M Tris + 25 % glycerol + 200 µM MRL-871 (pH=8.5)
25-OH + FM26	1.6M $AmSO_4$ + 0.1M Tris (pH=8.5)	800 : 400	1.6M $AmSO_4$ + 0.1M Tris + 25 % glycerol + 200 µM FM26 (pH=8.5)
25-OH + CPD13	0.2M $MgCl_2$ + 6% PEG6000 + 0.1M Tris (pH=8.5)	800 : 400	0.2M $MgCl_2$ + 6% PEG6000 + 0.1M Tris + 200µM CPD13 (pH=8.5)
DSM + MRL-871	0.2M $MgCl_2$ + 6% PEG6000 + 0.1M Tris (pH=8.5)	900 : 300	0.2M $MgCl_2$ + 6% PEG6000 + 0.1M Tris + 200µM MRL-871 (pH=8.5)
DSM + FM26	1.2M $AmSO_4$ + 0.1M Tris (pH=8.5)	900 : 300	1.6M $AmSO_4$ + 0.1M Tris + 25 % glycerol + 200 µM CPD13 (pH=8.5)
DSM + CPD13	1.6M $AmSO_4$ + 0.1M Tris (pH=8.5)	800 : 400	1.6M $AmSO_4$ + 0.1M Tris + 25 % glycerol + 200 µM FM26 (pH=8.5)
CHL + MRL-871	0.2M $MgCl_2$ + 6% PEG6000 + 0.1M Tris (pH=8.5)	800 : 400	0.2M $MgCl_2$ + 6% PEG6000 + 0.1M Tris + 200µM MRL-871 (pH=8.5)
CHL + FM26	1.2M $AmSO_4$ + 0.1M Tris (pH=8.5)	800 : 400	1.6M $AmSO_4$ + 0.1M Tris + 25 % glycerol + 200 µM FM26 (pH=8.5)
CHL + CPD13	1.6M $AmSO_4$ + 0.1M Tris (pH=8.5)	800 : 400	1.6M $AmSO_4$ + 0.1M Tris + 25 % glycerol + 200 µM CPD13 (pH=8.5)

* Crystallization drop composition, protein-ligand solution volume (P) : crystallization buffer volume (B)
** The protein ligand solution was evaporated using an empty buffer well

Acknowledgements

Femke A. Meijer, Richard G. Doveston and Iris A. Leijten-van de Gevel are greatly acknowledged for the valuable discussions and contributions to this work. The tutors of the DLS-CCP4 Data Collection and Structure Solution Workshop 2017 at the Diamond Light Source (Oxfordshire, UK) are greatly acknowledged.

References

1. Meijer, F. A., Leijten-van de Gevel, I. A., de Vries, R. M. J. M. & Brunsveld, L. Allosteric small molecule modulators of nuclear receptors. *Mol. Cell. Endocrinol.* **485**, 20–34 (2019).
2. Changeux, J. P. & Christopoulos, A. Allosteric Modulation as a Unifying Mechanism for Receptor Function and Regulation. *Cell* vol. 166 1084–1102 (2016).
3. van Westen, G. J. P., Gaulton, A. & Overington, J. P. Chemical, Target, and Bioactive Properties of Allosteric Modulation. *PLoS Comput. Biol.* **10**, (2014).

4. Thal, D. M., Glukhova, A., Sexton, P. M. & Christopoulos, A. Structural insights into G-protein-coupled receptor allostery. *Nature* **559**, 45–53 (2018).
5. Lewis, J. A., Lebois, E. P. & Lindsley, C. W. Allosteric modulation of kinases and GPCRs: design principles and structural diversity. *Curr. Opin. Chem. Biol.* **12**, 269–280 (2008).
6. Wu, P., Clausen, M. H. & Nielsen, T. E. Allosteric small-molecule kinase inhibitors. *Pharmacol. Ther.* **156**, 59–68 (2015).
7. Jacobsen, S. E., Gether, U. & Bräuner-Osborne, H. Investigating the molecular mechanism of positive and negative allosteric modulators in the calcium-sensing receptor dimer. *Sci. Rep.* **7**, 46355 (2017).
8. Capdeville, R., Buchdunger, E., Zimmermann, J. & Matter, A. Glivec (STI571, imatinib), a rationally developed, targeted anticancer drug. *Nat. Rev. Drug Discov.* **1**, 493–502 (2002).
9. Whitty, A. Cooperativity and biological complexity. *Nat. Chem. Biol.* **4**, 435–439 (2008).
10. Stefan, M. I. & Le Novère, N. Cooperative Binding. *PLOS Comput. Biol.* **9**, e1003106 (2013).
11. Cattoni, D. I., Chara, O., Kaufman, S. B. & González Flecha, F. L. Cooperativity in Binding Processes: New Insights from Phenomenological Modeling. *PLoS One* **10**, e0146043–e0146043 (2015).
12. Wootten, D., Christopoulos, A. & Sexton, P. M. Emerging paradigms in GPCR allostery: Implications for drug discovery. *Nat. Rev. Drug Discov.* **12**, 630–644 (2013).
13. Lu, J. *et al.* Structural basis for the cooperative allosteric activation of the free fatty acid receptor GPR40. *Nat. Struct. Mol. Biol.* **24**, 570–577 (2017).
14. Cui, Q. & Karplus, M. Allostery and cooperativity revisited. *Protein Sci.* **17**, 1295–1307 (2008).
15. Shang, J. *et al.* Cooperative cobinding of synthetic and natural ligands to the nuclear receptor PPARγ. *Elife* **7**, (2018).
16. Putcha, B.-D. K., Wright, E., Brunzelle, J. S. & Fernandez, E. J. Structural basis for negative cooperativity within agonist-bound TR:RXR heterodimers. *Proc. Natl. Acad. Sci.* **109**, 6084 LP – 6087 (2012).
17. Darimont, B. D. *et al.* Structure and specificity of nuclear receptor-coactivator interactions. *Genes Dev.* **12**, 3343–3356 (1998).
18. Santos, R. *et al.* A comprehensive map of molecular drug targets. *Nat. Rev. Drug Discov.* **16**, 19–34 (2016).
19. Ivanov, I. I. *et al.* The Orphan Nuclear Receptor RORγt Directs the Differentiation Program of Proinflammatory IL-17+T Helper Cells. *Cell* **126**, 1121–1133 (2006).
20. Fauber, B. P. & Magnuson, S. Modulators of the nuclear receptor retinoic acid receptor-related orphan receptor-γ (RORγ or RORc). *Journal of Medicinal Chemistry* vol. 57 5871–5892 (2014).
21. Solt, L. A. & Burris, T. P. Action of RORs and their ligands in (patho)physiology. *Trends Endocrinol. Metab.* **23**, 619–627 (2012).
22. Bronner, S. M., Zbieg, J. R. & Crawford, J. J. RORγ antagonists and inverse agonists: a patent review. *Expert Opin. Ther. Pat.* **27**, 101–112 (2017).
23. Pandya, V. B., Kumar, S., Sachchidanand, Sharma, R. & Desai, R. C. Combating Autoimmune Diseases With Retinoic Acid Receptor-Related Orphan Receptor-γ (RORγ or RORc) Inhibitors: Hits and Misses. *J. Med. Chem.* **61**, 10976–10995 (2018).
24. Cyr, P., Bronner, S. M. & Crawford, J. J. Recent progress on nuclear receptor RORγ modulators. *Bioorganic Med. Chem. Lett.* **26**, 4387–4393 (2016).
25. Hu, X. *et al.* Sterol metabolism controls TH17 differentiation by generating endogenous RORγ agonists. *Nat. Chem. Biol.* **11**, 141–147 (2015).
26. Kumar, N. *et al.* The benzenesulfoamide T0901317 [N-(2,2,2-trifluoroethyl)-N-[4-[2,2,2-trifluoro-1-hydroxy-1-(trifluoromethyl)ethy l]phenyl]-benzenesulfonamide] is a novel retinoic acid receptor-related orphan receptor-alpha/gamma inverse agonist. *Mol. Pharmacol.* **77**, 228–236 (2010).
27. Karstens, W. F. J. et al W. F. J. *et al.* RORgammat inhibitors. *PCT Int. Appl.* (2012).
28. Scheepstra, M. *et al.* Identification of an allosteric binding site for RORγt inhibition. *Nat. Commun.* **6**, 1–10 (2015).

29. Meijer, F. A. *et al.* Ligand-Based Design of Allosteric Retinoic Acid Receptor-Related Orphan Receptor γt (RORγt) Inverse Agonists. *J. Med. Chem.* **63**, 241–259 (2020).
30. Chaudari, S. S. *et al.* Bicyclic Heterocyclic compounds as ROR Gamma Modulators. WO2015008234 (2015).
31. de Vries, R. M. J. M., Meijer, F. A., Doveston, R. G. & Brunsveld, L. Elucidation of an allosteric mode-of-action for a thienopyrazole RORγt inverse agonist. *ChemMedChem* **n/a**, (2020).
32. Jin, L. *et al.* Structural Basis for Hydroxycholesterols as Natural Ligands of Orphan Nuclear Receptor RORγ. *Mol. Endocrinol.* **24**, 923–929 (2010).
33. Huh, J. R. *et al.* Digoxin and its derivatives suppress TH17 cell differentiation by antagonizing RORγt activity. *Nature* **472**, 486–490 (2011).
34. Gege, C. Retinoid-related orphan receptor γ t modulators: comparison of Glenmark's me-too patent application (WO2015008234) with the originator application from Merck Sharp and Dohme (WO2012106995). *Expert Opin. Ther. Pat.* **25**, 1215–1221 (2015).
35. DeSantis, K. A. & Reinking, J. L. Use of Differential Scanning Fluorimetry to Identify Nuclear Receptor Ligands. *Methods Mol. Biol.* **1443**, 21–30 (2016).
36. Niesen, F. H., Berglund, H. & Vedadi, M. The use of differential scanning fluorimetry to detect ligand interactions that promote protein stability. *Nat. Protoc.* **2**, 2212–2221 (2007).
37. Gao, K., Oerlemans, R. & Groves, M. R. Theory and applications of differential scanning fluorimetry in early-stage drug discovery. *Biophys. Rev.* **12**, 85–104 (2020).
38. Degorce, F. HTRF: A Technology Tailored for Drug Discovery - A Review of Theoretical Aspects and Recent Applications. *Curr. Chem. Genomics* **3**, 22–32 (2009).
39. Kojetin, D. J. *et al.* Structural mechanism for signal transduction in RXR nuclear receptor heterodimers. *Nat. Commun.* **6**, 8013 (2015).
40. Leijten-van de Gevel, I. A. & Brunsveld, L. Delineation of the molecular determinants of the unique allosteric binding site of the orphan nuclear receptor RORγt. *J. Biol. Chem.* jbc.RA120.013581 (2020) doi:10.1074/jbc.ra120.013581.
41. Potterton, L. *et al.* CCP4i2: the new graphical user interface to the CCP4 program suite. *Acta Crystallogr. Sect. D Struct. Biol.* **74**, 68–84 (2018).
42. Clabbers, M. T. B. *et al.* Electron diffraction data processing with *DIALS*. *Acta Crystallogr. Sect. D Struct. Biol.* **74**, 506–518 (2018).
43. Evans, P. R. & Murshudov, G. N. How good are my data and what is the resolution? *Acta Crystallogr. Sect. D Biol. Crystallogr.* **69**, 1204–1214 (2013).
44. McCoy, A. J. Solving structures of protein complexes by molecular replacement with Phaser. *Acta Crystallogr. D. Biol. Crystallogr.* **63**, 32–41 (2007).
45. Long, F. *et al. AceDRG*: a stereochemical description generator for ligands. *Acta Crystallogr. Sect. D Struct. Biol.* **73**, 112–122 (2017).
46. Murshudov, G. N. *et al.* REFMAC5 for the refinement of macromolecular crystal structures. *Acta Crystallogr. D. Biol. Crystallogr.* **67**, 355–67 (2011).
47. Emsley, P., Lohkamp, B., Scott, W. G. & Cowtan, K. Features and development of *Coot*. *Acta Crystallogr. Sect. D Biol. Crystallogr.* **66**, 486–501 (2010).
48. Afonine, P. V. *et al.* Towards automated crystallographic structure refinement with phenix.refine. *Acta Crystallogr. Sect. D Biol. Crystallogr.* **68**, 352–367 (2012).
49. Schrodinger LLC. *The PyMOL Molecular Graphics System, Version 2.2.3*. (Schrödinger LLC, 2015).
50. Abraham, M. J. *et al.* Gromacs: High performance molecular simulations through multi-level parallelism from laptops to supercomputers. *SoftwareX* **1–2**, 19–25 (2015).
51. Maier, J. A. *et al.* ff14SB: Improving the Accuracy of Protein Side Chain and Backbone Parameters from ff99SB. *J. Chem. Theory Comput.* **11**, 3696–3713 (2015).
52. Wang, J., Wolf, R. M., Caldwell, J. W., Kollman, P. A. & Case, D. A. Development and testing of a general Amber force field. *J. Comput. Chem.* **25**, 1157–1174 (2004).

53. Jorgensen, W. L., Chandrasekhar, J., Madura, J. D., Impey, R. W. & Klein, M. L. Comparison of simple potential functions for simulating liquid water. *J. Chem. Phys.* **79**, 926–935 (1983).
54. Bussi, G., Donadio, D. & Parrinello, M. Canonical sampling through velocity rescaling. *J. Chem. Phys.* **126**, 014101 (2007).
55. Parrinello, M. & Rahman, A. Polymorphic transitions in single crystals: A new molecular dynamics method. *J. Appl. Phys.* **52**, 7182–7190 (1981).
56. Hess, B., Bekker, H., Berendsen, H. J. C. & Fraaije, J. G. E. M. LINCS: A linear constraint solver for molecular simulations. *J. Comput. Chem.* **18**, 1463–1472 (1997).
57. Holden, Z. C., Richard, R. M. & Herbert, J. M. Periodic boundary conditions for QM/MM calculations: Ewald summation for extended Gaussian basis sets. *J. Chem. Phys.* **139**, 244108 (2013).

TR-FRET assays were performed by Femke A. Meijer and Iris A. Leijten-van de Gevel performed the thermal shift assays and purified the RORγt protein used for the TR-FRET assays.

CHAPTER 6

Epilogue

Abstract

Over the last decades, nuclear receptors have emerged as a primary target for drug discovery because of their involvement in various aspects of human physiology. Numerous small molecules have been developed to target members of this receptor family to modulate their activity, with some having progressed as marketed drugs. The work described in this thesis demonstrated that, apart from activation and inhibition, ligands also regulate processes such as receptor dimerization and allosteric ligand recruitment. This study highlighted that nuclear receptors do not function as simple on-off switches but, instead, generate a scala of responses based on the shape, composition and conformational flexibility of the bound ligand. In this final chapter, we briefly discuss some of the future directions of this work and how some of the results could be applied to other NR-related processes.

Introduction

The effect of nuclear receptor activation or inhibition of the biological response is regularly determined using a single small molecule that modulates the receptor's activity. The work in this thesis described how small molecules not only regulate the activation state of the receptor but also finetune other processes, such as receptor dimerization and allosteric ligand recruitment. We showed that minor modifications in a ligand's scaffold could have significant effects on the associated functions of the receptor. In other words, two chemically different full agonists will each induce maximum activation of the receptor, while leading to different dimerization behavior, generating a potentially different biological response. Therefore, it has been suggested that to prevent misinterpretation; assays should be conducted with at least one reference ligand that is expected to lead to the same biological response.[1] LG100268, bexarotene and 9-cis-retinoic acid are full agonists for RXRα, which are regularly used as tool compounds to induce the active state of the receptor.[2–6] The NanoBiT assay results from Chapter 2 show that these agonists each generate distinct dimerization profiles and are thus all likely to produce a differentiated biological response.

The results from Chapter 5 show that the affinity of the orthosteric ligand can be modulated by an allosteric ligand and vice versa. Naturally occurring orthosteric ligands like cholesterol and desmosterol have been shot to enhance the binding affinity of allosteric modulators *in vitro*. This implies that the biological response in the presence of an allosteric ligand in an *in vivo* format depends on the cooperative effect of both the allosteric modulator and the naturally occurring ligand. Therefore, assay results can be significantly determined by the environment a protein is subjected to.

Altogether, we showed that subtle changes in the ligand scaffold allosterically affect NR's dimerization behavior and the recruitment of allosteric ligands. Moreover, it provides evidence that small molecules can mold the NR's structure to direct particular interactions. In this final chapter, the work described in this thesis will be put into perspective and used as inspiration for future directions. Moreover, we show how some identified ligand-induced mechanisms could influence other NR-associated processes.

Ligand-induced NR heterodimerization

Chapter 2 describes how minor modifications in the rexinoid scaffold can significantly affect the dimerization behavior of RXR. The NanoBiT assay format proved to be a useful tool to determine and quantify the direct interaction between two NRs. Even though the

number of NRs tested in this work was limited to RXRα-RXRα, RXRα-Nurr1, RXRα-PPARα and ERRα-PPARα, several ligands significantly favored specific dimers over others. However, RXR can interact with various other NRs, both permissively and non-permissively.[7] Therefore, producing all the NR-NanoBiT fusion constructs can provide valuable information if ligands can direct the dimerization to one or a subset of RXR heterodimers (Figure 1B). Combining this data with the receptor's structural features allows for the identification of regions that are important for dimer selectivity. Helix 12 of Nurr1, for example, already has been demonstrated to play an essential role in heterodimerization with RXRα. For the RXRα-PPARγ, helix 12 of PPARγ is also present at the dimerization interface and the conformation of this helix is stabilized by residues on helix 7 and 11 of RXRα.[8,9] The length, rigidity and orientation of helix 12 are highly variable across the NR family (Figure 1A).[10,11] These factors, combined with the NR's activation state, will influence the ability to heterodimerize with and get transactivated by RXR. Therefore, also the RXR partner's ligand could play a role in regulating the heterodimerization via this mechanism. Like RXR, ligands binding to the partner NR shape and change the structure and dynamics of the protein partner. Therefore, analyzing single and dual ligand binding across a wide variety of RXR partners using the NanoBiT assay will provide valuable insights into how and if heterodimer selectivity can be achieved and to what extent ligands play a role (Figure 1C).

In Chapters 2 and 3, the LBD of two NRs is used to assess dimerization behavior because this domain is believed to be the primary driving force for dimerization and avoids the challenging purification of bacterially expressed full-length NRs. However, the work described in Chapter 3 shows that full-length ERRα was required to heterodimerize with PPARα. Including the full-length variant of the receptors in the NanoBiT assay format, can create an additional layer of information on the contribution of the other domains (Figure 1D).

Finally, increasing the available crystal structures of RXR heterodimers is essential to understand the mechanism behind heterodimer selectivity. Although there have been major successes obtaining crystal structures of RXR heterodimers, the database remains limited.[8,12,13] Performing MD simulations on these heterodimeric complexes, similar to those performed in Chapter 5, will provide valuable insights into the detailed mechanism behind ligand-induced dimer selectivity. Ultimately, this will aid in developing a molecular blueprint for the design of rexinoids that selectively induce specific heterodimers.

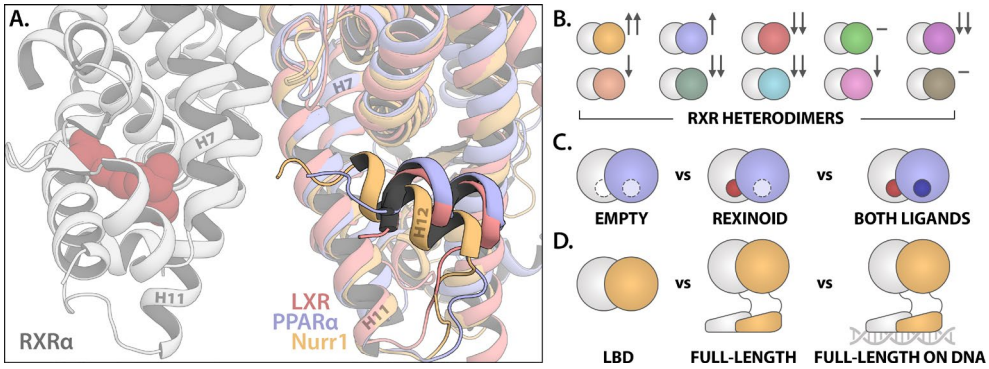

Figure 1 | Structure alignment of different RXRα heterodimer partners. A. LBDs of Nurr1 (PDB: 1OVL)[26] and LXR (PDB: 4DK7)[27] were superimposed on the LBDs of the full-length structure of RXRα-PPARα.[8] Helix 12 of each receptor displays a different length, orientation and helical content. **B.** Illustration of an exemplary effect of rexinoids inducing the formation of specific RXR heterodimers. The up-arrows indicate stabilization of the heterodimer, the down-arrows inhibition of heterodimerization and the dash means no effect. **C.** Illustration of the comparison of the empty, rexinoid or dual ligand-bound state. **D.** Illustration of the comparison of the influence of domain composition on RXR heterodimerization.

Heterodimerization versus transactivation

In Chapter 1, the permissiveness of RXR was briefly discussed. In short, for permissive RXR heterodimers, the sole presence of a rexinoid is sufficient to activate the heterodimeric complex, whereas for non-permissive heterodimers, the partner's ligand is required for activation. What determines the permissiveness of the RXR heterodimer and how ligands contribute remains poorly understood, although progress has been made in recent years.[9,14,15]

Generally, two types of assays are conducted to analyze RXR heterodimerization. First, assays where (part of) a fluorescent protein or luciferase is conjugated to the NR, measuring a fluorescent or luminescent signal. Secondly, a luciferase reporter gene assay where the LBDs are conjugated to a GAL4-DBD. Although both assays rely on heterodimerization, one determines the dimerization of the receptors, while the other determines the ability of the complex to activate gene transcription. Thus, in some cases, ligands can induce a stable heterodimeric complex while being unable to induce gene transcription. The combination of both assays could shed light on how dimerization and transactivation are correlated and how ligands influence both processes.

Orthosteric ligand-induced coactivator selectivity through helix 4-5

Chapter 5 described how small molecules binding to the orthosteric pocket modulate the conformational dynamics of the allosteric pocket through helix 4-5. The orthosteric cholesterol derivatives blocked the movement on Met365 on helix 5, restricting the flexibility of this helix. The majority of the other NR family members also contain bulky residues at this position on helix 5.[10] Therefore, it is likely that other NRs experience a similar behavior upon orthosteric ligand binding. RXRα, for example, has a phenyl residue at this position that is conformationally restricted by the orthosteric ligand (Figure 2). Since the allosteric pocket of RORγt appears to be unique for this NR, the restricted movement is not particularly relevant for allosteric ligand recruitment in other NRs.[16] However, together with helix 3 and 12, helix 4 forms the so-called "charge clamp" responsible for the recruitment of coactivators (Figure 2).[17] The interaction between the protein and a cofactor is dependent on a network of hydrophobic and polar interactions. Although helix 12 significantly enhances coactivator binding in the agonist-bound state, changes in the dynamic behavior of helix 4-5 are likely to influence the recruitment of the coactivator. One can imagine that this could either stabilize or inhibit the formation of a particular NR-coactivator complex. There are several reports demonstrating that orthosteric ligands could indeed direct the recruitment of specific coactivators.[18–22]

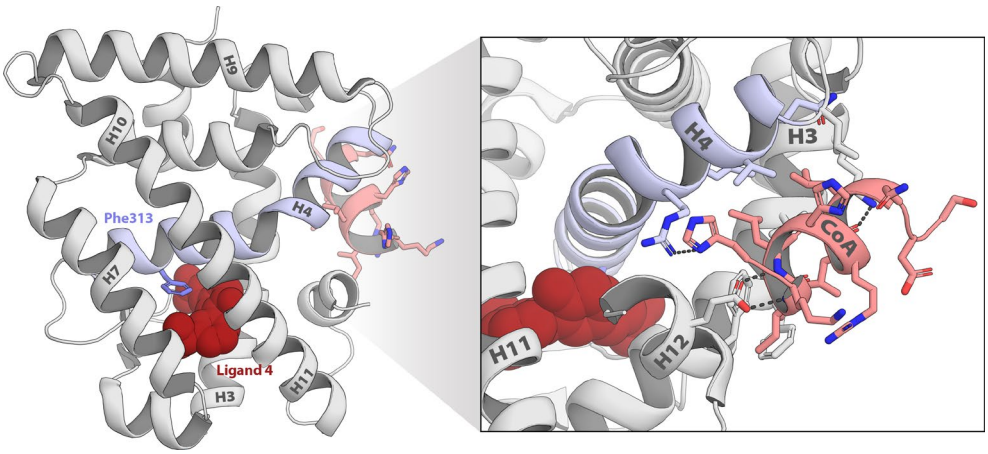

Figure 2 | Effect of orthosteric ligand binding on coactivator binding through helix 4-5. Crystal structure of RXRα (white cartoon) in complex with ligand 4 (red spheres; PDB: 5MKU).[28] Like RORγt, the conformational flexibility of helix 4-5 (light blue cartoon) is restricted by the ligand through a residue blockade on helix 5 (Phe313; blue sticks). This changes the dynamics of helix 4 and can influence coactivator (CoA; red cartoon) binding. Polar interactions are represented as black dashed lines.

However, the mechanism that is responsible for the selectivity has not been reported previously. Helix 4-5 could play a decisive role in coactivator selectivity using a similar mechanism described for cooperative dual ligand binding in RORγt. The conformational dynamics of helix 4 is likely to change depending on the extent to which the orthosteric ligand restricts the movement of helix 5. Therefore, this could lead to an altered affinity for coactivators.

In Chapter 2, a homologous series of biaryl derivatives with varying bulk towards helix 7 was tested for its effect on RXRα heterodimerization. A similar approach could be applied to restrict the movement of helix 5 by synthesizing molecules that regulate the conformational flexibility of Phe313 of RXRα. As an illustration, ligand 4 and the chiral compound 9a[23] are reported to be full agonists for RXRα. However, both ligands induce a different conformation of Phe313 as well as a slight shift of helix 5 compared to apo-RXRα[24] (Figure 3A). Compound 9a introduces more bulk towards Phe313 compared to ligand 4, thereby displacing this residue further away from the coactivator binding pocket. If the conformational flexibility of Phe313 is indeed important for coactivator selection, both ligands are likely to display different coactivator binding behavior. Combining coactivator recruitment assays with crystallographic data can be used to determine if

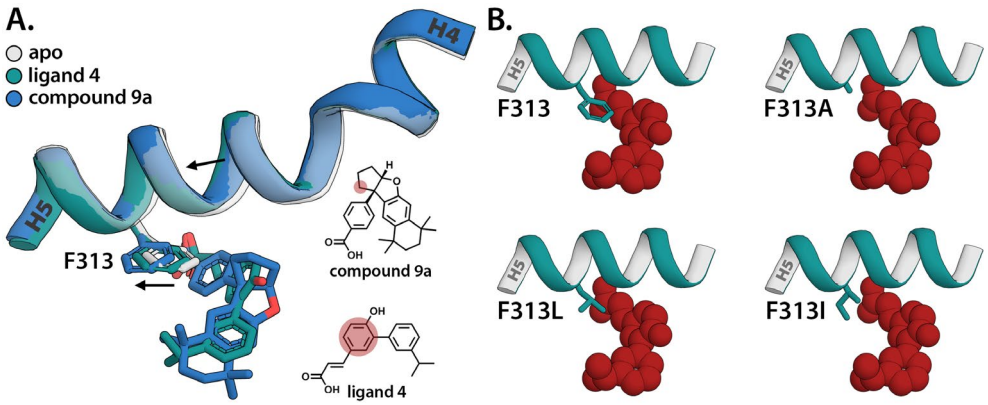

Figure 3 | Effect of orthosteric ligand binding on helix 4-5 dynamics. A. Superimposed structures of apo-RXRα (PDB: 6HN6; semi-transparent white), RXRα in complex with ligand 4 (PDB: 5MKU; teal) and RXRα in complex with compound 9a (PDB: 5EC9; blue). Arrows indicate the displacement of helix 5 and Phe313 compared to the apo structure. The semi-transparent red circles on the chemical structures indicate the part of the ligand that is oriented towards Phe313 of RXRα. **B.** Structural representation of some proposed mutants of Phe313 of RXRα. The mutant residues are smaller and more flexible than the wild-type phenylalanine and, therefore, less sterically hindered by the orthosteric ligand (red spheres).

there is a relationship between the conformational freedom of Phe313 and coactivator recruitment.

Site-directed mutagenesis could also be used to convert Phe313 to a smaller, more flexible residue, like alanine, leucine or isoleucine (Figure 3B). Assuming that the Phe313 mutations do not impair rexinoid binding, the dynamics of helix 4-5 in the presence of an orthosteric ligand is likely to be different for each mutant protein. Therefore, in the presence of the same rexinoid, each mutant is expected to display different coactivator binding behavior. Performing coactivator recruitment assays using the mutant proteins in the presence of different rexinoids and coactivator peptides will provide valuable information on the role of helix 4-5 in coactivator selection.

Both discussed approaches can be complemented with molecular dynamics measurements to unravel the underlying allosteric mechanism of how orthosteric ligands change the behavior of the AF-2 site. Like RORγt, RXRα has an alanine at the transition between helix 4 and 5. Therefore, orthosteric ligands can perhaps also adjust the conformation of this residue from one helix to the other, changing the dynamics of the helix 4 (mechanism described in Chapter 5).

Despite the preceding methods focusing on RXRα, the same principle can be applied to other NRs with an accessible orthosteric LBP.

Closing Thoughts

This work has aimed to improve our understanding of how NRs function on a molecular level and how ligands contribute to their behavior. NRs have proven to be more than a simple ligand-induced on-off switch for gene transcription. Two chemically distinct ligands do not necessarily lead to two different conformations of the NR. Instead, modest changes in the receptor's architecture are often observed. We showed that, despite the differences being small, these changes can significantly determine the behavior of the receptor. We were fortunate to obtain structural data for multiple related NR structures, allowing the identification of these small differences. Understanding the molecular mechanism through which a drug alters a receptor's behavior will not immediately lead to the development of a drug, but it will certainly facilitate a more direct and rational approach.

References

1. le Maire, Teyssier, Balaguer, Bourguet & Germain. Regulation of RXR-RAR Heterodimers by RXR- and RAR-Specific Ligands and Their Combinations. *Cells* **8**, 1392 (2019).
2. Széles, L. *et al.* Research resource: Transcriptome profiling of genes regulated by RXR and its permissive and nonpermissive partners in differentiating monocyte-derived dendritic cells. *Mol. Endocrinol.* **24**, 2218–2231 (2010).
3. Takahashi, H., Yoshida, K. & Yanagisawa, A. Synthesis of Carbocyclic Aromatic Compounds Using Ruthenium-Catalyzed Ring-Closing Enyne Metathesis. *J. Org. Chem.* **74**, 3632–3640 (2009).
4. Ijpenberg, A. *et al.* In vivo activation of PPAR target genes by RXR homodimers. *EMBO J.* **23**, 2083–2091 (2004).
5. Mounier, A. *et al.* Bexarotene-activated retinoid X receptors regulate neuronal differentiation and dendritic complexity. *J. Neurosci.* **35**, 11862–11876 (2015).
6. Lehman, A. M. B. *et al.* Activation of the retinoid X receptor modulates angiotensin II-induced smooth muscle gene expression and inflammation in vascular smooth muscle cells. *Mol. Pharmacol.* **86**, 570–579 (2014).
7. Chawta, A., Repa, J. J., Evans, R. M. & Mangelsdorf, D. J. Nuclear receptors and lipid physiology: Opening the x-files. *Science* vol. 294 1866–1870 (2001).
8. Chandra, V. *et al.* Structure of the intact PPAR-γ–RXR-α nuclear receptor complex on DNA. *Nature* **456**, 350–356 (2008).
9. Kojetin, D. J. *et al.* Structural mechanism for signal transduction in RXR nuclear receptor heterodimers. *Nat. Commun.* **6**, 8013 (2015).
10. Leijten-van de Gevel, I. A. & Brunsveld, L. Delineation of the molecular determinants of the unique allosteric binding site of the orphan nuclear receptor RORγt. *J. Biol. Chem.* (2020) doi:10.1074/jbc.ra120.013581.
11. Wurtz, J. M. *et al.* A canonical structure for the ligandbinding domain of nuclear receptors. *Nat. Struct. Biol.* **3**, 87–94 (1996).
12. Rochel, N. *et al.* Common architecture of nuclear receptor heterodimers on DNA direct repeat elements with different spacings. *Nat. Struct. Mol. Biol.* **18**, 564–570 (2011).
13. Orlov, I., Rochel, N., Moras, D. & Klaholz, B. P. Structure of the full human RXR/VDR nuclear receptor heterodimer complex with its DR3 target DNA. *EMBO J.* **31**, 291–300 (2012).
14. Wang, N., Zou, Q., Xu, J., Zhang, J. & Liu, J. Ligand binding and heterodimerization with retinoid X receptor (RXR) induce farnesoid X receptor (FXR) conformational changes affecting coactivator binding. *J. Biol. Chem.* **293**, 18180–18191 (2018).
15. Lammi, J., Perlmann, T. & Aarnisalo, P. Corepressor interaction differentiates the permissive and non-permissive retinoid X receptor heterodimers. *Arch. Biochem. Biophys.* **472**, 105–114 (2008).
16. Scheepstra, M. *et al.* Identification of an allosteric binding site for RORγt inhibition. *Nat. Commun.* **6**, 1–10 (2015).
17. He, B. & Wilson, E. M. Electrostatic Modulation in Steroid Receptor Recruitment of LXXLL and FXXLF Motifs. *Mol. Cell. Biol.* **23**, 2135–2150 (2003).
18. McKenna, N. J. & O'Malley, B. W. Minireview: Nuclear Receptor Coactivators—An Update. *Endocrinology* **143**, 2461–2465 (2002).
19. Takeyama, K.-I. *et al.* Selective Interaction of Vitamin D Receptor with Transcriptional Coactivators by a Vitamin D Analog. *Mol. Cell. Biol.* **19**, 1049–1055 (1999).
20. Bramlett, K. S., Wu, Y. & Burris, T. P. Ligands specify coactivator nuclear receptor (NR) box affinity for estrogen receptor subtypes. *Mol. Endocrinol.* **15**, 909–922 (2001).
21. Kraichely, D. M., Sun, J., Katzenellenbogen, J. A. & Katzenellenbogen, B. S. Conformational changes and coactivator recruitment by novel ligands for estrogen receptor-α and estrogen receptor-β: Correlations with biological character and distinct differences among SRC coactivator family members. *Endocrinology* **141**, 3534–3545 (2000).

22. Grenier, J. *et al.* Selective recruitment of p160 coactivators on glucocorticoid-regulated promoters in Schwann cells. *Mol. Endocrinol.* **18**, 2866–2879 (2004).
23. Sundén, H. *et al.* Chiral Dihydrobenzofuran Acids Show Potent Retinoid X Receptor-Nuclear Receptor Related 1 Protein Dimer Activation. *J. Med. Chem.* **59**, 1232–1238 (2016).
24. Eberhardt, J., Mcewen, A. G., Bourguet, W., Morasa, D. & Dejaegerea, A. A revisited version of the apo structure of the ligand-binding domain of the human nuclear receptor retinoic x receptor a. *Acta Crystallogr. Sect. F Struct. Biol. Commun.* **75**, 98–104 (2019).
25. Koppen, A. *et al.* Nuclear receptor-coregulator interaction profiling identifies TRIP3 as a novel peroxisome proliferator-activated receptor γ cofactor. *Mol. Cell. Proteomics* **8**, 2212–2226 (2009).
26. Wang, Z. *et al.* Structure and function of Nurr1 identifies a class of ligand-independent nuclear receptors. *Nature* **423**, 555–560 (2003).
27. Kopecky, D. J. *et al.* Discovery of a new binding mode for a series of liver X receptor agonists. *Bioorganic Med. Chem. Lett.* **22**, 2407–2410 (2012).
28. Scheepstra, M. *et al.* Ligand Dependent Switch from RXR Homo- to RXR-NURR1 Heterodimerization. *ACS Chem. Neurosci.* **8**, (2017).

Structural Elucidation of Novel Allosteric Regulatory Mechanisms in Nuclear Receptors

The central role of nuclear receptors (NRs) in disease pathology established this protein class as a prominent drug target for various diseases such as diabetes, neurological disorders and cancer. This is exemplified by the large number of approved drugs, and drug candidates that target NRs. Over the last decades, increasing evidence suggested that small molecules binding to NRs do not only alter the activity state of the receptor but also modulate related functions such as receptor dimerization, coactivator selectivity and allosteric ligand recruitment. These functions significantly contribute to the biological response and should be considered when selecting ligands for biological studies. The molecular mechanism by which small molecules modulate these related functions remains mostly unclear.

The work described in this thesis aims to improve our mechanistic understanding of how the shape and chemical composition of small molecules influence nuclear receptor dimerization and the recruitment of allosteric ligands. Chapter 2 describes how small molecules binding to the orthosteric ligand-binding pocket of RXRα influence the homo- and heterodimerization behavior of this NR. RXRs have the unique ability to heterodimerize with various other NR family members, thereby modulating their activity. The RXRα-Nurr1 heterodimer is the primary focus of this research since Nurr1 proved challenging to modulate directly, making modulation via RXRα a compelling alternative. An RXRα-Nurr1 heterodimer model is constructed to determine regions of the protein that are important for receptor dimerization and can be modulated by molecules binding to the orthosteric LBP. A modular *in vitro* NanoBiT complementation assay is developed to identify the effect of orthosteric ligand binding on the homo- and heterodimerization behavior of RXRα. This assay revealed that small molecules that introduce bulk towards particular parts of the protein promote specific dimer complexes over others, which shows to be in agreement with the heterodimer model. The results demonstrate that ligand design can effectively be used to steer the dimerization equilibrium.

Chapter 3 presents a collaborative project with Ghent University to identify the direct interaction between ERRα and PPARα, two NRs regulating mammalian oxidative metabolism. The LBDs of ERRα and PPARα could be purified effectively but show no physical interaction in various *in vitro* assay setups. An *in vitro* His-tag pulldown assay is developed to show that full-length ERRα was required to dimerize with the PPARα-LBD.

This established ERRα-PPARα as one of the first examples of a non-RXR NR heterodimer. The requirement of the full-length receptor for dimeric association demonstrates that the LBD is not always the primary driving force for NR dimerization.

Chapter 4 of this thesis focuses on RORγt, an NR associated with chronic autoimmune diseases, which recently demonstrated the ability to be modulated by ligands binding to an allosteric pocket. The allosteric mode of action of two chemically distinct ligands is confirmed: the *in silico*-derived FM26 and compound 13 from Glenmark Pharmaceuticals. Both ligands show no competitive binding with orthosteric modulators for the protein but demonstrate to effectively displace a probe binding to the allosteric pocket. Ultimately, the cocrystal structures of RORγt with FM26 and compound 13 confirmed the allosteric binding modes for these ligands, which required extensive optimization of the RORγt protein purification protocol. Despite the binding mode of FM26 and compound 13 being comparable to the earlier reported allosteric modulator MRL-871, both ligands induce an altered conformation of helix 4 and the loop before helix 12 of RORγt. Compounds allosterically targetting NRs are in strong demand, making FM26 and compound 13 valuable additional examples of allosteric nuclear receptor modulators.

Chapter 5 continues on RORγt, where we determine if orthosteric and allosteric ligands can simultaneously bind to RORγt and if this affects either ligand's potency. Biophysical assays reveal that the presence of an orthosteric modulator enhances the allosteric ligand's binding affinity. The ternary complex of RORγt with an orthosteric and allosteric ligand simultaneously bound is crystallized to determine the mechanism behind this cooperative binding behavior. In total, twelve high-resolution crystal structures are obtained, with all combinations of four orthosteric and three allosteric ligands. Careful analysis of the structures containing both ligands and the structures with only the allosteric ligand present reveals subtle, but mechanistically essential differences. Binding of an orthosteric modulator leads to a contraction of the allosteric ligand-binding pocket via helix 4, enhancing the binding affinity of the allosteric ligand. These results are confirmed using comprehensive molecular dynamics studies, which provide valuable information about the NR's dynamic behavior. Apparent differences in the dynamic behavior are observed depending on which ligands are bound to RORγt.

Finally, the epilogue puts the research performed in this thesis into perspective and provides recommendations for future research. Moreover, we elaborate on how the molecular mechanism behind cooperative dual ligand binding can also occur in other NRs and how this mechanism can impact coactivator binding and coactivator selection.

In summary, the work described in this thesis demonstrates that the morphology and chemical composition of the NR ligand significantly contributes to receptor dimerization behavior and the recruitment of allosteric ligands. Apart from potency, these are aspects that should be considered when selecting a ligand for biological studies. Understanding how small molecules influence these associated NR functions is essential for developing drug candidates that induce the desired biological response.

Curriculum Vitae

Rens de Vries was born October 6th, 1993, in Hoorn (The Netherlands). After completing his secondary education in 2010, he finished the propedeutic program Engineering Physics at Fontys University of Applied Sciences a year later. In 2011, he started the Bachelor Biomedical Engineering at Eindhoven University of Technology. He received his BSc and MSc degree in Biomedical engineering in 2014 and 2016, respectively. During his bachelor program, he worked in the group of prof. dr. Bert Meijer on the functionalization of supramolecular nanostructures with proteins. In his master, he performed research in the group of prof. dr. ir. Luc Brunsveld, under the direct supervision of dr. Christian Ottmann. In this research, the molecular interaction between 14-3-3 and the Parkinson's disease-associated LRRK2 was analyzed and quantified. This work was continued during his internship at the Lead Discovery Center in Dortmund (Germany) where high-throughput screening and assay development were used to find drug candidates for this interaction. In 2016, he started his PhD research under the supervision of prof. dr. ir. Luc Brunsveld in the laboratory of Chemical Biology. He determined how small molecules can modulate the structure and conformational dynamics of nuclear receptors on a molecular level. The most relevant results of this research have been described in this thesis.

List of Publications

- R.M.J.M. de Vries*, A. de Dreu* & L. Brunsveld*.* A NanoBiT complementation assay to identify ligand-controlled RXR heterodimerization. *In preparation*.
- I.A. Leijten-van de Gevel, K.H.N. van Herk, R.M.J.M. de Vries & L. Brunsveld*.* Elucidation of the MRL-871 binding mode in PPARγ. *In preparation*.
- R.M.J.M. de Vries & L. Brunsveld*.* Purification of the RORγt ligand-binding domain for protein crystallography. *In preparation*.
- R.M.J.M. de Vries*, F.A. Meijer*, R.G. Doveston, I.A. Leijten-van de Gevel, *et al.* Cooperativity in Ligand Binding between the Orthosteric and Allosteric Binding Sites of RORγt. *Submitted*.
- S.J. Desmet, J. Thommis, R.M.J.M. de Vries, S. Timmermans, *et al.* ERRα functions as a rheostat of PPARα transcriptional activity controlling energy metabolism gene expression. *Submitted*.
- R.M.J.M. de Vries, R.G. Doveston, F.A. Meijer & L. Brunsveld*.* Elucidation of an Allosteric Mode of Action for a Thienopyrazole RORγt Inverse Agonist. *ChemMedChem* **15**, 561–565 (2020).
- F.A. Meijer, R.G. Doveston, R.M.J.M. de Vries, G.M. Vos, *et al.* Ligand-Based Design of Allosteric Retinoic Acid Receptor-Related Orphan Receptor γt (RORγt) Inverse Agonists. *J. Med. Chem.* **63**, 241–259 (2020).
- F.A. Meijer*, I.A. Leijten-van de Gevel*, R.M.J.M. de Vries* & L. Brunsveld. Allosteric small molecule modulators of nuclear receptors. *Mol. Cell. Endocrinol.* **485**, 20–34 (2019).
- M. Scheepstra, S.A. Andrei, R.M.J.M. de Vries, F.A. Meijer, *et al.* Ligand Dependent Switch from RXR Homo- to RXR-NURR1 Heterodimerization. *ACS Chem. Neurosci.* **8**, (2017).
- L.M. Stevers, R.M.J.M. de Vries, R.G. Doveston, L-G. Milroy, *et al.* Structural interface between LRRK2 and 14-3-3 protein. *Biochem. J.* **474**, (2017).
- L.M. Stevers, C.V. Lam, S.F.R. Leysen, R.M.J.M. de Vries, *et al.* Characterization and small-molecule stabilization of the multisite tandem binding between 14-3-3 and the R domain of CFTR. *Proc. Natl. Acad. Sci. U. S. A.* **113**, E1152-1161 (2016).

* These authors contributed equaly.

Acknowledgements

En daar zit ik dan: proefschrift af en bezig om mijn werk van de afgelopen vier jaar te evalueren. Voor je aan je PhD begint, denk je nog: Vier jaar! Dan heb je echt alle tijd om aan een project te werken! Het was een paar keer knipperen en toen zat het er ook alweer op. Nou ja, ze zeggen dat de tijd vliegt als je het leuk hebt, dus het zal wel een goed teken zijn! Hoewel het voorbijgevlogen is, kan ik met een tevreden gevoel terugkijken op een ontzettend mooie periode waarin ik veel geleerd heb, geweldige mensen heb leren kennen en ik heb geprobeerd mijn steentje bij te dragen aan de wetenschap. Ik heb het geluk gehad veel talentvolle wetenschappers en vrienden om mij heen te hebben die mij hebben bijgestaan gedurende mijn promotie. Bij hen wil ik daarom graag nog even stilstaan.

Allereerst wil ik mijn promotor Luc erg bedanken voor het vertrouwen om mij binnen zijn groep aan dit mooie project te laten werken. Hoewel we de deur bij elkaar niet platliepen, maakte je altijd tijd wanneer dat nodig was, zowel op persoonlijk als professioneel vlak. Je hebt mij veel vrijheid gegeven tijdens mijn project waardoor ik mezelf goed heb leren kennen, iets wat mij erg geholpen heeft in mijn persoonlijke ontwikkeling. Ik heb veel bewondering voor hoe je zo'n grote en diverse onderzoeksgroep succesvol draaiende houdt. De Chemical Biology-groep is inmiddels zo groot dat het moeilijk is bij te houden wie waar nu ook alweer mee bezig is. Toch weet je altijd iedereen te voorzien van gedetailleerde feedback en ideeën, ook buiten je eigen onderzoeksgroep. Luc, dank je wel voor de afgelopen jaren en ik hoop dat je het niet heel vervelend vond dat ik maar 'u' tegen je bleef zeggen. Ik wens je het allerbeste toe.

I was very excited when you accepted my invite to become my co-promotor. Richard, as a former post-doc in our group, you know how tricky RORγt can be. I'm happy that, in the end, we were able to solve the issues surrounding this protein and were able to write some nice articles together. Your detailed feedback during meetings, as well as on presentations and manuscripts, has always been greatly appreciated. Thanks for all your support and we stay in contact.

Ik wil ook graag de andere leden van mijn promotiecommissie bedanken voor de bijdrage die ze hebben geleverd aan de inhoud van dit proefschrift en het deelnemen aan mijn verdediging. Karolien, ik heb met veel plezier met Sofie en u samengewerkt aan het onderzoek beschreven in hoofdstuk 3. Naar mijn mening was dit een prachtig voorbeeld

van een zeer effectieve interdisciplinaire samenwerking. Ik heb altijd veel bewondering gehad voor uw passie voor en visie op het NR-onderzoek. Uw vrolijke mailtjes zal ik in ieder geval niet vergeten, mijn dag was altijd weer helemaal goed als ik er weer eentje van u binnenkreeg. Deze automatische mail in het bijzonder: *'Hi, I'm OOO and somewhere in an Ecuadorian jungle trying to ward off snakes, spiders etc. Please expect a delay in my response'.* Karolien, dank je wel. Christian, ik heb nogal wat tijd doorgebracht in je kantoor, meestal met de beide Linux-pc's tegelijkertijd in gebruik. En als ik niet bij je op kantoor zat, dan werkte ik wel via TeamViewer op die pc's. Het gebeurde dan ook menigmaal dat mijn muis opeens een magisch zetje kreeg. Nou ja, dan zag Christian in elk geval dat ik aan het werk was! Ik wil je ook erg bedanken voor al je input gedurende mijn PhD-traject en ik wens je heel veel succes en geluk toe met AmbAgon Therapeutics!

Arthur Oubrie, ik ben blij dat je deel wilde nemen aan mijn promotiecommissie en wil je bedanken voor de tijd die je hebt besteed aan het lezen van mijn proefschrift en je zeer nuttige en scherpe feedback. Ook wil ik Wilbert Zwart, Bart Markvoort en Jan van Hest bedanken voor hun deelname aan mijn promotiecommissie en ik zie er erg naar uit om met jullie van gedachten te wisselen over mijn onderzoek. Verder wil ik voorzitter Maarten Merkx bedanken voor zijn deelname, maar ook voor de constructieve feedback en ideeën over het onderzoek gepresenteerd in hoofdstuk 2. And last, but certainly not least, I would like to thank Lech-Gustav Milroy. You started as my co-promotor but left the university to proceed with an industrial career. However, you helped me to set the foundation for my PhD-work and you always made time to sit down and listen to yet a new theory of mine. We also spend quite some time doing a personality test, which proved to be extremely helpful for me to grow as a person. I also remember the amazing LoesSpTevers-project we did together, good times.

Ik heb altijd een hekel gehad aan het woord "paranimf", maar ja, zo heet het nu eenmaal, helaas. Ik zou het liever twee heel goede vrienden willen noemen die mij niet alleen hebben bijgestaan tijdens mijn verdediging, maar ook een rots in de branding waren gedurende mijn gehele PhD-traject. Daan en Wiggert, ik ben heel blij dat jullie dit voor mij wilden doen. We hebben nogal wat tijd samen doorgebracht, in de trein, op kantoor, en laten we vooral ons shoppingdagje in het pittoreske Utrecht niet vergeten. Jullie zijn allebei heel talentvolle wetenschappers en ik wens jullie veel geluk toe in jullie toekomst!

Naast Daan zaten er nog twee andere collega's bij mij op kantoor: Peggy en Shidong. De deur van ons kantoor werd de afgelopen vier jaar nogal vaak platgelopen, doordat wij

een cel-labverantwoordelijke, een 24/7-vraagbaak en de Biolab-moeder op één kantoor hadden. Tegen het einde van mijn PhD werd het vaak zo druk dat we besloten de deur maar even dicht te doen, soms zelfs de lichten uit om mensen maar te laten denken dat we er niet waren. Het zorgde voor veel leuke momenten. Net als de muziekmiddagen waarop we hard aan het werk waren, maar er ook een goede sfeer hing in kantoor. 'Daan, van wie is dit nummer?' Met dan als antwoord: 'Even luisteren hoor… Nou ja, zal dan wel van Bruce Springsteen zijn'. En ijsjes halen voor de Biolab cleaning… Ik denk met veel plezier terug aan de tijden op dit leuke kantoor; ik hoop erg dat jullie een leuke vervanger voor mij krijgen. Shidong, you were the perfect addition to our office. With two goofy guys that pretty much said everything that came to mind, it was nice to have you as a counterbalance. Your Chinese snacks and your incomparable sense of humor was truly appreciated. I wish you the best of luck with your PhD-project, I'm sure you will do great. And do not forget; don't be a sucker...

En dan de NR Kerngroep, Femke en Iris. Ons groepje van drie vormde een hecht en effectief onderzoeksteam. Doordat ieder van ons een ander onderzoeksspecialisme had, konden we elkaar erg goed helpen. We zijn een heel aantal keren met z'n drieën naar een congres geweest, iets wat ik vaak genoeg als een soort van vakantie bestempelde. We waren een uniek groepje mensen waarin iedereen zijn of haar rol had, waardoor het altijd op rolletjes liep. Femke, wij hebben zoveel met elkaar samengewerkt, dat er niet veel papers zijn waar de ander niet op staat. Ik heb de samenwerking altijd als heel prettig ervaren; ik wist precies waar ik aan toe was en wat ik van je kon verwachten. Je bent iemand van je woord en hebt een bijzonder doorzettingsvermogen. Heel veel succes met de afronding; je mag trots op jezelf zijn! Iris, ook wij hebben veel tijd besteed in elkaars kantoor om de verschillende onderzoeksprojecten en ideeën door te spreken. Het kon soms wel de hele middag duren, maar ja, dan konden we wel weer met een hoop nieuwe ideeën aan de gang! Een vraagje nog: bestaat Windows 11 (zelf)? Femke en Iris, ik wens jullie al het beste toe met jullie PhD en alles wat erna komen gaat.

En dan de leden van de BitterbalBBQ/Lunch/KoffieThee?-groep: Simone, Lenne, Maaike, Suzanne, Femke, Iris, Daan en Wiggert. Stuk voor stuk geweldige mensen met wie je kunt lachen, sparren over onderzoek en die je een heel fijne tijd bezorgen. Jullie hebben van mijn PhD-traject een gezellige tijd gemaakt. Dank jullie wel voor alle leuke momenten en dat jullie mij van mijn bureaustoel hebben getrokken om mee te gaan voor lunch/koffie! Lenne, ik wil jou ook heel hartelijk bedanken voor al je hulp en in het bijzonder voor de DNA-, NanoBiT- en promotieafronding-gerelateerde zaken. Je bent een

fijne en betrokken collega aan wie de groep heel veel heeft gehad! Simone, bij jou kon ik altijd terecht voor vragen, maar ook voor een goed gesprek. Ik wil je ook nog bedanken voor de "Rens can/can't help you"-kaarten achter mijn bureau. Ook al namen de mensen ze niet altijd serieus, het hielp wel om mensen ervan bewust te maken dat de vraagbaak soms zelf ook aan het werk moest. Eigenlijk had jij deze kaarten ook moeten hebben! Dank je wel dat je me zo goed in de gaten hebt gehouden tijdens mijn promotie. Het ga je goed! Maaike, volgens mij heb ik jou altijd vrolijk gezien. Je enthousiasme en je fijne gevoel voor humor zorgt telkens weer voor een goede sfeer. Ik wens jou en Lenne samen veel geluk toe en we houden contact! Mischief Managed. En natuurlijk ook nog Suzanne. Ik ben altijd fan geweest van je scherpe, sarcastische opmerkingen. We hebben nogal wat gefotoshopt de afgelopen jaren, wat zeker heeft geleid tot een paar pareltjes. Ik meen me een plaatje te herinneren waarop ik in mijn witte labjas een ijsbaan aan het schrobben ben... Een moment dat me nog lang zal bijblijven is het avontuur in Helix waarbij we op zoek waren naar een "foes". Suzanne, heel veel succes met je promotie, dat gaat helemaal goedkomen!

Dan nog wat snelle, maar zeker niet onbelangrijkere bedankjes. Olga, voor het zijn van een prettige en wijze kantoorgenoot aan het begin van mijn promotie. Loes, nogmaals dank voor je begeleiding tijdens mijn master, je hebt me goed afgeleverd! En je was natuurlijk ook een superfijne collega tijdens mijn promotie. Eline, dank je voor al je hulp tijdens mijn promotie, je vlotte babbel en je schaterlach. Henk, voor de koffie en de goede praat natuurlijk! Christine, voor de schone werkplek en de talloze verhalen. Sebastian, voor je hulp met de SPR en voor de karaoke! Pim, voor je kritische blik op de wetenschap en de talloze inzichten. Peter, for being a very talented post-doc and my favourite Aussie! Bente en Emira (zeg je toch vaak in één adem, hè!), jullie zijn heel getalenteerde en hardwerkende collega's. Heel veel succes met jullie promoties! Bas, je ging dan wel niet vaak mee met de koffie, maar ik blijf het cool vinden dat ik in je voorprogramma stond bij de Chemical Biology meeting! Guido en Maxime (zeg je ook vaak in één adem), jullie heb ik ook nog met veel plezier mogen begeleiden tijdens jullie master. Ik wens jullie allebei heel veel succes toe met jullie promotie! Madita, thanks for all your help related to crystallography but also for all the nice conversations we had. I wish you all the best for the future. Sylvia, dank je wel voor alle gezellige momenten en de goede gesprekken. Heel veel succes met je PhD traject, ik wens je veel geluk en gezondheid toe. We blijven zeker in contact! Ook Marjo en Tanja wil ik heel erg bedanken voor alle inspanningen om alles logistiek op rolletjes te laten lopen. Marjo, ik wil je erg bedanken voor al je hulp de

afgelopen jaren, ook nadat je al eigenlijk niet meer de secretaresse van Luc was! Tanja, jij bent echt een doorpakker. Als jij iets op je nam wist je dat het in goede handen was en voor elkaar ging komen! Ik wil je ook erg bedanken voor al je behulpzame mailtjes tijdens de coronatijd! I want to thank Florian and Nicky for being amazing teammates and two dear friends. Thanks a lot for all the great times.

Ik wil ook de studenten die mij geholpen hebben met dit mooie project heel hartelijk bedanken voor hun bijdragen aan hoofdstuk 2 van mijn proefschrift. In volgorde: Johan Verhoeven, Pim Vendrig, Laureen de Bever, Timo Schaap en Anne de Dreu. Johan, Pim, Laureen en Timo hebben veel tijd besteed in het chemisch lab om RXR-liganden te maken en te zuiveren. Laat ik zeggen dat molecuulsynthese niet per se mijn sterkste punt was… Ik ben dan ook heel erg blij dat ik deze talentvolle studenten heb mogen begeleiden. Heel erg bedankt voor jullie inzet en ik wens jullie het beste toe. Anne heeft ontzettend veel tijd gestoken in het ontwerp en de optimalisatie van het NanoBiT-assay. Het heeft bloed, zweet en tranen gekost, maar de aanhouder wint! Het heeft een prachtig hoofdstuk in mijn proefschrift opgeleverd. Anne, dank je wel en ik wens ook jou heel veel succes toe met je PhD. Ik heb er alle vertrouwen in dat je het hartstikke goed gaat doen!

Anderhalve week thuis in je eentje aan je proefschrift werken terwijl je vriendin vakantie gaat houden óf lekker meegaan en op locatie aan je proefschrift schrijven? Die keuze was snel gemaakt! Ik heb dan wel tien volle dagen geschreven en niet echt van het weer en de omgeving kunnen genieten, maar ik heb wel bijna twee hoofdstukken af geschreven in Schoorl! Ik wil mijn schoonfamilie heel erg bedanken dat ik een ruimte in jullie vakantiehuisje mocht omtoveren tot een minikantoor! Ageeth, Sjon, Milou en Lindsey, het is alweer 14 jaar geleden dat ik bij jullie voor het eerst over de vloer kwam en in die tijd is er heel veel gebeurd. Veel mooie momenten, vakanties en talloze keren dat we lekker muziek maakten en meezongen met muziek! Ik heb bij jullie altijd het gevoel van een tweede thuis gehad. Jullie hebben Rosita en mij altijd gesteund in de keuzes die we maakten en de wegen die we bewandelen. Dank jullie wel!

En dan natuurlijk familie De Vries! Ongeveer een decennium geleden wilden mijn broers en ik in Eindhoven gaan studeren. Nou, toen dacht mijn moeder, wat doe ik hier dan nog? Dus hup, wij met z'n allen naar Eindhoven verhuisd om daar een studie Biomedische Technologie te volgen. Ik kon toen echt nog niet bedenken dat ik ongeveer een decennium na dato dit dankwoord van mijn proefschrift zou schrijven. Mam, je hebt het niet makkelijk gehad als alleenstaande moeder met vier jongens. Ik heb zoveel respect voor de manier waarop je je altijd in tienen hebt kunnen delen, iedereen aandacht kon

geven, brood op de plank bracht en alle zaken op orde hield. Eén ding kan ik met zekerheid zeggen: ik had dit dankwoord nooit kunnen schrijven als jij je niet dag in dag uit zo voor ons had ingezet. Leg de lat hoog voor jezelf, daag jezelf uit, maar durf ook af en toe onder die lat door te lopen. Mam, dank je wel dat je ons zo goed hebt afgeleverd! Hopelijk kun je als wijze uil met trots terugkijken naar je vier uitgevlogen duiven.

Ik denk dat ik niet zo'n kritische blik had gehad op de wetenschap als ik niet drie broers had met wie ik altijd in discussie was. Tot vervelends aan toe soms, maar ja, we hadden gewoon allemaal gelijk! Joost, Tom en Sam, ik vind het heel goed om te zien dat nu we ouder worden iedereen zijn eigen pad beloopt en een ieder zijn eigen dromen volgt. Ik ben ongelofelijk trots op jullie en wil jullie bedanken voor de support in de afgelopen jaren!

Ze zeggen soms weleens: 'Zo'n proefschrift, dat is leuk om aan je oma te geven. Bij andere mensen verdwijnt hij toch snel in de boekenkast of onder een pc-monitor.' Nou, en of ik het leuk vind om dit boek aan mijn oma te geven! Ik weet niet wie de afgelopen vier jaar meer werkuren heeft gemaakt, mijn oma of ik. Ik ben blij dat u nog altijd zo vitaal bent en met zoveel plezier een actieve bijdrage levert aan tientallen commissies! Ik wil u ook erg bedanken voor al uw steun en ik hoop dat u het een mooi boek vindt!

Als laatste wil ik afsluiten met mijn lieve vriendin Rosita. Inmiddels ken ik je al langer wél dan niet en ben ik blij dat we nog altijd zo gelukkig samen zijn. Jij hebt mij elke dag van mijn PhD-traject gemotiveerd om het beste uit mezelf te halen. We hebben de loodjes samen gedragen en daar ben ik je dankbaar voor. Dank je wel voor alle steun, liefde en vrijheid die je mij geeft en hebt gegeven. Je bent mijn alles, en onthoud: je bent perfect zoals je bent, veel beter dan de rest! Ik ben trots op je.

En dan is het nu tijd om een punt achter dit verhaal te zetten. Hoofdstuk af, klaar voor het volgende!

Dank jullie wel allemaal,